SCIENCE AND NEW APPLICATIONS

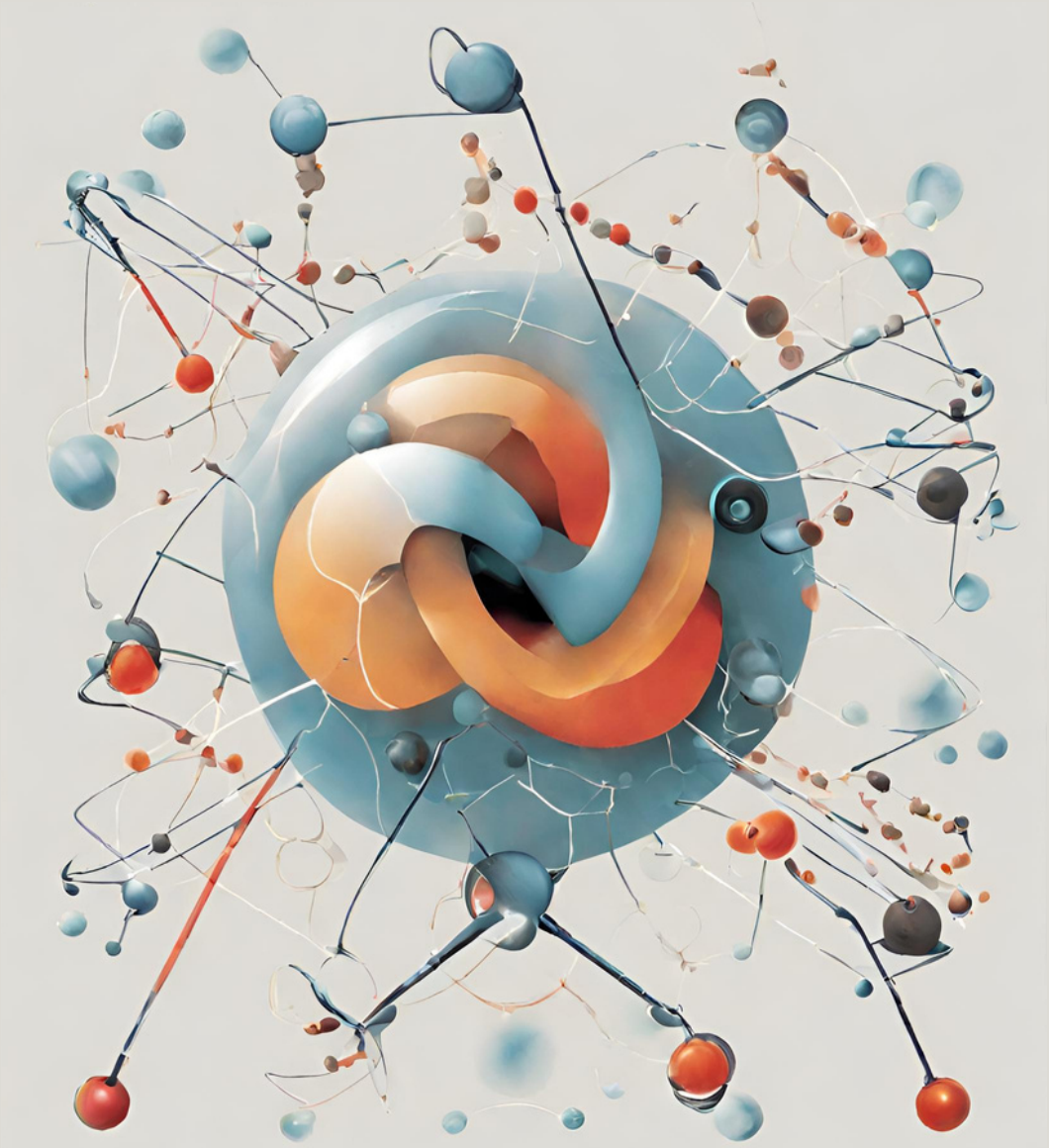

EDITOR
ASSIST. PROF. DR. NİLGÜN ONURSAL

İKSAD
Publishing House

SCIENCE AND NEW APPLICATIONS

EDITOR
Assist. Prof. Dr. Nilgün ONURSAL

AUTHORS
Prof. Dr. Murat ATES
Prof. Dr. Musa SARIKAYA
Prof. Dr. Tolga DEPCİ
Assoc. Prof. Dr. Ersin BAHÇECI
Assoc. Prof. Dr. Hacı Mehmet KAYILI
Assist. Prof. Dr. Nilgün ONURSAL
Assoc. Prof. Dr. Sevil AKÇAĞLAR
Assoc. Prof. Dr. Yunus ÖNAL
Assist. Prof. Dr. Ayşegül YÜCEL
Lecturer Selda SEZER
Musa Halimatu Fago
Zainab Ahmad Muhammad

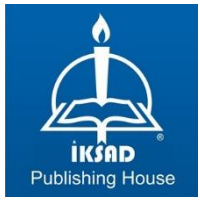

(The Licence Number of Publicator: 2014/31220)
TÜRKİYE TR: +90 342 606 06 75
USA: +1 631 685 0 853
E mail: iksadyayinevi@gmail.com
www.iksadyayinevi.com

It is responsibility of the author to abide by the publishing ethics rules.
Iksad Publications – 2023©

ISBN: 978-625-367-562-2
Cover Design: Eda KOÇAK
December / 2023
Ankara / Türkiye
Size = 16x24 cm

CONTENTS

PREFACE

As we stand at the intersection of innovation and discovery, the realm of science continues to captivate and inspire us with its ceaseless evolution. The pursuit of knowledge, exploration, and experimentation has led to groundbreaking advancements that shape the way we perceive and interact with the world around us. In this collection, "Science and New Applications," we embark on a journey through the frontiers of scientific inquiry, where the boundaries of what is possible are continually expanding.

This compilation serves as a testament to the tireless efforts of scientists, researchers, and thinkers who dedicate their lives to unraveling the mysteries of the universe. Each chapter within this volume delves into diverse fields of science, ranging from physics and chemistry to biology and technology, offering a panoramic view of the multifaceted landscape of human understanding.

The pages that follow explore not only the theoretical foundations of various disciplines but also their practical applications in our daily lives. From cutting-edge technologies that redefine our interactions with the digital realm to innovative approaches addressing global challenges such as climate change and healthcare, the contributions within this anthology illuminate the transformative power of science.

Moreover, this collection aims to foster a sense of curiosity and wonder, inviting readers of all backgrounds to engage with the latest developments in the scientific world. The narrative unfolds with the belief that knowledge is a shared endeavor, and through the dissemination of information, we empower individuals to contribute to the ongoing dialogue of discovery.

As we navigate the complexities of the present and chart the course for the future, "Science and New Applications" stands as a compass, guiding us through the uncharted territories of scientific exploration. It is our hope that this compilation sparks curiosity, instills a sense of awe,

and encourages a collective commitment to the pursuit of knowledge for the betterment of humanity.

May the pages that follow ignite a passion for inquiry and serve as a beacon for those who seek to understand, innovate, and push the boundaries of what is possible in the ever-expanding realm of science.

EDITOR
Assist. Prof. Dr. Nilgün ONURSAL

CHAPTER 1

UTILIZATION OF OLIVE POMACE AS BIO-SORBENT IN CATIONIC DYE ADSORPTION: EQUILIBRIUM, KINETICS AND THERMODYNAMICS STUDIES

Asst. Prof. Dr. Ayşegül YÜCEL[1]
Lecturer Selda SEZER[2]
Prof. Dr. Tolga DEPCİ[3]
Assoc. Prof. Dr. Yunus ÖNAL[4]
Assoc. Prof. Dr. Ersin BAHÇECI[5]
Prof. Dr. Musa SARIKAYA[6]

DOI: https://dx.doi.org/10.5281/zenodo.10444648

[1] Iskenderun Technical University Iskenderun Vocational School, Environmental Protection and Control Program, Hatay, Türkiye, aysegul.yucel@iste.edu.tr, ORCID:0000-0001-7069-7518
[2] Malatya Turgut Ozal University, Akcadag Vocational School, Laboratory and Veterinary Health Program, Malatya, Türkiye, selda.sezer@ozal.edu.tr, ORCID:0000-0002-3136-1250
[3] Iskenderun Technical University, Iskenderun Technical University, Department of Petroleum and Natural Gas Engineering, Hatay, Türkiye, tolga.depci@iste.edu.tr, ORCID:0000-0001-9562-8068
[4] Inonu University, Faculty of Engineering, Department of Chemical Engineering, Malatya, Türkiye, yunus.onal@inonu.edu.tr, ORCID:0000-0001-6342-681
[5] Iskenderun Technical University, Department of Metallurgical and Material Science Engineering, Hatay, Türkiye, ersin.bahceci@iste.edu.tr, ORCID:0000-0002-7719-6051
[6] Inonu University, Faculty of Engineering, Department of Mining Engineering, Malatya, Türkiye, musa.sarikaya@inonu.edu.tr, ORCID:0000-0003-4942-4472

1. INTRODUCTION

In recent years, dyes are used in many different industrial processes such as plastic, paper and pulp production, fabric and leather production. Today, there are more than 10,000 synthetic and organic commercial dyes with different chemical structures. Textile industry is one of the sectors where dye and at the same time water are consumed mostly. During consumption of water in production processes such as washing, abrasion and dyeing, large amounts of wastewater produced. For example, it is estimated that 95 - 400 L of water is consumed for 1 kg fabric production (Al-Ghouti et al. 2020; Jiang et al. 2019).

Many studies have shown that dye wastewater causes serious environmental problems such as carcinogenic and mutagenic products, as well as danger to flora and fauna species, and pollution of clean water (Ismail et al. 2019; Lellis et al. 2019). Since the disposal of wastes by arranging them at the source is an important step in waste management, researches are still ongoing on the treatment and management of wastewater containing dyes (Sarici-Özdemir and Önal 2018). Biological treatment, filtration, adsorption, flocculation and photocatalytic degradation are the methods used in dye waste water studies (Ponraj et al. 2017; Mashkoor et al. 2018; Inamuddin et al. 2019; Gadekar et al. 2020).

Malachite green is a cationic dye, which is used textile industry for paper, wool, silk and leather (Srivastava et al. 2004; Adebayo et al. 2020). The dye appears as crystalline green powder, belongs to triphenylmethane dye and is water soluble (Thiruchelvi et al. 2020). This dye is used as well as in aquaculture as an antibacterial, antiparasitic and antifungal agent. Therefore, it may enter the food chain of the dye and cause carcinogenic, teratogenic and mutagenic effects for humans (Culp et al. 1999; Sava and Hoten 2021; Hamdaoui et al. 2008).

Adsorption stands out as the predominant and highly favored approach for purifying polluted water due to its versatility, effectiveness, and cost-effectiveness. Extensive research in the literature has explored various bio-adsorbents for the purpose of eliminating dyes from wastewater. For example; groundnut hull (Bello et al., 2012; Din et al. 2009), peanut shell (Kılıç and Sarici-Özdemir 2016), ginger waste (Ahmad and Kumar 2010), mango peels

(Bello and Ahmad 2011), mango stone (Shoukat et al., 2017), coconut shell (Bello and Ahmad 2012), apricot shell (Aygün et al. 2003; Önal 2006), olive stone (Fiol et al. 2006; Martin-Lara et al. 2013), olive pomace (Pagnanelli et al. 2003; Rizzi et al. 2017; Marrakchi et al. 2017; Dakroury et al. 2020; Koçer and Acemioğlu 2016; Uzunkavak et al. 2019; Uzunkavak and Özdemir 2019). The importance of the adsorption method in wastewater treatment is rapidly increasing as it provides advantages such as easy applicability and low cost of the adsorbent (Kapdan and Kargi 2002). For this reason, agricultural waste materials belonging to different sectors with little or no economic value and generally causing storage problems are suitable for adsorption in terms of usability (Bharathi and Ramesh 2013; Sayğılı et al. 2015).

Many biomasses with suitable properties for removing textile dyes or heavy metals from waste water have been investigated. It seems to be an attractive source for the disposal of different sector wastes of the increasing food-based urban waste (Das et al. 2015; Moreno-Sader et al. 2020). The high availability, low economic value, environmental friendliness and sustainability of these biomass materials increase the potential for use (Banerjee et al. 2021). Turkey is also located in the Mediterranean countries; olive production is very important in terms of both wealth and tradition. In addition, olive oil production is increasing with the increase in the consumption of olive oil in the World (Marrakchi et al. 2017; Bhatnagar et al. 2014). While an average of 15-22 kg of olive oil is obtained from 100 kg of olives, 35-45 kg of olive pomace is formed (Karta et al. 2016). Considering the production and consumption of olives worldwide, there is a serious problem of solid waste generation (Rizzi et al. 2017). Olive pomace is a solid waste obtained in the production of olive oil, in other words, it is a biological waste, that is, biomass. The accumulation of contaminants such as heavy metals or textile dyes in the structure of natural materials such as olive pomace can be defined as biosorption (Fernandez and Murguia 2020). Work on the use of olive mill solid wastes in the treatment of drinking water containing heavy metals began decades ago. Respectively, the studies about the possible use of olive mill solid wastes as a low-cost improvement adsorbent for heavy metals biosorbents, raised (Veglio et al. 2003; Pagnanelli et al. 2002; Pagnanelli et al. 2003, Havari et al. 2009; Nuhoğlu and Malkoç 2009; Hawari et al. 2014). In the removal of different dyes, activated carbon produced from olive pomace is used (Uğurlu et al. 2007;

Okeowo et al. 2020; Baccar et al. 2010; Demiral 2011; Berrios et al. 2012). Banat et al. they tried to remove the methylene blue. They said that with the increase in the amount of olive pomace, the dye removal efficiency increased (Banat et al. 2007). Akar et al, in their study on reactive dye RR198, claimed that the highest dye biosorption capacity was at pH=2 and that olive pomace was a suitable adsorbent (Akar et al. 2009).

This study utilized olive pomace, a solid waste derived from the olive industry, for the purpose of adsorbing textile dye, known as a hazardous waste. The intention behind using the natural form of olive pomace was to minimize additional expenses. This approach aimed to transform one facility's waste into a valuable resource for managing another facility's waste, thereby contributing to more sustainable waste management practices.

2. MATERIALS AND METHODS

2.1. Preparation of Biosorbent

Olive pomace is a biosorbent material which is the solid waste of olive oil production. The olive pulp taken as solid waste was ground and turned into powder. The pulverized olive pulp was washed with deionized water up to neutral pH and oven-dried at 378 K. The dried olive pomace was screened under 75 μm and its structure was characterized. All experiments were repeated three times. Results are presented as the average of these repetitions.

2.2. Characterization of bioadsorbent

For the structural characterization of olive pomace before and after adsorption XRD (X-ray Powder Diffraction, Rigaku Miniflex 600 with Cu Kα, 40 kV, 15 mA, λ = 1.54050 Å), FT-IR (Fouirer Transform Infrared Spektrofotometre, Perkin Elmer Spectrum Two) was used. For elemental analysis (LECO CHNS 932), thermal analysis (Shimadzu DTA-50 (Differential Thermal Analysis) and TGA-50 (Thermogravimetric analysis) thermal analyzers) were used. SEM (Scanning Electron Microscopy, LeO EVO 40), BET (Brunauer–Emmett–Teller, A Tri Star 3000 Micromeritics) particle size (Malvern Zeta-Sizer Nano series Nano-ZS) were used for surface characterization. In addition, the spectrophotometric determination of malachite green dye adsorption was made in the Agilent Cary 60 UV-vis (Ultraviolet-Visible Spectroscopy) spectrophotometer at 617 nm wavelength.

2.3. Biosorption isotherms

A solution of 200 ppm malachite green in 1 L deionized water was prepared. Kinetic studies were executed at a fixed dose of bio adsorbent (1 g) at 278 K, 308 K, and 323 K at 200 ppm malachite green concentration. Samples were taken at different times for 3 hours and filtered. Adsorbed malachite green solution was analyzed by UV-vis spectrophotometer at different times. The bio adsorbent capacity was determined under the same conditions at 298 K, 308 K, and 323 K temperatures. The biosorption capacity at different times and different temperatures were calculated using equation (1):

$$qe = \frac{(\mathrm{Co}-\mathrm{Ce})}{W} V \qquad (1)$$

In the equation;

q_e = Amount of dye adsorbed at equilibrium (mg adsorbed/g adsorbent).

C_o = Initial dye concentration (mg/L).

C_e = dye solution concentration at equilibrium (mg/L).

V = dye solution volume (liters).

W = Adsorbent amount (g)

2.4. Biosorption thermodynamic

At constant stirring speed (400 rpm) and taking 1 g of bio adsorbent at its own pH, the thermodynamic parameters of malachite green solutions at the fixed concentration (200 ppm) were determined by adsorption at three different temperatures (298 K, 308 K, and 323 K).

3. RESULTS AND DISCUSSION

3.1. Biosorbent characterization

According to the elemental analysis results, olive pomace contains 47.85% C, 6.483% H, 1.054% N, 0.159% S, and 44.094% O. The particle size was determined around 100 to 200 nm. The BET surface area was measured as 0.0761 m^2/g.

In Figure 1.a, XRD peaks of olive pomace before and after adsorption are given. When the peaks before adsorption are examined, it shows that it does not have a distinct crystal structure but has an irregular semi-crystalline structure close to the amorphous peaks at 15.37° and 21.88° (2θ values). It is

seen that there are at least three macromolecular structures in the structure. When examined after adsorption, it is seen that the peak at 15.37 degrees has partially disappeared. It can express that this structure adsorbs the paint. In the study conducted by Koçer et al. (2016), it was observed that the peak changes of olive pomace with similar peaks before and after adsorption were similar (Koçer and Acemioğlu 2016). It is seen that the peak of amorphous macromolecular structure around 2θ seen at 35° after adsorption disappears. The disappearance of this peak as the temperature increases can be explained by the presence of small macromolecular structures in the biosorbent that can interact with malachite green and/or dissolve in water. However, the fact that the peaks in the FT-IR spectrum do not disappear or decrease, decreases the possibility of dissolution in water.

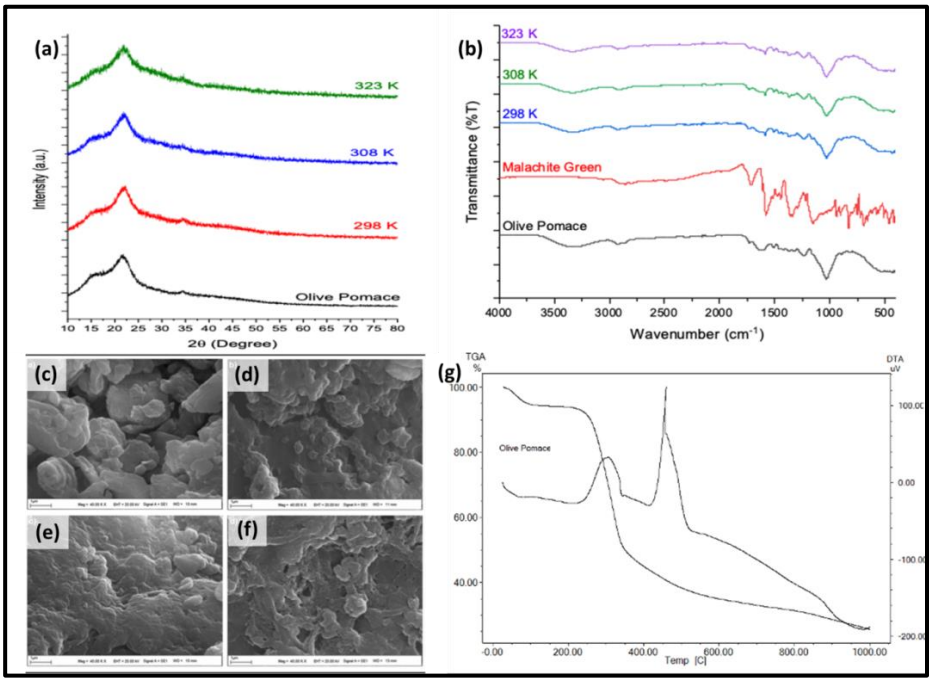

Figure 1. Characterization of olive pomace before and after adsorption **(a)** XRD spectrum **(b)** FT-IR spectrum **(c)** SEM imagine of olive pomace **(d)** SEM imagine of after malachite green adsorption at 298 K **(e)** SEM imagine of after malachite green adsorption at 298 K **(f)** SEM imagine of after malachite green adsorption at 298 K **(g)** DTA-TGA thermogram of olive pomace thermal degradation

In order to understand the adsorption mechanism (adsorption and/or adsorption) of malachite green on the surface of olive pomace FT-IR spectra before and after adsorption for 298 K, 308 K, and 323 K temperatures were obtained and shown in Figure 1.b. FT-IR spectra showed the presence of –OH groups with a wide peak at 3600-3200 cm^{-1}. It was seen that this bandgap did not change after adsorption. The peaks at 2950 cm^{-1} and 2880 cm^{-1} are caused by symmetrical and asymmetrical stretching, which show the presence of –CH and $–CH_2$ groups in the structure. The incoming bands around 1700-1600 cm^{-1} were included –NH and $–NH_2$ bonds and it was seen that this band density changes after adsorption. $-SO_2$ symmetrical and asymmetrical stretching vibrations in the structure are seen to come at 1160 cm^{-1} and 1200 cm^{-1}. C=O carboxyl groups show that the peak density at 1250 cm^{-1} changes and the peaks around 1200-100 cm^{-1} showed the presence of carboxylic acids, phenols, alcohols, and esters. This band density was also seen after adsorption. This shows that the structure of olive pomace did not change chemically in the surface groups (Koçer and Acemioğlu 2016). When the original FT-IR spectrum of olive pomace is examined, the peaks of –OH and aliphatic C-H stresses were determined clearly, but it was seen that the intensity of these peaks decreased after adsorption. This shows that malachite green dye interacts with olive pomace through physical adsorption.

The SEM images of dried olive pomace loaded with dye both before and after adsorption at 298 K, 308 K, and 323 K are shown in Figure 1.(c/d/e/f). When SEM images are examined, it was seen that olive pomace did not have a clear crystal structure and have pores. After malachite green adsorption, it was seen that the surface of the olive pomace is covered and the irregular void structures are reduced. According to SEM images it can be concluded that adsorption takes place on the surface.

Obtained TGA/DTA thermograms in this study are shown in Figure 1.g. It is considered that thermal decomposition in TGA at 100 ^oC was caused by moisture loss in the structure. 74% of the mass loss of between 230-1000 ^oC is caused by the thermal degradation of the structure. The peaks in DTA support the degradation peak in the TGA thermogram. DTA results show that the biomass has two different macromolecular structures in the temperature range of 200-400 ^oC and 400-510 ^oC. The fact that the DTA degradation peaks were not very wide indicated that the biomass structure was close to homogeneous.

3.2. Biosorption isotherms

3.2.1. Determination of dye concentration and adsorbent amount

Figure 2.a shows that the dye changes the removal potential of olive pomace at room temperature with increasing dye concentration. When 1 g olive pomace was added to the malachite green solutions prepared as 50-100-200-300-400-500 ppm at a mixing speed of 400 rpm for 120 minutes, it was seen that the highest increase is obtained at 200 ppm. After 200 ppm, the amount of adsorbent per unit mass was decreased. This was because of the dye molecules have irregular voids as can be seen from the SEM image.

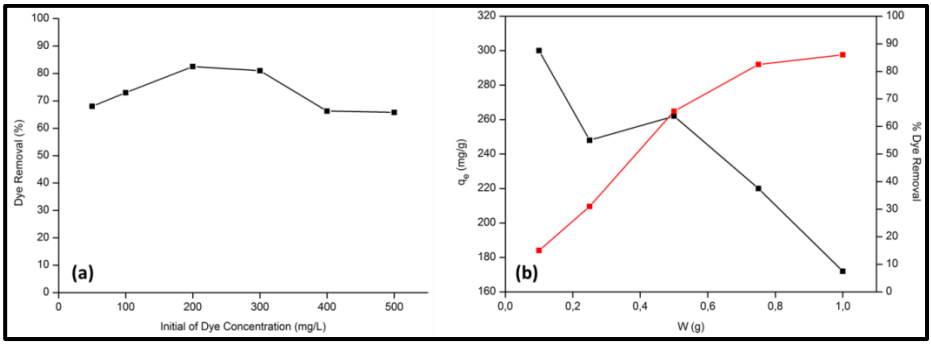

Figure 2. Determination of dye concentration (a) and adsorbent amount (b)

Adsorbent amount plays an important role in the adsorption capacity. For this reason, the effect of adsorbent amount on malachite green dye adsorption was investigated at different concentrations of 0.1: 0.25: 0.5: 0.75 and 1 g. Experiments were carried out at 200 ppm constant dye concentration, 400 rpm stirring speed and a temperature of 25^{o}C (room temperature) were also kept constant. Measurements were taken after 3 hours. It was observed that the adsorption was faster in the first minutes and then increased gradually by continuing up to 180 minutes as shown in Figure 2.b. It is seen from the Figure that there is an adverse effect between the adsorbent dose and the adsorption capacity. As the amount of adsorbent increases, the interaction between the dye and the adsorbent surface area increases. It was observed that 1 g of olive pomace has higher dye removal properties. Therefore, the amount of adsorbent in other studies was determined as 1 g.

3.2.2. Isotherm Studies

Adsorption isotherms have described the relationship between the amount of adsorbent adsorbed on the adsorbent (q_e), the constant concentration, the amount of substance, and the adsorbent concentration at equilibrium condition (C_e) (Kuang et al. 2020). Equilibrium isotherms provide information about their physicochemical properties during adsorption (Piccin et al. 2017; Limousin et al. 2007).

In this study, 200 ppm malachite green of 0.1: 0.25: 0.5: 0.75: 1 g olive pomace and adsorption equilibrium data at 298 K, 308 K, and 323 K temperatures were adapted for Langmuir, Freundlich, Dubinin-Radushkevich (D-R), and Temkin isotherms. Isotherm results equations can be described as follows successively (Dada et al. 2012).

$$q_e = q_m + \frac{q_e}{b.C_e} \quad \text{Langmuir Isotherms} \quad (1)$$

$$Inq_e = InK + \frac{1}{n}.InC_e \quad \text{Freundlich Isotherms} \quad (2)$$

$$q_e = B_T InK_T + B_T InC_e \quad \text{Temkin} \quad (3)$$

$$Inq_e = Inq_m - K_{DR}\varepsilon^2 \quad \text{Dubinin-Redushkevich} \quad (4)$$

q_e (mg/g) is the amount of dye adsorbed at equilibrium time, C_e (mg/L) is the dye concentration remaining in solution at equilibrium time. q_m is the adsorption capacity and *b* are the Langmuir constant (Vijayakumar et al. 2012) $R_L=1/(1+bC_o)$ is also the dimensionless separation factor, K denotes the adsorption capacity and n denotes Freundlich's constant (Kamga 2019) denoting density. B_T (j/mol), which is equal to RT/*b*, is the constant indicating the adsorption temperature and B_T Temkin constant is (Neto et al. 2011) and K_T (L/g) is the equilibrium binding condition. T (K) is absolute temperature; R (J/mol.K) is the ideal gas constant. ε is Polanyi potential and is equal to $R.T.\ln(1+1/C_e)$. K_{DR} (mol^2/J^2) denotes the adsorption energy, E is the average adsorption energy per molecule of the adsorbate, and is given as $E=1/(2K_{DR})^{1/2}$ (Kumar et al. 2019). The graphics of the isotherms obtained according to these calculations are shown in Figure 3.a/b/c/d and the isotherm parameters obtained in the regression analysis of all graphics are given in Table 1.

Table 1. Isotherm parameter of the adsorption of malachite green into olive pomace

Langmuir		**Freundlich**	
Parameters	**Result**	**Parameters**	**Result**
qm (mg/g)	145.57	n (g/L)	-5.814
b (L/mg)	0.233	K (mg/g)	304.996
R_L	0.021	R^2	0,99
R^2	0.99		
Temkin		**Dubinin-Redushkevich**	
Parameters	**Result**	**Parameters**	**Result**
B_T (j/mol)	-29.336	q_m (mg/g)	136.58
K_T (L/g)	$1.017x10^{-4}$	K (mol^2/J^2)	$3x10^{-5}$
b	-0.087	E (kj/mol)	0.129
R^2	0,99	R^2	0,95

The Langmuir isotherm model is a close approximation for monolayer localized adsorption (Ng et al. 2017). It allows attaching to the surface adsorbed species. By plotting q_e against q_e/C_e in the linear form equation were calculated correlation coefficient (R^2) of 0.99, q_m=145.57 mg/g, and Langmuir constant b=0.233. The dimensionless separation factor (R_L) obtained using these data was calculated as 0.021. If R_L>1, the reaction does not take place, if R_L=1, linear 0<R_L<1 means that the reaction has taken place, and if R_L=0, it means that it is an irreversible reaction (Demir et al. 2019; Pandey et al. 2010). These results show that adsorption takes place on the olive pomace surface according to the R_L value and that it conforms to this isotherm equation.

Freundlich isotherm model presumes that adsorption take places on a heterogeneous surface by the interaction between adsorbed molecules (Ayawei et al. 2017). It is not limited to the formation of single-layer adsorption, but can also be applied for multi-layer adsorption (Yahia et al. 2013). In this model, it is known that the adsorption energy is not constant and decreases with the completion of adsorption. The Freundlich isotherm, which is a linear equation, shows the adsorption capacity and n indicates the departure from the adsorption line accuracy. It is related to the heterogeneity of 1/n adsorption. n=1 indicates adsorption is linear if n<1 is adsorption chemical and n>1 indicates that

adsorption is physical (Kamga 2019). The smaller the n, the greater the heterogeneity. Depending on the fact that the n value is -5.814, it was considered as physical adsorption in temperature-dependent isotherm. K value is 304.996 mg/g and R^2 value is 0.99. It was seen that it fit this isotherm less than Langmuir.

Temkin isotherm model states that the decrease in the adsorption temperature of the molecules in the surface layer is linear and their binding energies are characterized by a uniform distribution (Piccin et al. 2011). It was assumed that the decrease in adsorption temperature is linear rather than logarithmic. Adsorption constant (B_T) is used to estimate the type of adsorption mechanism. Since B_T=-29.336 j/mol, K_T=1.017x10^{-4} L/mg, b=-0.087, and R^2=0.99, the low B_T value was due to physical adsorption and supports the result obtained from the Freundlich model.

Dubinin-Radushkevich model was a validated model for expressing Gaussian energy distribution and adsorption mechanism on a heterogeneous surface (Dada et al. 2012). It changed depending on the energy on the adsorbent surface. It was given information about whether the interaction was physical or chemical in adsorption and was shown physical adsorption when the energy value of E is less than 8 kJ/mol (Kul and Çalışkan 2009). It was appeared that q_m=136.58 mg/g, K=3x10^{-5} mol^2/J^2, E=0.129 (kj/mol) and R^2=0.95. The E value was indicated that the adsorption mechanism was a physical process. This was supported by other models.

3.3. Bioadsorption kinetics

Adsorption kinetics was described as the time-varying adsorption of the adsorbed solution concentration (Yetilmezsoy et al. 2020). In olive pomace adsorption kinetics, the adsorption kinetics of 1 g of the adsorbent amount was examined at 298 K, 308 K, and 323 K at 400 rpm. The equations of the investigated pseudo-first-order (Simonin 2016), pseudo-second-order (Robati 2013), elovic (Wu et al. 2009), and intraparticle diffusion (McKAy et al. 1987) kinetic models are respectively expressed as follows:

$$\mathrm{In}(q_e - q_t) = Inq_e - k_1 t \quad (5)$$

$$\frac{t}{q_t} = \frac{1}{k_2 q_e^2} + \left(\frac{1}{q_e}\right) t \quad (6)$$

$$q_t = \frac{In\alpha\beta}{\beta} + \left(\frac{1}{\beta}\right) Int \quad (7)$$

In Equation (5), the contact time t (min), q_e, and q_t are the amount of dye per unit mass of adsorbent at equilibrium, and k_i (mg/g) is the amount of dye per unit mass of adsorbent at any time K_T (1/min) is the pseudo first order is the speed constant. K_2 (g/mg.min) given in Equation (6) was the rate constant for the pseudo-quadratic kinetic model and was the rate constant of $h=k_2 q_e^2$, where h (mg/g.min) is the first adsorption rate. Given that in (7) was related to the surface coating and activation energy for chemisorption, α was the initial adsorption rate. Graphs made using these kinetic equations are shown in Figure 3(e/f/g). Isotherm parameters calculated from the linear regression analysis of these graphs are given in Table 2.

Table 2. Effect of temperature on kinetic parameters for adsorption malachite green of olive pomace

Kinetic Models	Concentration (mg/L)	Parameters	Temperature (K)		
			298 K	308 K	323 K
Pseudo-First-order kinetics	200	qe (mg/g)	40.358	16.844	9.796
	200	K_1 (1/min)	0.019	0.022	0.007
	200	R^2	0.86	0.60	0.13
Pseudo-second-order kinetics	200	qe (mg/g)	172.41	169.49	166.67
	200	K_2 ($x10^{-3}$) (g/mg.min)	3.06	7.41	15.65
	200	h (mg/g.min)	90.91	212.76	434.80
	200	R^2	0.99	0.99	0.99
Elovic kinetics	200	α	10495	34729	$13.18x10^6$
	200	β (g/ mg. min)	0.065	0.071	0.112
	200	R^2	0.87	0.74	0.56

As seen in Figure 3.e and Table 2, it was seen that it did not fit the pseudo-first-order kinetic model with low regression between 0.12-86 and k_1 between 0.007-0.019. Pseudo-second-order kinetic model was determined by

the chemisorption rate model (Robati 2013). Accordingly, as seen in Figure 3.f and the table, it was seen that the high regression coefficient of 0.999 and they fit between q_e, h, k_2 values fit the pseudo-second-order kinetics. Similar results were shown that biosorption fits the second-order kinetic model in the literature (Aljeboree et al. 2017). The chemical absorption of the Elovic kinetic model was represented the degree of surface coverage and activation energy for chemisorption from the Elovic constants as shown in Figure 3.g and Table 2. The low regression coefficient between 0.56-0.87 was indicated that it did not fit this model. According to these models, it can be said that chemical adsorption was not on a heterogeneous surface (Kumar et al. 2019).

3.4. Biosorption Diffusion processes

Table 3 shows the diffusion parameters for the adsorption of malachite green into olive pomace. Dye ions are affected by the adsorbent properties such as the liquid film surrounding the adsorbent particle in the solution and the diffusion from the liquid film to the adsorbent surface, the thickness of the liquid film and the reactivity of the surface (Yu et al. 2022). The reactivity of the thickness of the liquid film changes depending on the diffusion surface reaction to the pores of different sizes in the adsorbent particle and the pore structure. The larger the limiting step, the particle diffusion rate constant (g/mg.min) C, the greater the contribution of surface adsorption. While C, which represents the boundary layer effect, increased with the solution temperature, the intragranular diffusion rate constant k_i for the adsorption of malachite green on the olive pomace decreased (8).

$$q_t = k_i t^{0.5} + C \tag{8}$$

$$D_i = \frac{0.03r^2}{t_{0.5}} \tag{9}$$

where D_i is the intraparticle diffusion coefficient (cm^2/s), t0.5 is the time required to complete half the adsorption (min), and r is the radius of the adsorbent particle (cm) (9). If D_i values are in the range of 10^{-5} to 10^{-13} cm^2/s, intraparticle diffusion plays a role in the rate-limiting step, especially for chemisorption systems. Film diffusion exponents, D_1, where the intraparticle diffusion process is checked by both film and pore diffusion, can be computed by assuming that the adsorbent particle is a sphere of radius 'a' and diffusion

follows Fick's law, and the relationship between input times is delineated as (Pholosi et al. 2020).

$$\frac{q_t}{q_e} = 6(\frac{D_t}{\pi a^2})^{0.5} t^{0.5} \quad (10)$$

Similar to the trend obtained in the intraparticle diffusion graph, it was observed that malachite green has a slow final uptake into the pores. Film diffusion coefficient (D_1) values for malachite green adsorption on olive pomace at different temperatures were calculated from qt/qe slope versus $t^{0.5}$ plots (10). It was found by olive pomace that the film diffusion coefficient values for malachite green adsorption rising up with increasing solution temperature at fixed initial malachite green concentration. Michelson et al. (1975) showed that the film diffusion coefficient in the range of 10^{-6} - 10^{-8} cm^2s^{-1} indicates that film diffusion is active in the adsorption mechanism (Michelson et al.,1975).

$$B_t = -0.4997 - In(1 - \frac{q_t}{q_e}) \quad (11)$$

It is used to calculate the B_t values at different solution temperatures at a constant initial malachite green concentration, and the calculated B_t values are plotted against time for the malachite green adsorption on olive pomace (11). Here it is possible to determine whether intraparticle diffusion controls the adsorption rate. The olive press shows that the external mass transfer takes place more strongly in the rate determination stage, and as the temperature increases, the involvement of the external mass transfer decreases the transmission to the intraparticle diffusion control. Slope of B_t versus t plots (B) at different temperatures for malachite green adsorption on olive pomace, Eq. It was used to calculate the pore diffusion coefficient (12):

$$B = \pi^2 \frac{D_2}{r^2} \quad (12)$$

Pore diffusion coefficient and D_2 values were calculated for the adsorption of malachite green on olive pomace. The increase in D_2 values with

increasing temperature can be attributed to the increase in the mobility of malachite green in the solution with the increase in temperature. McKay et al., (1980) showed that the pore diffusion coefficient between 10^{-11} - 10^{-13} cm^2s^{-1} indicates that pore diffusion controls the adsorption mechanism (McKay et al. 1980). The results revealed that the D_2 values were in the range of 10^{-7}-10^{-13} cm^2s^{-1} for olive pomace, and it was seen that pore diffusion was the velocity control for olive pomace.

Table 3. Diffusion parameters for the adsorption of malachite green onto olive pomace

Diffusion Models	Concentration (mg/L)	Parameters	Temperature (K)		
			298 K	308 K	323 K
Intraparticle Diffusion	200	k_i (g/mg $min^{0.5}$)	8.66	7.25	6.03
	200	C	88.89	99.57	109.29
	200	D_i ($x10^{-11}$) (cm^2/s)	1.41	2.10	4.22
	200	R_i	0.54	0.55	0.43
	200	C/q_{ref}	0.45	0.46	0.57
	200	r^2	0.52	0.44	0.34
Film Diffusion	200	D_1 ($x10^{-4}$) (cm^2/s)	4.39	5.30	5.93
	200	r^2	0.98	0.99	0.98
Pore Diffusion	200	D_2 ($x10^{-7}$) (cm^2/s)	3.13	4.04	5.51
	200	r^2	0.91	0.95	0.96

In intraparticle diffusion, we can examine the liquid phase boundary layer in 3 different steps, as shown in Figure 3.h and Table 4.

The bulk diffusion region widely was reflected the film diffusion where the adsorbent migrates to the outer surface of the sorbent and the particle diffusion where it is transferred into its pores (Mayalagan and Karthikeyan 2013). The adsorption of absorbent molecules on the solid surface was shown in Figure 3.h and Table 4. It was seen that the thickness of the boundary layer due to the micropores of the bioadsorb has increased from 1 to 7 and it was also seen to have a high regression between 0.98-0.99. There was an increase in the kinetic speed depending on the temperature.

In the pore diffusion region, it was seen that the values of k decrease between 6-13 and the thickness of the boundary layer increases. Regression values were low as they were in the range of 86-89 compared to the first region. In the equilibrium religion, it was observed that the boundary layer thickness increased significantly between 162-165. Since the speed constant decreases too much, this region can be neglected. When the table below was examined for the intraparticle model, it was seen that the adsorption progresses in the later stages when the dye molecules start to attach to the surface at the beginning of the adsorption and the boundary layer thickness to the surface increases in the equilibrium phase.

It was an expected result that the boundary layer thickness increases with temperature, and it was due to the increasing kinetic energy that the molecules want to take more space on the surface for a lower entropy. This situation was an expected result.

3.5. Biosorption Thermodynamic

Thermodynamic analyzes were carried out at three different temperatures: 298 K, 303 K and 323 K. Thermodynamic parameters such as standard free energy change (ΔG^o), enthalpy change (ΔH^o) and entropy change (ΔS^o) were calculated using the following equations (13).

$$K_D = \frac{q_e}{C_e} \tag{13}$$

K_D (dispersion coefficient) was revealed the affinity of the adsorbent surface. The Gibbs free energy (14) was found in the following equation and shown in the Table 5.

$$\Delta G^O = -RTInK_D \tag{14}$$

The values of ΔH^o and ΔS^o were found using the Van't Hoff equation (15).

$$InK_D = \frac{\Delta S^o}{R} - \frac{\Delta H^o}{RT} \tag{15}$$

R (8.314 $J.mol^{-1}.K^{-1}$) was the gas constant and T (K) was the absolute temperature. As can be seen in Figure 3.k, $\ln K_D$ against 1/T was graphed linearly, and ΔH^o and ΔS^o values were found from the slope and shift of the obtained line.

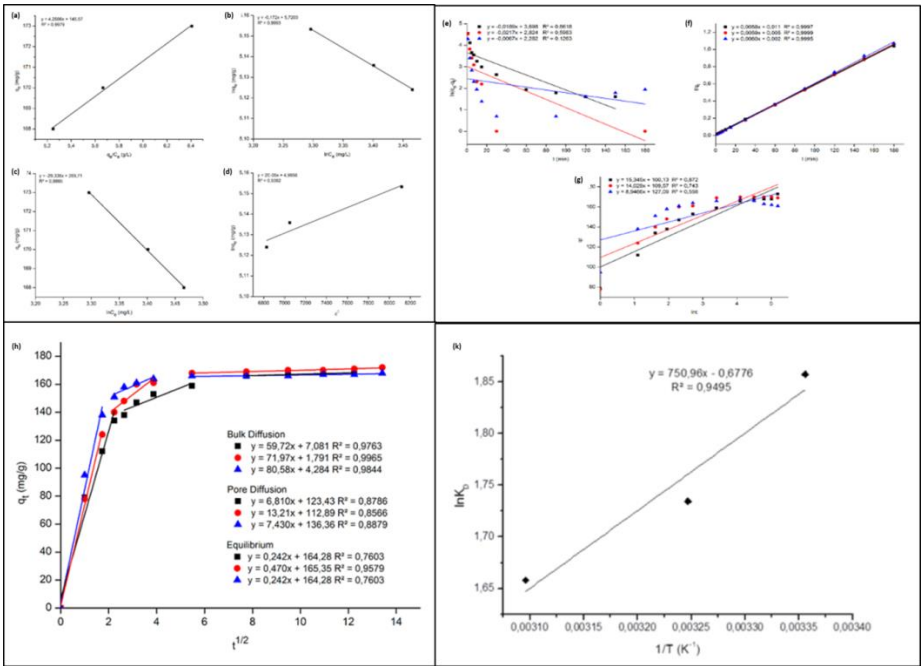

Figure 3. The isotherm plots of adsorption (a) Langmuir isotherm, (b) Freundlich isotherm, (c) Temkin isotherm, (d) Dubinin-Redushkevich isotherm, the isotherm plots of biosorption kinetics (e) Pseudo-First-order kinetic equation (f) Pseudo-second-order kinetics (g) Elovic kinetics models, the liquid phase boundary layer in 3 different steps (bulk diffusion, pore diffusion, equilibrium) (h), Van't Hoff plots of malachite green adsorption onto olive pomace for initial dye concentration at natural pH (k)

Table 4. Intraparticle diffusion portions of olive pomace

Temperature	C_o (mg/L)	Intraparticle Diffusion								
		Bulk Diffusion			Pore Diffusion			Equilibrium		
		K_i (g/ mg. min)	C	R^2	K_i (g/ mg. min)	C	R^2	K_i (g/ mg. min)	C	R^2
298 K	200	59.716	7.08	0.98	6.81	123.43	0.88	0.48	162.45	0.92
308 K	200	71.97	1.79	0,99	13.21	112.89	0.86	0.47	165.35	0.96
323 K	200	80.58	4.28	0.99	7.43	136.36	0.89	0.24	164.28	0.76

Table 5. Thermodynamic parameters for the adsorption of malachite green onto olive pomace

Conc. (mg/L)	ΔH (kJ/mol)	ΔS (kJ/mol)	298 K	303 K	323 K	298 K	303 K	323 K
			ΔG (kJ/mol)	ΔG (kJ/mol)	ΔG (kJ/mol)	K_c	K_c	K_c
200	-6244	-5.634	-4602	-4272	-3807	6.407	5.667	5.25

ΔG^o values were found to be negative from malachite green in olive pomace adsorption. In this case, the adsorption process takes place automatically. ΔH^o and ΔS^o values were also negative. A negative ΔH^o value indicates that the reaction proceeds exothermically. The change in ΔS^o shows that the irregularity increases due to its heterogeneous micropores (Feng et al. 2017). It was seen that K_c values change depending on the adsorption to the intermolecular surface depending on the temperature (Du et al. 2019).

Table 6. Some studies of raw and modified olive pomace

Adsorbents	Dye	Temperature (K)	q_{max} (mg/g)	References
K_2CO_3-activated olive pomace boiler ash	Acid Blue 29	303	38.48	Al-Ghouti and Al-Absi (2020)
	Methylene Blue		149.11	
Olive Pomace	Reactive Dye RR198	303	41,38	Akar et al. (2009)
Olive Pomace (after solvent extraction)	Methylene Blue	298	42.30	Banat et al. (2007)
Raw Olive Pomace	Methylene Blue	303	10,08	Kalipci (2016)
Modification Raw Olive Pomace			73,08	
Olive Pomace	Basic Green 4	323	41.66	Kocer and Acemioğlu (2016)
Black Olive Stones	Methylene Blue	318	458	Al-Ghouti and Al-Absi (2020)
Green Olive Stone			525	
Mango Stone	Crystal Violet	306	352.79	Shoukat et al. (2017)
Mango stone ash	Acid Blue 193	298	7.59	Puari and Rattan (2012)
Orange peel	Direct red 23	298	10.72	Arami et al. (2005)
	Direct red 80		21.05	
	Acid violet 17		19.18	
Olive Pomace	Malachite Green	298	173	This work
		308	170	
		323	168	

4. CONCLUSIONS

The production of waste is increasing globally across various industries, leading to the generation of different types of waste. One such waste is Olive Pomace, which constitutes the solid waste byproduct of the olive industry. Researchers have extensively explored the use of waste materials as adsorbents, focusing on their structural properties. This study can be divided into two main parts: the examination of the structural characteristics of olive pomace and the evaluation of its biosorption capabilities. Olive pomace retains its original structure without undergoing any pre-processing. This approach aims to minimize additional environmental pollution and avoid incurring extra costs by directly using industrial waste to mitigate other industrial waste. Structural analysis of olive pomace was conducted both before and after biosorption studies. The analysis revealed that olive pomace possesses an irregular structure and lacks a complete crystalline arrangement. This suggests that the interaction between olive pomace and malachite green is primarily physical in nature.

Various parameters, including dye concentration, the quantity of olive pomace biosorbent, contact time, and temperature, were studied. The initial dye concentration was set at 200 ppm, with 1 gram of olive pomace as the chosen biosorbent quantity, and a contact time of 180 minutes. Experimental data were analyzed using different isotherms, including Langmuir, Freundlich, Temkin, and Dubinin-Redushkevich. The analysis resulted in R^2 values of 0.97, 0.75, 0.77, and 0.88, respectively, indicating that the Langmuir isotherm provides the most accurate description of the biosorption data. The kinetics of malachite green dye biosorption onto olive pomace were investigated at three different temperatures: 298 K, 308 K, and 323 K. High correlation coefficients close to 1 were obtained for all temperatures, confirming the suitability of the pseudo-second-order kinetic model. The intraparticle diffusion model was employed to assess the biosorption mechanism. As temperature increased, the boundary layer thickness also increased, with the maximum boundary layer value calculated as 165.35 at 308 K. The ΔG_o value was found to be negative at all three temperatures studied, indicating that the biosorption process occurs spontaneously. When compared to other biosorbent materials (as detailed in Table 6), it was evident that the biosorption of malachite green dye onto olive pomace yielded successful results. Olive pomace's molecular structure can

effectively facilitate malachite green biosorption without the need for any pre-treatment.

CRediT authorship contribution statement

A.Y., Conceptualization, Methodology, Visualization, Investigation, Writing – original draft, **S.S.,** Conceptualization, Methodology, Investigation, Writing – original draft, **T. D.,** Conceptualization, Validation, Supervision, Writing – review & editing, **Y. Ö.,** Validation, Supervision, **E. B.,** Validation, Review & editing, **M. S.,** Supervision, Funding acquisition, Review & editing.

DECLARATION OF INTEREST STATEMENT

The authors declare that they have no known competing financial interests or personal relationships that could have appeared to influence the work reported in this paper.

ACKNOWLEDGEMENTS

A.Y and **S.S.** contributed equally to this work. The authors would like to thank Inonu University Scientific Research Projects Coordination Unit for providing financial support for this research project with Project number **FDK-2020-2114**. In addition, it would like to thank Inonu University Scientific and Technological Research Center and Iskenderun Technical University Science and Technology Application and Research Center for providing device support for material characterization.

REFERENCES

Adebayo M. A., Adebomi, J. I., Abe, T. O., Areo, F. I. 2020. Removal of aqueous Congo red and malachite green using ackee apple seed–bentonite composite. *Colloid and Interface Sci Commun 38:100311*. https://doi.org/10.1016/j.colcom.2020.100311

Ahmad, R., Kumar, R. 2010. Adsorption studies of hazardous malachite green onto treated ginger waste. *J Environ Manag 91:1032–1038*. https://doi.org/10.1016/j.jenvman.2009.12.016

Akar, T., Tosun, I., Kaynak, Z., Ozkara, E., Yeni, O., Sahin, E. N., Akar, S. T. 2009. An attractive agro-industrial by-product in environmental cleanup: Dye biosorption potential of untreated olive pomace. *J Hazardous Mat 166(2-3):1217-1225*. https://doi.org/10.1016/j.jhazmat.2008.12.029

Al-Ghouti, M. A., Al-Absi, R. S. 2020. Mechanistic understanding of the adsorption and thermodynamic aspects of cationic methylene blue dye onto cellulosic olive stones biomass from wastewater. *Scientific Reports 10(1):1-18*. https://doi.org/10.1038/s41598-020-72996-3

Aljeboree, A.M., Alshirifi, A. N., Alkaim, A. F. 2017. Kinetics and equilibrium study for the adsorption of textile dyes on coconut shell activated carbon. *Arabian J Chemist 10(2):3381-3393*. https://doi.org/10.1016/j.arabjc.2014.01.020

Arami, M., Limaee, N. Y., Mahmoodi, N. M., Tabrizi, N. S. 2005. Removal of dyes from colored textile wastewater by orange peel adsorbent: equilibrium and kinetic studies. *Journal of Colloid and interface Sci 288(2):371-376*. https://doi.org/10.1016/j.jcis.2005.03.020

Ayawei, N., Ebelegi, A. N., Wankasi, D. 2017. Modelling and Interpretation of Adsorption Isotherms. *Hindawi J Chemist 11:3039817*. https://doi.org/10.1155/2017/3039817

Aygün, A., Yenisoy-Karakaş, S., Duman. I. 2003. Production of granular activated carbon from fruit stones and nutshells and evaluation of their physical, chemical and adsorption properties. *Microporous and mesoporous mater 66(2-3):189-195*. https://doi.org/10.1016/j.micromeso.2003.08.028

Baccar, R., Blánquez, P., Bouzid, J., Feki, M., Sarrà, M. 2010. Equilibrium, thermodynamic and kinetic studies on adsorption of commercial dye by activated carbon derived from olive-waste cakes. *Chem Eng 165(2):457-464.* https://doi.org/10.1016/j.cej.2010.09.033

Banat, F., Al-Asheh, S., Al-Ahmad, R., Bni-Khalid, F. 2007. Bench-scale and packed bed sorption of methylene blue using treated olive pomace and charcoal. *Bioresource technol 98(16):3017-3025.* https://doi.org/10.1016/j.biortech.2006.10.023

Banerjee, M., Bar, N., Das, S. K. 2021. Cu(II) Removal From Aqueous Solution Using The Walnut Shell: Adsorption Study, Regeneration Study, Plant Scale-Up Design, Economic Feasibility, Statistical, and GA-ANN Modeling. *Int J Environ Res 15:875–891.* https://doi.org/10.1007/s41742-021-00362-w

Bello, O. S., Ahmad, M. A. 2011. Adsorption of dyes from aqueous solution using chemical activated mango peels. *In: 2nd international conference on environmental science and technology (ICEST) 2:108–113.*

Bello, O. S., Ahmad, M. A. 2012. Coconut (Cocos nucifera) shell based activated carbon for the removal of malachite green dye from aqueous solutions. *Sep Sci Technol 47:903–912.* https://doi.org/10.1080/01496395.2011.630335

Bello, O. S., Fatona, T. A., Falaye, F. S., Osuolale, O. M., Njoku, V. O. 2012. Adsorption of eosin dye from aqueous solution using groundnut hull-based activated carbon: kinetic, equilibrium, and thermodynamic studies. *Environ Eng Sci 29:186–194.* https://doi.org/10.1089/ees.2010.0385

Berrios, M., Martin, M. A., Martin, A. 2012 Treatment of pollutants in wastewater: Adsorption of methylene blue onto olive-based activated carbon. *J Industrial and Eng Chemist 18(2):780-784.* https://doi.org/10.1016/j.jiec.2011.11.125

Bharathi, K. S., Ramesh, S.T. 2013. Removal of dyes using agricultural waste as low-cost adsorbents: a review. *Applied Water Sci 3(4):773-790.* https://doi.org/10.1007/s13201-013-0117-y

Bhatnagar, A., Kaczala, F., Hogland, W., Marques, M., Paraskeva, C. A., Papadakis, V. G., Sillanpää, M. 2014. Valorization of solid waste products from olive oil industry as potential adsorbents for water

pollution control—a review. *Environ Sci and Pollution Res 21(1):268-298.* https://doi.org/10.1007/s11356-013-2135-6

Culp, S. J., Blankenship, L. R., Kusewitt, D. F., Doerge, D. R., Mulligan, L. T., Beland, F. A. 1999. Toxicity and metabolism of malachite green and leucomalachite green during short-term feeding to Fischer 344 rats and B6C3F1 mice. *Chemico-biological interactions 122(3):153-170.* https://doi.org/10.1016/S0009-2797(99)00119-2

Dada, A. O., Olalekan, A. P., Olatunya, A. M., Dada, O. 2012. Langmuir, Freundlich, Temkin and Dubinin–Radushkevich Isotherms Studies of Equilibrium Sorption of Zn^{2+} Unto Phosphoric Acid Modified Rice Husk. *IOSR Journal of Applied Chemist (IOSR-JAC) 3(1):38-45.*

Dakroury, G. A., Abo-Zahra, S. F., Hassan, H. S. 2020. Utilization of olive pomace in nano MgO modification for sorption of Ni (II) and Cu (II) metal ions from aqueous solutions. *Arabian J Chemist, 13(8):6510-6522.* https://doi.org/10.1016/j.arabjc.2020.06.008

Das, A., Mondal, C., Roy, S. 2015. Pretreatment Methods of Ligno-Cellulosic Biomass: A Review. *J Eng Sci & Technol Rev 8(5):141-165.*

Demir, F., Laçin, Ö., Bastaban, B. 2019. Determined of Equilibrium Adsorption Isotherm Model Pertechnetate Oxoanion Onto Activated Carbon. *Sinop Uni J Nat Sci 4(1):37-46.* https://doi.org/10.33484/sinopfbd.486647

Demiral, I. 2011. Methylene blue adsorption from aqueous solution using activated carbon prepared from olive bagasse. *Fresenius Environmental Bulletin 20(1): 127-134.*

Din, A. T. M., Hameed, B. H., Ahmad, A. L. 2009. Batch adsorption of phenol onto physiochemical-activated coconut shell. *J. Hazard Mater 161:1522–1529.* https://doi.org/10.1016/j.jhazmat.2008.05.009

Du, X., Wu, T., Sun, F., Hou, Z., Liu, Z., Huo, L., Hao, Y., Zha, Y. 2019. Adsorption Equilibrium and Thermodynamic Analysis of CO_2 and CH_4 on Qinshui Basin Anthracite, *Hindawi Geofluids 2019:1-14.* https://doi.org/10.1155/2019/8268050

Feng, Z., Cai, T., Zhou, D., Zhao, D., Zhao, Y., Wang, C. 2017. Temperature and deformation changes in anthracite coal after methane adsorption. *Fuel 192:27–34.* https://doi.org/10.1016/j.fuel.2016.12.005

Fernandez, M. E., Murguía, M. C. 2020. Biosorption of an anionic dye by peanut shell modified with gemini surfactants: A study on the stability of the modification and the removal efficiency. *J Molecular Liquids 317:114262.* https://doi.org/10.1016/j.molliq.2020.114262

Fiol, N., Villaescusa, I., Martínez, M., Miralles, N., Poch, J., Serarols, J. 2006. Sorption of Pb (II), Ni (II), Cu (II) and Cd (II) from aqueous solution by olive stone waste. *Separation and Purification technol 50(1):132-140.* https://doi.org/10.1016/j.seppur.2005.11.016

Gadekar, M. R., Ahammed, M. M. 2020. Use of water treatment residuals for colour removal from real textile dye wastewater. *Applied Water Sci 10(7):1-8.* https://doi.org/10.1007/s13201-020-01245-9

Hamdaoui, O., Saoudi, F., Chiha, M., Naffrechoux, E. 2008. Sorption of malachite green by a novel sorbent, dead leaves of plane tree: Equilibrium and kinetic modeling. *Chemical Eng J 143(1-3):73-84.* https://doi.org/10.1016/j.cej.2007.12.018

Hawari, A., Khraisheh, M., Al-Ghouti, M. A. 2014. Characteristics of olive mill solid residue and its application in remediation of Pb^{2+}, Cu^{2+} and Ni^{2+} from aqueous solution: Mechanistic study. *Chemical Eng J 251:329-336.* https://doi.org/10.1016/j.cej.2014.04.065

Hawari, A., Rawajfih, Z., Nsour, N. 2009. Equilibrium and thermodynamic analysis of zinc ions adsorption by olive oil mill solid residues. *J Hazardous Mat 168(2-3):1284-1289.* https://doi.org/10.1016/j.jhazmat.2009.03.014

Inamuddin, A. M. 2019. Xanthan gum/titanium dioxide nanocomposite for photocatalytic degradation of methyl orange dye. *Int J of Biol Macromol 121:1046–1053.* https://doi.org/10.1016/j.ijbiomac.2018.10.064

Ismail. M., Akhtar, K., Khan, M. I., Kamal, T., Khan, M. A. M., Asiri, A., Seo, J., Khan, S. B. 2019. Pollution, toxicity and carcinogenicity of organic dyes and their catalytic bio-remediation. *Current Pharmaceutical Design 25(34):3645-3663.* https://doi.org/10.1016/j.ijbiomac.2018.10.064

Jiang, Q., Chen, S., Deng, X., Feng, Y., Reddy, N., Zhu, Q., Liu, W., Qiu, Y. 2019. A sustainable low temperature yarn reinforcing process to reduce water and energy consumptions and pollution in the textile industry. *J Cleaner Product 210:646-652.* https://doi.org/10.1016/j.jclepro.2018.11.034

Kalipci, E. 2016. Removal of methylene blue from aqueous solutions with natural olive pomace modified with ultrasounds and acid. *Environment Protection Engineering, 42(3):* DOI:10.5277/epe160301

Kamga, T. F. 2019. Modeling adsorption mechanism of paraquat onto Ayous (Triplochiton scleroxylon) wood sawdust. *Appl Water Sci 9:1*. https://doi.org/10.1007/s13201-018-0879-3

Kapdan, I. K., Kargi, F. 2002. Simultaneous biodegradation and adsorption of textile dyestuff in an activated sludge unit. *Process Biochemist 37(9):973-981*. https://doi.org/10.1016/S0032-9592(01)00309-0

Karta, M., Depci, T., Karaca, H., Onal, M., Coskun, M. A. 2016. Co-liquefaction Behaviour of Elbistan Lignite and Olive Bagasse. *In IOP Conference Series: Earth and Environ Sci 44(5):052047*. doi:10.1088/1755-1315/44/5/052047

Kiliç, F., and Sarici-Özdemir, Ç. 2016. Experimental and modeling studies of methylene blue adsorption onto particles of peanut shell. *Particulate Science and Technology. 34:6, 658-664,* DOI: 10.1080/02726351.2015.1102188

Koçer, O., Acemioğlu, B. 2016. Adsorption of Basic green 4 from aqueous solution by olive pomace and commercial activated carbon: process design, isotherm, kinetic and thermodynamic studies. *Desalination and Water Treatment 57(35):16653-16669.* https://doi.org/10.1080/19443994.2015.1080194

Kuang, Y., Zhang, X., Zhou, S. 2020. Adsorption of Methylene Blue in Water onto Activated Carbon by Surfactant Modification. *Water 2020 12:587.* https://doi.org/10.3390/w12020587

Kul, A. R., Caliskan, N. 2009. Equilibrium and Kinetic Studies of the Adsorption of Zn(II) Ions onto Natural and Activated Kaolinites, *Adsorption Sci & Technol 27:1.* https://doi.org/10.1260/026361709788921632

Kumar, K. V., Gadipelli, S., Wood, B., Ramisetty, K. A., Stewart, A. A., Howard, C. A., Brett, D. J. L., Rodriguez-Reinoso, F. 2019. Characterization of the adsorption site energies and heterogeneous surfaces of porous materials. *J Mater Chem A 7:10104-10137.* DOI: 10.1039/C9TA00287A

Lellis, B., Fávaro-Polonio, C. Z., Pamphile, J. A., Polonio, J. C. 2019. Effects of textile dyes on health and the environment and bioremediation potential of living organisms. *Biotechnol Res and Innovation 3(2):275-290.* https://doi.org/10.1016/j.biori.2019.09.001

Limousin, G., Gaudet, J-P., Charlet, L., Szenknect, S., Barthes, V., Krimissa, M. 2007. Sorption isotherms: A review on physical bases, modeling and measurement. *Applied Geochemist 22:249–275.* https://doi.org/10.1016/j.apgeochem.2006.09.010

Maiyalagan, T., Karthikeyan, S. 2013. Film pore diffusion modeling for sorption of azo dye on to exfoliated graphitic nanoplatelets. *Indian J technol 20:7-14.*

Marrakchi, F., Bouaziz, M., Hameed, B. H. 2017. Adsorption of acid blue 29 and methylene blue on mesoporous K_2CO_3-activated olive pomace boiler ash. *Colloids and Surfaces A: Physicochem and Eng Aspects 535:157-165.* https://doi.org/10.1016/j.colsurfa.2017.09.014

Martín-Lara, M. A., Blázquez, G., Ronda, A., Pérez, A., Calero, M. 2013. Development and characterization of biosorbents to remove heavy metals from aqueous solutions by chemical treatment of olive stone. *Industrial & Eng Chemist Res 52(31):10809-10819.* https://doi.org/10.1021/ie401246c

Mashkoor, F., Nasar, A., Inamuddin, A. A. M. 2018. Exploring the reusability of synthetically contaminated wastewater containing crystal violet dye using tectona grandis sawdust as a very low-cost adsorbent. *Sci Rep 8(1):1–16.* https://doi.org/10.1038/s41598-018-26655-3

McKay, G., Otterburn, M. S., Aga, J. A. 1987. Intraparticle diffusion process occurring during adsorption of dye stuffs. *Water Air Soil Pollut 36:381–390.* https://doi.org/10.1007/BF00229680

McKay, G., Poots, V. J. P. 1980. Kinetics and diffusion processes in colour removal from effluent using wood as an adsorbent. *J Chem Technol Biotechnol 30:279–292.* https://doi.org/10.1002/jctb.503300134.

Michelson, L. D., Gideon, P. G., Pace, E. G., Kutal, L. H. 1975. Removal of Soluble Mercury from Wastewater by Complexing Techniques, *vol. 74 US Department Industry water research and technology Bull.*

Moreno-Sader, K., Alarcón-Suesca, C., González-Delgado, Á. D. 2020. Application of environmental and hazard assessment methodologies

towards the sustainable production of crude palm oil in North-Colombia. *Sustainable Chemist and Pharmacy 15:100221*. https://doi.org/10.1016/j.scp.2020.100221

Neto, V. O. S., Oliveira, A. G., Teixeira, R. N. P., Silva, M. A. A., Freire, P. T. C., Keukeleire, D. D., Nascimento, R. F. 2011. Use of coconut bagasse as alternative adsorbent for separation of copper(II) ions from aqueous solutions: Isotherms, kinetics, and thermodynamic studies. *BioRes. 6(3), 3376-3395*.

Ng, K. C., Burhan, M., Shahzad, M. W., Ismail, A. B. 2017. A Universal Isotherm Model to Capture Adsorption Uptake and Energy Distribution of Porous Heterogeneous Surface. *Sci Rep 7:10634*. https://doi.org/10.1038/s41598-017-11156-6.

Nuhoglu, Y., Malkoc, E. 2009. Thermodynamic and kinetic studies for environmentaly friendly Ni (II) biosorption using waste pomace of olive oil factory. *Bioresource Technol 100(8):2375-2380*. https://doi.org/10.1016/j.biortech.2008.11.016

Okeowo, I. O., Balogun, E. O., Ademola, A. J., Alade, A. O., Afolabi, T. J., Dada, E. O., Farombi, G. F. 2020. Adsorption of Phenol from Wastewater Using Microwave-Assisted Ag–Au Nanoparticle-Modified Mango Seed Shell-Activated Carbon. *Int J Environ Res 14:215–233*. https://doi.org/10.1007/s41742-020-00244-7

Önal, Y. 2006. Kinetics of adsorption of dyes from aqueous solution using activated carbon prepared from waste apricot. *J Hazardous mater 137(3):1719-1728*. https://doi.org/10.1016/j.jhazmat.2006.05.036

Pagnanelli, F., Mainelli, S., Vegliò, F., Toro, L. 2003. Heavy metal removal by olive pomace: biosorbent characterisation and equilibrium modelling. *Chem eng sci 58(20):4709-4717*. https://doi.org/10.1016/j.ces.2003.08.001

Pagnanelli, F., Toro, L., Veglio, F. 2002. Olive mill solid residues as heavy metal sorbent material: a preliminary study. *Waste Management 22(8):901-907*. https://doi.org/10.1016/S0956-053X(02)00086-7

Pandey, P. K., Sharma, S. K., Sambi, S. S. 2010. Kinetics and equilibrium study of chromium adsorption on zeoliteNaX. *Int J Environ Sci Tech 7(2): 395-404.* https://doi.org/10.1016/S0956-053X(02)00086-7

Pholosi, A., Naidoo, E. B., Ofomaja, A. E. 2020. Intraparticle diffusion of Cr(VI) through biomass and magnetite coated biomass: A comparative kinetic and diffusion study. *South African J Chem Eng 32:39–55.* https://doi.org/10.1016/j.sajce.2020.01.005

Piccin, J. S., Cadaval, T. R. S., Pinto, L. A. A., Dotto, G. L. 2017. Adsorption Isotherms in Liquid Phase: Experimental, Modeling, and Interpretations. In: Bonilla-Petriciolet A., Mendoza-Castillo D., Reynel-Ávila H. (eds) *Adsorption Processes for Water Treatment and Purification. Springer, Cham.* https://doi.org/10.1007/978-3-319-58136-1_2

Piccin, J. S., Dotto, G. L. L., Pinto, A. A. 2011. Adsorption isotherms and thermochemical data of fd&c red n° 40 binding by chitosan. *Brazilian J Chem Eng 28(02):295 - 304.* http://dx.doi.org/10.1590/S0104-66322011000200014.

Ponraj, C., Vinitha, G., Daniel, J. 2017. A review on the visible light active $BiFeO_3$ nanostructures as suitable photocatalyst in the degradation of different textile dyes. *Environ Nanotechnol Monit Manag Manag 7:110–120.* https://doi.org/10.1016/j.enmm.2017.02.001

Purai, A., Rattan, V. K. 2012. Biosorption of leather Dye (Acid Blue 193) from aqueous solution using ash prepared from cow dung, mango stone, parthenium leaves and activated carbon. *Indian chem eng 54(3):190-209.* https://doi.org/10.1080/00194506.2011.696368

Rizzi, V., D'agostino, F., Fini, P., Semeraro, P., Cosma, P. 2017. An interesting environmental friendly cleanup: The excellent potential of olive pomace for disperse blue adsorption/desorption from wastewater. *Dyes and Pigments 140:480-490.* https://doi.org/10.1016/j.dyepig.2017.01.069

Robati, D. 2013. Pseudo-second-order kinetic equations for modeling adsorption systems for removal of lead ions using multi-walled carbon nanotube. *J Nanostruct Chem 3:55.* https://doi.org/10.1186/2193-8865-3-55

Sarici-Özdemir, Ç., and Önal, Y. 2018. Study to observe the applicability of the adsorption isotherms used for the adsorption of medicine organics onto activated carbon. *Particulate Science and Technology. 36:2, 254-261.* DOI: 10.1080/02726351.2016.1246497

Sawa, Y., Hoten, M. 2001. Antibacterial activity of basic dyes on the dyed acrylic fibers. *Sen-I Gakkaishi 57(5):153-158.*

Sayğılı, H., Güzel, F., Önal, Y. 2015. Conversion of grape industrial processing waste to activated carbon sorbent and its performance in cationic and anionic dyes adsorption. *J Cleaner Production 93:84-93.* https://doi.org/10.1016/j.jclepro.2015.01.009

Shoukat, S., Bhatti, H. N., Iqbal, M., Noreen, S. 2017. Mango stone biocomposite preparation and application for crystal violet adsorption: a mechanistic study. *Microporous and Mesoporous Mater 239:180-189.* https://doi.org/10.1016/j.micromeso.2016.10.004

Simonin, J. P. 2016. On the comparison of pseudo-first order and pseudo-second order rate laws in the modeling of adsorption kinetics. *Chem Eng J 300:254-263.* https://doi.org/10.1016/j.cej.2016.04.079

Srivastava, S., Sinha, R., Roy, D. 2004. Toxicological effects of malachite green. *Aquatic toxicology 66(3):319-329.* https://doi.org/10.1016/j.aquatox.2003.09.008

Thiruchelvi, R., Venkataraghavan, R., Sharmila, D. 2020. Optimization of environmental parameters by Plackett-Burman design and response surface methodology for the adsorption of Malachite green onto Gracilaria edulis. *Materials Today: Proceedings.* https://doi.org/10.1016/j.matpr.2020.07.448

Uğurlu, M., Gürses, A., Doğar, Ç. 2007. Adsorption studies on the treatment of textile dyeing effluent by activated carbon prepared from olive stone by $ZnCl_2$ activation. *Coloration Technol 123(2):106-114.* https://doi.org/10.1111/j.1478-4408.2007.00072.x

Uzunkavak, O., Özdemir, G. 2019. Removal of lead and cadmium ions from aqueous solutions by olive pomace as a low-cost biosorbent. *J Turkish Chem Society Section B: Chem Eng 2(2):121-132.*

Uzunkavak, O., Patterer, M., Medici, F., Özdemir, G. 2019. Modeling of single and binary adsorption of lead and cadmium ions onto modified olive pomace. *Doi Numarası:* 10.5004/dwt.2019.24340

Veglio, F., Beolchini, F., Prisciandaro, M. 2003. Sorption of copper by olive mill residues. *Water Res 37(20):4895-4903.* https://doi.org/10.1016/S0043-1354(03)00414-7

Vijayakumar, G., Tamilarasan, R., Dharmendirakumar, M. 2012. Adsorption, Kinetic, Equilibrium and Thermodynamic studies on the removal of

basic dye Rhodamine-B from aqueous solution by the use of natural adsorbent perlite. *J Mater Environ Sci 3(1):157-170.*

Wu, F. C., Tseng, R. L., Juang, R. S. 2009. Characteristics of Elovich equation used for the analysis of adsorption kinetics in dye-chitosan systems. *Chem Eng J 150:366–373.* https://doi.org/10.1016/j.cej.2009.01.014

Yahia, M. B., Torkia, Y. B., Knani, S., Hachicha, M. A., Khalfaoui, M., Lamine, A. B. 2013. Models for Type VI Adsorption Isotherms from a Statistical Mechanical Formulation. *J Adsorption Sci & Technol 31:4.* https://doi.org/10.1260/0263-6174.31.4.341

Yetilmezsoy, K., Özçimen, D., Koçer, A. T., Bahramian, M., Kıyan, E., Akbin. H. M., Goncaloğlu, B. I. 2020. Removal of Anthraquinone Dye via Struvite: Equilibria, Kinetics, Thermodynamics, Fuzzy Logic Modeling. *Int J Environ Res 14:541–566.* https://doi.org/10.1007/s41742-020-00275-0

Yu, K. Chen, Y., Liu, J., Yang, X., Wen, S., Yue, Z. 2022. Deposition of micron-sized inertial particles on flat surfaces: effects of electrostatic forces and surface roughness. *Particulate Science and Technology.* DOI: 10.1080/02726351.2022.2147462

CHAPTER 2

REMOVALS OF SOME ORGANIC DYES NAMELY NATURAL BROWN #12 AND NATURAL YELLOW #11 USING GRAPHENE IRON OXIDE (G/Fe_3O_4) NANOCOMPOSITE

Assoc. Prof. Dr. Sevil AKÇAĞLAR[1]

DOI: https://dx.doi.org/10.5281/zenodo.10444682

[1] Dokuz Eylül University, Faculty of Engineering, Department of Mechanical Engineering İzmir, Türkiye. sevil.akcaglar@deu.edu.tr, Orcid ID: 0000-0002-5386-1862

INTRODUCTION

Dyes are widely used in various fields, such as textile, paper, rubber, plastic, leather, cosmetic, pharmaceutical and food industries, but their discharge into water could cause environmental pollutions because most of the used dyes are toxic, and some are considered carcinogenic for human health. Natural dyes have been used to color textiles from ancient times, but in the 19 th century, synthetic dyes replaced natural dyes after discovery of mauve colorant [2, 3]. Natural dye is defined as any dye, pigment, or any other substance derived from natural sources such as plants, animals and minerals are renewable and sustainable bio resource products with minimum environmental impact. They have been known since antiquity for their use in coloring of textiles, food substrate, natural protein fibers like wool, silk and cotton, and leather as well as food ingredients and cosmetics. Natural Brown #12 is used in dying various natural fibers and paper [4, 5]. Commonly called Natural Yellow #11, fustic is used for dying many natural fibers, and is commonly used for dying leather. Yellow 11" is a dye widely used in the dye industry for various printing, textile and other uses. The sources for yellow dyes are enormous [6, 7], and the plants which yield yellow dyes outnumber those yielding other colors. The chromophores of natural yellow dyes include flavonoids, carotenoids, hydroxylanthraquinones, and bis-α,β-unsaturated diketone polyphenols [8, 9].

The treatment of dye-contaminated household wastewater and industrial effluents is a challenging topic in environmental science and technology, and the removals of the hazardous dyes from wastewater have attracted many attentions in recent years [10-12]. Conventional physicochemical and biological treatment methods are ineffective for dyes removal because most of dyes are stable to photodegradation, bio-degradation and oxidizing agents. One of the most efficient methods for the removal of organic dyes is adsorption technique [13-16]. Carbon materials are known for their high adsorption capacity for organic compounds and some of them, such as activated carbon nanotubes, have

already been used as sorbents [6, 7]. An innovative technology that has gained much attention is the use of magnetic materials for some separations. Magnetic separation has advantages such as its easy phase separation with aqueous solutions and its capability of treating large amount of wastewater within a short time. In recent years, magnetic materials have found many interesting applications in the removal of organic and inorganic pollutants from waste water and for the preconcentration and subsequent assay of low levels of analyses in different samples [6-13].

One of the most dangerous wastes is dyes because of their side effects to human health and the environment [1, 2]. In addition, the colors of the dyes are simply detectable, even, at a very low level of concentrations, making them visible and unwanted. Enormous methods of dye wastewater treatment such as; anaerobic reduction, adsorption and bacterial decolonization methods have been reviewed [14-15]. Absorption and adsorption is straightforward and economic processes [4-8]. Several materials have been used at adsorption processes for instance, active carbon, natural materials, and agricultural wastes [4–6]. The rapid enhancement in nanotechnology has involved them on the wastewater treatment [7–9].

The multiwall carbon nanotube/iron oxide magnetic composites has been used for the removal of Eu(III), Ni(II) and Sr(II) from water solution [9-13]. To increase the adsorption selectivity, multiwall carbon nanotube/iron oxides was grafted with cyclodextrin and polyaniline, respectively [14-18]. The results indicated that they were promising adsorbent for the removal of 1-naphthylamine, aniline and phenol. In addition, magnetic nanoparticles are also known to be capable of adsorbing some biologically active compounds such as protein and DNA [19-22]. Graphene (G), discovered in 2004, is a kind of novel and interesting carbon material and has attracted tremendous attentions from both the experimental and theoretical scientific communities in recent years [15–17]. Graphene is one-atom-thick two-dimensional (2D) layers

of sp_2-bonded carbon that can be considered the “mother of all graphitic forms” of nano-carbon, including 0D bucky balls, 1D carbon nanotube and 3D graphite. In addition to being the principal component of most carbon based nanomaterials, graphene also exhibits extraordinary properties, such as excellent mechanical, electrical, thermal, optical properties and very high specific surface area [18-22]. As the large delocalized-electron system of G can form strong -stacking interaction with the benzene ring [18, 26], it might be also a good candidate as an adsorbent for the adsorption of benzenoid form compounds. Recently, graphene-based composites have been applied for the extraction of polycyclic aromatic hydrocarbons and pyrethroid pesticides [23-28]. The introduction of magnetic properties into G can combine the high adsorption capacity of G and the separation convenience of magnetic materials. The preparation of graphene-based magnetic nanocomposite has been reported recently Graphene/Fe_3O_4 nanocomposite was introduced for water treatment at large number literature studies as a consequence of the effective preliminary treatment to augment cleanse, and samples purify with a composite matrix [22-38]. Furthermore, G/Fe_3O_4 nanocomposite has a considerable attention because of the fundamental scientific interest and the promising applications in magnetic fluids, catalysis, sensors, biomedicine, spintronics, magnetic recording devices, and environmental remediation [11–14].

The graphene / Fe_3O_4 nanocomposite also shows advantages such as low toxicity, low cost, and eco-environmentally friendly. With the magnetic property, the new absorbent using magnetic solidphase extraction techniques could avoid time-consuming procedures and be performed directly to pretreat crude samples without the need for centrifugation or filtration, due to the facile magnetic separations and regeneration [29-32]. From literature survey, the utilization of graphene / Fe_3O_4 nanocomposite in water treatment at microscale devices has not been reported before. Several methods have been developed for the synthesis of magnetic nanoparticles at different compositions such as wet

chemical, template-directed, thermal decomposition co-precipitation, and solvothermal method [15–19].

Herein, we produced a nano-structured G/Fe_3O_4 nanocomposite for the adsorptions of natural brown #12 and natural yellow #11 dyes. The effects of the concentration of G/Fe_3O_4 nanocomposite, pH values, temperatures and the concentration of natural brown #12 and natural yellow #11 dyes on the adsorption efficiency of both dyes have been investigated. The reusability of G/Fe_3O_4 nanocomposite and two adsorption kinetic models namely intraparticle diffusion and pseudo-second-order was investigated during dye adsorptions.

MATERIALS AND METHODS

Synthesis of G/Fe_3O_4 nanocomposite

The graphene nano-plates were placed to nano Fe_3O_4 by precipitation using a sonicator. To produce G Fe_3O_4 nanocomposite, 0.5 g of FeC_{l3} and 0.5 g FeC_2 x H_2O were sonicated in 50 ml of deionized water in a sonicator with a frequency of 20 kHz and a power of 500 W for 30 min to obtain a light-brown solution at a temperature of 40 °C. Then to the solution 0,1 ml 0.2M NaOH was added. The resulting suspension was centrifuged to separate the powder product. The black product was washed and dried before use [5, 33].

Characterization of G/Fe_3O_4 nanocomposite

The nanocomposite prepared under laboratory conditions has been characterized by X-ray diffraction (XRD-6100 Shimadzu, Japan) equipped with Cu Kα radiation source with wavelength (λ = 1.5418 Å). The morphology of produced composite has been estimated by Transmission Electron Microscope (TEM) (TEM, JEM-2100). The magnetic properties were analysed using Vibrating Sample Magnetometer (VSM) at room temperature. The confirmation of graphene samples was performed by Fourier Transform Infrared/IR spectrometer (FTIR) (Vertex 70, Germany). The specific surface areas

were measured using Brunauer-Emmett Teller (BET) with an ASAP 2020 Micrometrics Instrument at 77 K.

Adsorption experiments for Natural Brown #12 and Natural Yellow #11 dyes

The removal of Natural Brown #12 and Natural Yellow #11 dyes from aqueous solutions by the magnetic graphene nanocomposite was carried. Increasing amount of G/Fe_3O_4 nanocomposite put to the 20 ml dye industry wastewater. After increasing contact times, the G/Fe_3O_4 nanocomposite was removed from the wastewater using a magnet and the concentration of the dyes in the treated wastewater was determined with UV spectrophotometer at a wavelength of 542 nm and 560 nm for natural Brown #12 and natural Yellow #11 dyes, respectively, which the maximum absorbance's were detected at these wavelengths. The removed quantity (q_e in mg L^{-1}) of the dyes by the G/Fe_3O_4 nanocomposite was calculated by $q_e = C_0 - C_{eq}$ m V (1) where C_0 (mg L^{-1}) exhibits the dye concentration at the beginning, Ce (mg L^{-1}) is the concentration of the dye remaining in the treated wastewater under steady-state conditions, V (L) is the volume of the wastewater, and m (g) is the concentration of the G/ Fe_3O_4 nanocomposite [5, 39].

Adsorption kinetic model experiments

50 mL of 50 mg L^{-1} dye industry wastewater samples containing natural Brown #12 and natural Yellow #11 dyes were mixed with increasing concentrations of G/Fe_3O_4 nanocomposite in glass reactors with a volume of 1 liter. At certain time intervals, the G/Fe_3O_4 nanocomposite was separated and removed from the solution by magnetic separation. The remaining concentration of the dye in the solution was then determined by UV–vis spectrometry and the dye adsorption percentages versus time were calculated.

Pseudo-second-order equation model

In the Pseudo-second-order equation model, the relationship between the adsorption capacity at time t, qt, and t 1/2 could be written as illustrated in Equation 1

$$\frac{t}{q_t} = \frac{1}{h} + \frac{1}{q_e}t, \quad h = k_2 q_e^2$$
$$\Rightarrow \quad q_t = q_e \frac{q_e k_2 t}{1 + q_e k_2 t},$$

Equation 1

where q_t is the amount of solute adsorbed on the surface of adsorbent (mg/g) at any time t (min), q_e is the amount of solute adsorbed at equilibrium (mg/g), k_2 is the rate constant of a pseudo-second-order equation (g/mg min) and h is the initial adsorption rate (mg/g min) [34-45].

Intraparticle diffusion model

In the intraparticle diffusion model, the relationship between the adsorption capacity at time t, q_t, and t 1/2 could be written as illustrated in Equation 2 [34-45].

$$q_t = x_i + k_p t^{1/2}$$

Equation 2

where k_p is the intraparticle diffusion constant (mg/g $min^{1/2}$) and xi is the intercept of the line which is proportional to the boundary layer thickness. The intraparticle diffusion coefficient, D, was determined by using the following equations, which are derived from Fick's law was defined with Equation 3,

$$F(t) = \frac{C_0 - C_t}{C_0 - C_e} = \frac{q_t}{q_e} = \left[1 - \exp\left(-\frac{\pi^2 Dt}{r^2}\right)\right]^{1/2}$$

or

$$\ln\left[1 - F(t)^2\right] = -\frac{\pi^2 D}{r^2} t,$$

Equation 3

where C_0 is the initial dye concentration (mg/dm^3), C_t is the dye concentration (mg/dm^3) at time t (min), C_e is the dye equilibrium concentration (mg/dm^3), D is the intraparticle diffusion coefficient (m^2 /s) and r is the particle radius assuming spherical geometry (m). A plot of ln [1 − F (t)] versus time, t, should be linear with a slop of $-\pi$ 2D/r^2, which is commonly known as the diffusional rate constant.

Reuse of G/Fe_3O_4 nanocomposite

For the desorption study, 3 mg of G/Fe_3O_4 adsorbent was added to 50 ml of the dye solutions and the mixture was shaken on a rotary shaker at 300 rpm for 30 min. The initial dye concentration and pH of the solution were 400 mg/l and 6.0, respectively. At the end of the adsorption, the dye-adsorbed G/Fe_3O_4 adsorbents were isolated from the mixture with a magnet and then were added into 20 ml ethanol at pH = 60. The suspensions were shaken on a rotary shaker at 300 rpm for 60 min. Then the supernatant solutions were analyzed by UV–vis spectrometry. Desorption efficiency of the dyse from the G/Fe_3O_4 adsorbent was calculated as the ratio of the amount of the dye desorbed to amount of the dye adsorbed and the adsorption yields were calculated [39-45].

Sampling of the dyes

The natural Brown #12 and natural Yellow #11 dyes present in a dye industry wastewater was taken with automatic sampling apparatus at four times and the mixtures of the sampling was used in the experimental analysis.

RESULTS AND DISCUSSION

Physio-chemical characterization of the G/Fe_3O_4 nanocomposite

XRD analysis results

The characteristic peak of graphene appears at 2θ = 27.009° [34]. With these analysis it was found that the peak at 2θ = 29.02° corresponding to the (0 0 3) reflection of graphene. The (0 0 3) peak ordered along the stacking direction and shows the presence of large individual graphene sheets (Figure 1a). The diffraction peak at 2θ = 26.3° (3 0 1) also originated from graphene. It was found that the diffraction peaks of the G/ Fe_3O_4 matched well with the data from the JCPDS (19-0629) for Fe_3O_4 at 2θ = 30.5°, 35.9°, 43.8°, 53.9°, 57.8°, and 63.1° can be assigned to (2 2 1), (3 1 2), (4 0 2), (4 2 3), (5 1 3), and (4 4 3) of the crystal structure of Fe_3O_4 (Figure 1b).

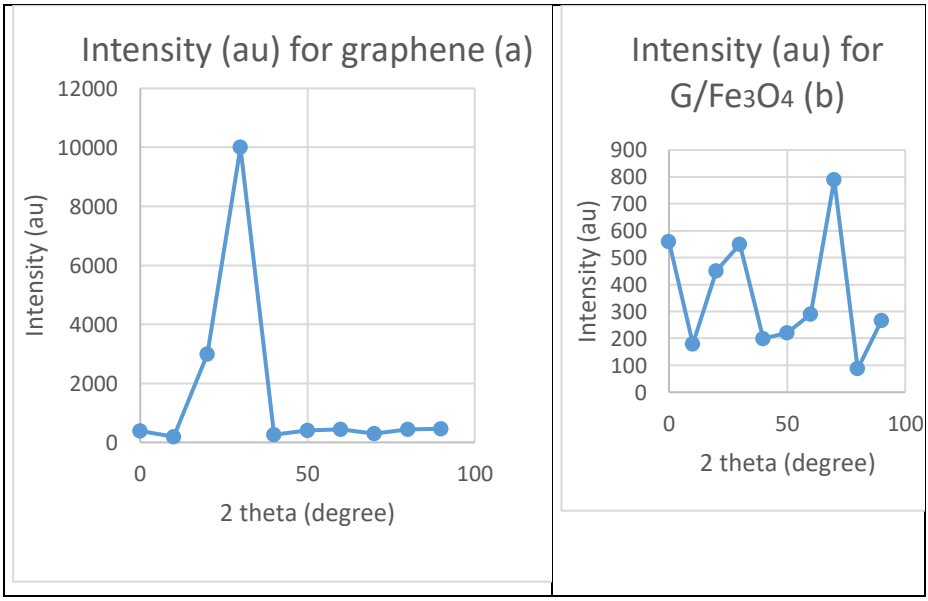

Figure 1. XRD analysis of graphene **(a)** and G/ Fe_3O_4 nanocomposite **(b)**

FTIR spectra results

FTIR spectra of G/Fe_3O_4 nanocomposite exhibited absorption bands at 464 cm^{-1} that presents the C-C=O bounds in deformation

vibration and another one around 604 cm^{-1} originated from the split of the υ1 band at 597 cm^{-1} (Figure 2). This is relevant with the Fe–O bond of Fe_3O_4 in wastewater. These results confirm that Fe_3O_4 has been prepared on the surface of graphene sheets [35]. The peak located at 1709. 97 cm^{-1} can be defined as a stretch of C =O [36, 37]. The peaks found at 3730, 3629 and 3413 cm^{-1} exhibits the O–H stretching. This indicates the presence of the functional groups having oxygen and carbon. This shows the immobilizing of Fe_3O_4 to the Graphene surfaces.

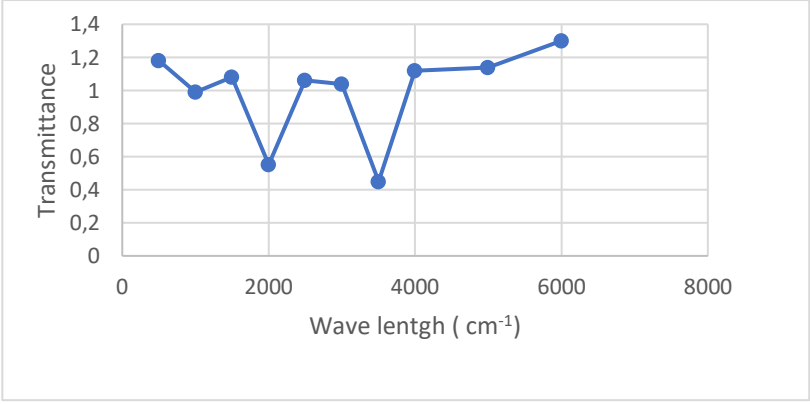

Figure 2. FTIR spectra of G/Fe_3O_4 nanocomposite

SEM analysis results

The SEM pictures for graphene and G/Fe_3O_4 nanocomposite was illustrated in Figure 3. The detected crumpled silk waves present as single-layer graphene/carbon sheets (Figure 3a). The Fe_3O_4 nanoparticles were coated on the surface of graphene to produce G/Fe_3O_4 nanocomposite (Figure 3b). The diameter of the Fe_3O_4 nanoparticles measured from SEM pictures was about 23 nm. The Fe_3O_4 nanoparticles were distributed on graphene sheets. These sheets were flat in the surface location and were located in a big area. A small part of G/ Fe_3O_4 nanocomposites were aggregated at high nanocomposite concentrations.

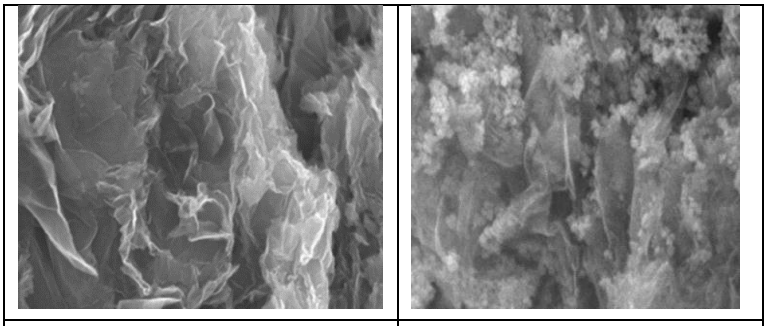

Figure 3. SEM analysis results of graphene **(a)** and G/Fe_3O_4 nanocomposite **(b)**

TEM analysis

TEM image of pure graphene surface which are as nanoplatelets structure exhibited as a soft wrinkled surface [38]. The G/Fe_3O_4 nanocomposite exhibited a flake structure having several in-plane sizes and the graphene sheets have regular layers. TEM results of grahene showed a 2D shape and conforming from carbon material existing as a monolayer in a honeycomb lattice [39].The thickness of the G/Fe_3O_4 nanocomposite was measured as 8 nm. The surface at active sides of the graphene exhibited a good at co-precipitation. The TEM images of graphene nanoparticles and G/Fe_3O_4 nanocomposites were illustrated in Figure 4a and 4b. The distribution graphene platelets in the surface of Fe_3O_4 nanoparticles were clearly detected from the TEM images.

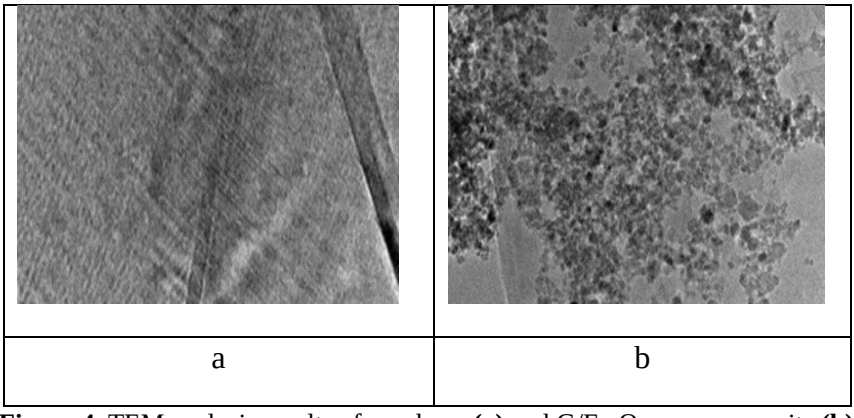

Figure 4. TEM analysis results of graphene **(a)** and G/Fe_3O_4 nanocomposite **(b)**

VSM analysis

The magnetic properties of the G/Fe_3O_4 nanocomposite were investigated using VSM at room temperature of 21º C. The hysteresis loop of the produced G/Fe_3O_4 nanocomposite exhibited in Figure 5. The produced nanocomposite exhibited advanced magnetic properties. The saturation moment of the nanocomposite as per unit mass was measured as 23.004 emu·g^{-1} [40]. The superparamagnetic properties to G/Fe_3O_4 nanocomposite used in this study provide a good separation in the presence of a magnet in a magnetic field. Magnetization of Fe_3O_4 nanoparticle and G/Fe_3O_4 nanocomposite as a function of applied magnetic field at 232 K.

Both Fe_3O_4 and G/Fe_3O_4 exhibit typical superparamagnetic behavior. The saturation magnetization intensity of Fe_3O_4 and G/ Fe_3O_4 was 70.5 and 74.3 emu g^{-1}, respectively. Under this condition an efficient separation occurred in the magnetic field.

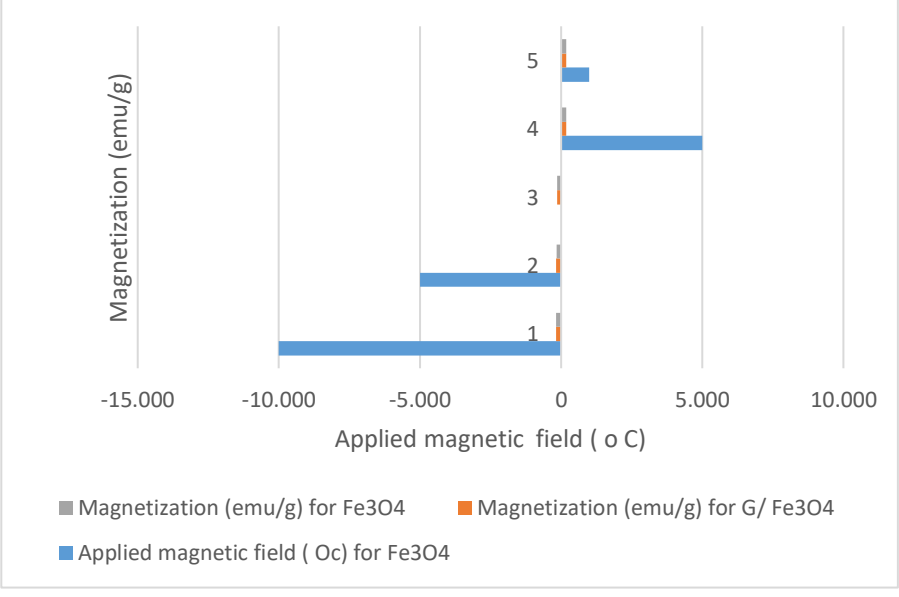

Figure 5. VSM magnetization plots of Fe_3O_4 nanomaterial and G/Fe_3O_4 nanocomposite

BET analysis

In the BET analysis, the specific surface areas of graphene and G/Fe3O4 nanocomposite were determined by taking into account the Barrett-Joyner-Helena (BJH) method and equation. The BET analysis results showed that the surface area and the total pore volume of G/Fe_3O_4 nanocomposite were bigger than that of the graphene nanomaterial (Table 1). According to BET measurements the G/Fe_3O_4 nanocomposite surface area and pore size increased up to 35.400 m2 /g and up to 17,564 nm, respectively compared to Fe_3O_4 with low surface area and pore size (13.987 m^2/g and 12.987 nm, respectively) while the graphene surface area and pore size were recorded as 16.674 m^2/g and 13,785 nm, respectively.

Table 1. BET analysis results

Compound	BET surface area (m^2/g)	Pore volume (cm^3/g)	Pore size (nm)
Graphene nanoparticle	16.674	8.987	13.785
Fe_3O_4 nanoparticle	13.987	7.675	12. 987
G/Fe_3O_4 nanocomposite	35.400	10.564	17. 564

Effects of some operational conditions on the adsorption yields of Brown #12 and natural Yellow #11 dyes

Effect of G/Fe_3O_4 concentration

The mechanism of G/Fe_3O_4 adsorption toward the organic dye may be derived from two reasons. One reason might be based on van der Waals interactions occurring between the hexagonally arrayed carbon atoms in the graphene sheet of the G/Fe_3O_4 and the aromatic backbones of the dye. The second reason might be due to the strong-stacking interaction between the benzene ring of the dye and the large delocalized-electron system of G. It was observed that the percentages

of the dye adsorbed increased as the G/Fe_3O_4 dosage was increased over the range from 0.2 to 0.4 g L^{-1} (Fig. 5). The removal ratio of the dye correspondingly increased from 82.2 to 99.4%. Above 0.4 g L^{-1} of G/Fe_3O_4, the adsorption equilibrium of the dye was reached and the removal ratio of the dye held almost constant. At 0.4 g L^{-1} of G/Fe_3O_4 dosage, about 96% of the dye was adsorbed within 10 min and 99% of the dye was adsorbed within 30 min. Therefore, 0.4 g L^{-1} G/Fe_3O_4 dosage was selected.

Table 2. Effect of G/Fe_3O_4 nanocomposite concentrations on the adsorption yields of Brown #12 and Yellow #11 dyes

G/Fe_3O_4 concentration (mg/l)	Brown #12 dye adsorption yield (%)	Yellow #11 dye adsorption yield (%)
0.05	56	61
0.1	70	72
2.0	84	80
3.0	99	97
4.0	99	97

Effect of Brown #12 and Yellow #11 dyes concentration

The concentration of nanocomposite affects the yields of dye. The adsorption yield was high at 500 and 600 mg/l dye concentration. The adsorption yields were recorded as 99% and 97% for brown #12 and yellow #11 dyes. The dye yields lowered slightly to 98% and to 96% at dye concentrations higher than 700 mg/l (Table 3). The degree of adsorption capacity increases with the increase in the adsorptive sites on the nanocomposite. The adsorption process is reduced, because of full filling of the adsorptive points in the surface of G/Fe_3O_4 nanocomposite. In the BET analysis, the specific surface areas of graphene and G/Fe3O4 nanocomposite were determined by taking into account the Barrett-Joyner-Helena (BJH) method and equation.

Table 3. Effect of of Brown #12 and Yellow #11 dyes concentrations on the adsorption yields

Brown #12 and Yellow #11 dye concentrations	Brown #12 dye adsorption yield (%)	Yellow #11 dye adsorption yield (%)
100	99	97
200	99	97
300	99	97
400	99	97
500	99	97
600	99	97
700	98	96

Effect of pH

The effect of increasing pH (4, 5, 7, and 9) values on the adsorption efficiencies of Brown #12 and Yellow #11 dye was investigated. At pH 4.00, at a constant G/Fe_3O_4 nanocomposite (3.0 mg/L) and constant dye concentrations of 400 mg/L, the adsorption yields for Brown #12 and Yellow #11 dye were detected as 93% and 89%, respectively (Table 4). Based on the maximum adsorption wavelengths of both dyes , the maximum adsorption yields was detected after 20 min adsorption time as 99% and 97% for brown #12 and yellow #11 dyes, respectively at pH=5.0 . The adsorption efficiencies were lowered at pH 7 and 9 to 90 and 88% and to 82%, 79% for brown #12 and yellow #11 dyes, respectively (Table 4). Adsorption behavior of each of the dyes was similar, when the pH was increased from 4.0 to 5.0, a big adsorption capacity was decreased. A decrease in adsorption capacity for this the aforementioned dyes were observed under neutral and basic conditions. Similar adsorption behavior with variation in solution pH has been

reported in the literature for similar dyes [2, 33]. The surface of G/Fe_3O_4 nanocomposite is positively charged (pH pzc ¼ 6.0) and dyes are negatively charged (pKa of dyes 4.3 - 5.6). The protonated groups of G/Fe_3O_4 nanocomposite are mainly carboxylic and chromatic groups [16, 17, 20]. The deprotonated groups of the dyes were probably the carbonate groups [40-46]. At high pH samples, the removal capacity of dyes was expected to decrease as the adsorbent was positively charged and dye molecules were either neutral or alkaline conditions were partially positively charged. Furthermore, the protonation of Fe_3O_4 especially those not involved in aromatic systems is also probable. The large reduction in dye adsorption at basic conditions can be attributed to electrostatic repulsion between the negatively charged G/Fe_3O_4 nanocomposite and the deprotonated dye molecules. The constant adsorption capacity of the aforementioned nanocomposite for dyes over the pH range 7-9 was an indication that the electrostatic mechanism was not the only mechanism for dye adsorption in this system. The adsorption yields of the cationic dyes are greater in the acidic medium than in neutral and alkaline media, which is correlated with the adsorption behavior of dyes on the catalyst surface.

Table 4. Effect of increasing pH on the adsorption of Brown #12 and Yellow #11 dye yields

pH	Brown #12 dye adsorption yield (%)	Yellow #11 dye adsorption yield (%)
4	93	89
5	99	97
6	88	80
7	65	62
9	45	40

Effect of temperature

The effect of temperature on the adsorption of brown #12 and yellow #11 dyes onto G/Fe_3O_4 nanocomposite was carried out at 20, 35, 55 and 65° C. The increase in the temperature led to an increase in the adsorption yields, from 89-87% to 99-97% corresponding to a temperature change from 20 to 65 °C, indicating that the adsorption of brown #12 and yellow #11 dyes onto G/Fe_3O_4 nanocomposite may be a kinetically controlled process (Table 5). The higher temperature increases the reaction rate and decreases the particle density, which forms voids, resulting in a reduced equilibrium time [15, 50-56]. The observed improvement in the adsorption capacity with increasing temperature is a kinetic result resulting from the increased monomer concentration in the dye wastewater. At low temperatures, A meaningful desorption was occurred where the dye concentration elevated (Table 5). This can be explained by a reversible adsorption or a back diffusion limiting the adsorption process [17]. At high temperatures, the adsorption capacity was enhanced by the intraparticle diffusion process and desorption phenomena totally decreased. It may be inferred that the intraparticle diffusion controlled process is a strong factor for the dye binding comparing to that for the external diffusion.

Table 5. Effect of increasing temperature on the adsorption of Brown #12 and Yellow #11 dye yields

Temperature (°C)	Brown #12 dye adsorption yield (%)	Yellow #11 dye adsorption yield (%)
20	89	87
35	96	92
55	98	95
65	99	97

Adsorption kinetic versus increasing temperature

Two different adsorption kinetics were applied to the data obtained from the experiments. Intraparticle diffusion and pseudo-second-order kinetic parameters of both dyes adsorption onto G/Fe_3O_4 nanocomposite at various dye wastewater temperatures were detected. Chemical interaction between the dye molecules and the surface of G/Fe_3O_4 nanocomposite may increase with increasing temperature and electrostatic interactions may also contribute to the enthalpy. The initial adsorption rate (h) and the calculated adsorption capacity (q_e) elevated as the temperature of the brown #12 dye wastewater increased (Table 6). The value of h increased from 10.20 to 39.88 mg/g. min and the q_e increased from 99.89 to 162.67 mg/g as the temperature increased from 20 to 66 ˚C. The experimental data relevant to the pseudo-second-order kinetic model exhibited high correlation coefficients at all temperatures (R_2 = 0.999), indicating the dyes were adsorbed by a pseudo-second-order mechanism. This suggests that the rate-limiting step is a chemical adsorption involving valence forces through sharing or exchange of electrons between brown #12 and yellow #11 dye molecules and G/Fe3O4 nanocomposite. Table 6 exhibited the adsorption kinetic versus increasing temperature for yellow #11 dyes**.** As shown in Tables 6 and 7 the adsorption capacity, q_t, and the pseudo-second-order adsorption, k_2, increase at elevated temperatures. In the intraparticle diffusion model low R_2 values and low kinetic constants for both dyes were detected (Tables 6 and 7) [50-57].

Chemical interaction between brown #12, yellow #11 dyes molecules and the G/Fe_3O_4 nanocomposite surface may increase with increasing temperature and electrostatic interactions may also contribute to the enthalpy. It is obvious that the initial adsorption rate, h, and the calculated adsorption capacity, gel, increased as the temperature of the dye solution increased (Tables 6 and 7). This suggests that the rate-limiting step is a chemical adsorption involving valence forces through

sharing or exchange of electrons between dye molecules and nanocomposite.

Table 6. Adsorption kinetic versus increasing temperature in brown #12 dye

Temperature (ºC)	Pseudo second order kinetic model				Intraparticle diffusion kinetic model	
	q_e (mg/g)	k_2(g/mg. min)	h (mg/g. min)	R_2	D / 10 - 5 (cm^2/s)	R_2
20	99.89	0.006	10.20	0.999	2.98	0.97
35	121.67	0.008	18.67	0.999	2.99	0.96
55	132.78	0.009	26.99	0.999	3.11	0.97
65	162.67	0.0019	39.88	0.999	3.22	0.94

Table 7. Adsorption kinetic versus increasing temperature in yellow #11

Temperature (ºC)	Pseudo second order kinetic model				Intraparticle diffusion kinetic model	
	q_e (mg/g)	k_2 (g/mg. min)	h (mg/g. min)	R_2	D/10-5 (cm^2/s)	R_2
20	95.67	0.005	9.68	0.999	2.89	0.96
35	128.46	0.006	16.99	0.999	2.90	0.98
55	145.89	0.007	25.44	0.999	3.01	0.96
65	159.88	0.0016	37.78	0.999	3.18	0.94

Recyclability of the G/Fe_3O_4 nanocomposite

The stability of a nanocomposite during the adsorption reaction is an important factor for a possible industrial application. To analyze the stability of the nanocomposite, prolonged recycling studies were performed. Table 8 shows the results of the repeated runs of brown #12, yellow #11 dyes adsorption using the same photocatalyst. After each cycle, the nanocomposite was collected by centrifugation and a magnet in a magnetism space and then washed with distilled water until the complete removal of dye from the catalyst. Then, the catalyst was dried at 100 ºC overnight and used for another cycle. The photocatalytic activity was found to be nearly the same up to five cycles.

Table 8. Recyclability of the G/Fe_3O_4 nanocomposite

Run cycles	Brown #12 dye adsorption yield (%)	Yellow #11 dye adsorption yield (%)
1	99	97
2	99	97
3	99	97
4	99	97
5	99	97
6	99	97
7	98	97

CONCLUSIONS

In this work, the G/Fe_3O_4 nanocomposite was prepared and investigated as effective material for removing Brown #12 and Yellow #11 dyes from a dye industry wastewater. Various characterization tools such as XRD, FTIR and TEM exhibited the formation of G/Fe_3O_4 nanocomposite. The maximum MG was 99.53% within 40 min. The nanocatalyst was reused up to six cycles without significant change in the adsorption activity, which indicates the stability of the

nanocomposite. The maximum adsorption yields of natural brown #12 and natural Yellow #11 dyes were 99% and 97%, respectively, at pH 5.00 at 65 ˚C temperature at 600 mg/l individual dye concentrations at a G/Fe_3O_4 nanocomposite concentration of 3 mg/l after 20 min adsorption time. The G/Fe_3O_4 nanocomposite has a better specific surface area, pore size and higher stability than individual graphene and Fe_3O_4 nanoparticles. G/Fe_3O_4 nanocomposite has a promising future of in the practical application for wastewater treatment.

REFERENCES

1. X.G. Luo, L.N. Zhang, High effective adsorption of organic dyes on magnetic cellulose beads entrapping activated carbon, J. Hazard. Mater. 171 (2009) 340–347.
2. V. Rocher, J.M. Siaugue, V. Cabuil, A. Bee, Removal of organic dyes by magnetic alginate beads, Water Res. 42 (2008) 1290–1298.
3. J.L. Gong, B. Wang, G.M. Zeng, C.P. Yang, C.G. Niu, Q.Y. Niu, W.J. Zhou, Y. Liang, Removal of cationic dyes from aqueous solution using magnetic multi-wall carbon nanotube nanocomposite as adsorbent, J. Hazard. Mater. 164 (2009) 1517–1522.
4. N. Yang, S. Zhu, D. Zhang, S. Xu, Synthesis and properties of magnetic Fe3O4- activated carbon nanocomposite particles for dye removal, Mater. Lett. 62 (2008) 645–647.
5. C.L. Chen, X.K. Wang, M. Nagatsu, Europium adsorption on multiwall carbon nanotube/iron oxide magnetic composite in the presence of polyacrylic acid, Environ. Sci. Technol. 43 (2009) 2362–2367.
6. C.L. Chen, J. Hu, D.D. Shao, J.X. Li, X.K. Wang, Adsorption behavior of multiwall carbon nanotube/iron oxide magnetic composites for Ni(II) and Sr(II), J. Hazard. Mater. 164 (2009) 923–928.
7. J. Hu, D.D. Shao, C.L. Chen, G.D. Sheng, J.X. Li, X.K. Wang, M. Nagatsu, Plasma-induced grafting of cyclodextrin onto multiwall carbon nanootube/iron oxides for adsorbent application, J. Phys. Chem. B 114 (2010) 6779–6785.
8. J. Hu, D.D. Shao, C.L. Chen, G.D. Sheng, X.M. Ren, X.K. Wang, Removal of 1- naphthylamine from aqueous solution by multiwall carbon nanotubes/iron oxides/cyclodextrin composite, J. Hazard. Mater. 185 (2011) 463–471.

9. D.D. Shao, J. Hu, C.L. Chen, G.D. Sheng, X.M. Ren, X.K. Wang, Polyaniline multiwalled carbon nanotube magnetic composite prepared by plasma-induced graft technique and its application for removal of aniline and phenol, J. Phys. Chem. C 114 (2010) 21524–21530.
10. J.S. Becker, O.R.T. Thomas,M. Franzreb, Protein separation with magnetic adsorbents in micellar aqueous two-phase systems, Sep. Purif. Technol. 65 (2009) 46–53.
11. R.B. Shi, Y.C. Wang, Y.L. Hu, L. Chen, Q.H. Wan, Preparation of magnetite-loaded silica microspheres for solid-phase extraction of genomic DNA from soy-based foodstuffs, J. Chromatogr. A 1216 (2009) 6382–6386.
12. K.S. Novoselov, A.K. Geim, S.V. Morozov, D. Jiang, Y. Zhang, S.V. Dubonos, I.V. Grigorieva, A.A. Firsov, Electric field effect in atomically thin carbon films, Science 306 (2004) 666–669. [16] A.K. Geim, K.S. Novoselov, The rise of graphene, Nat. Mater. 6 (2007) 183–191.
13. R.F. Service, Carbon sheets an atom thick give rise to graphene dreams, Science 324 (2009) 875–877. [18] M.J. Allen, V.C. Tung, R.B. Kaner, Honeycomb carbon: a review of graphene, Chem. Rev. 110 (2010) 132–145.
14. D.R. Dreyer, S. Park, C.W. Bielawski, R.S. Ruoff, The chemistry of graphene oxide, Chem. Soc. Rev. 39 (2010) 228–240.
15. J.M. Chen, J. Zou, J.B. Zeng, X.H. Song, J.J. Ji, Y.R. Wang, J. Ha, X. Chen, Preparation and evaluation of graphene-coated solid-phase microextraction fiber, Anal. Chim. Acta 678 (2010) 44–49.
16. J.F. Shen, Y.Z. Hu, M. Shi, N. Li, H.W. Ma, M.X. Ye, One step synthesis of graphene oxide-magnetic nanoparticle composite, J. Phys. Chem. C 114 (2010) 1498–1503.
17. X.P. Shen, J.L.Wu, S. Bai, H. Zhou, One-pot solvothermal syntheses and magnetic properties of graphene-based magnetic nanocomposites, J. Alloys Compd. 506 (2010) 136–140. [24] F.A.

He, J.T. Fan, D. Ma, L.M. Zhang, C. Leung, H.L. Chan, The attachment of Fe3O4 nanoparticles to graphene oxide by covalent bonding, Carbon 48 (2010) 3139–3144.

18. W.S. Hummers Jr., R.E. Offeman, Preparation of graphitic oxide, J. Am. Chem. Soc. 80 (1958) 1339.
19. H.F. Yang, F.H. Li, C.S. Shan, D.X. Han, Q.X. Zhang, L. Niu, A. Ivaska, Covalent functionalization of chemically converted graphene sheets via silane and its reinforcement, J. Mater. Chem. 19 (2009) 4632–4638.
20. D. Li, M.B. Muller, S. Gilje, R.B. Kaner, G.G. Wallace, Processable aqueous dispersions of graphene nanosheets, Nat. Nanotechnol. 3 (2008) 101–105.
21. V. Vadivelan, K.V. Kumar, Equilibrium, kinetics, mechanism, and process design for the sorption of methylene blue onto rice husk, J. Colloid Interface Sci. 286 (2005) 90–100
22. A. Celekli, M. Yavuzatmaca, H. Bozkurt, Kinetic and equilibrium studies on the adsorption of reactive red 120 from aqueous solution on Spirogyra majuscule, Chem. Eng. J., 152 (2009) 139–145.
23. M.Y. Arıca, G. Bayramoglu, Biosorption of reactive Red-120 dye from aqueous solution by native and modified fungus biomass preparations, J. Hazard. Mater., 149 (2007) 499–507.
24. G. Absalan, M. Asadi, S. Kamran, L. Sheikhian, D.M. Goltz, Removal of reactive red-120 and 4-(2-pyridylazo) resorcinol from aqueous samples by Fe3 O4 magnetic nanoparticles using ionic liquid as modifier, J. Hazard. Mater., 192 (2011) 476–484.
25. A. Tabak, N. Baltas, B. Afsin, M. Emirik, B. Caglar, E. Erend, Adsorption of reactive Red 120 from aqueous solutions by cetylpyridinium-bentonite, J. Chem. Technol. Biotechnol., 85 (2010) 1199–1207.
26. 5. S. Kittinaovarat, P. Kansomwan, N. Jiratumnukul, Chitosan/ modified montmorillonite beads and adsorption Reactive Red 120, Appl. Clay Sci., 48 (2010) 87–91

27. S.F. Azha, L. Sellaoui, M.S. Shamsudin, S. Ismail, A. Bonilla-Petriciolet, A.B. Lamine, A. Erto, Synthesis and characterization of a novel amphoteric adsorbent coating for anionic and cationic dyes adsorption: Experimental investigation and statistical physics modelling, Chem. Eng. J., 351 (2018) 221–229.
28. Srinivasan, Asha, and Thiruvenkatachari Viraraghavan. "Decolorization of dye wastewaters by biosorbents: a review." Journal of environmental management 91, no. 10 (2010): 1915-1929. https://doi.org/10.1016/j.jenvman.2010.05.003
29. Mondal, S. "Methods of dye removal from dye house effluent—an overview." Environmental Engineering Science 25, no. 3 (2008): 383-396.
30. Ren, Nanqi, Xianjiao Zhou, Wanqian Guo, and Shanshan Yang. "A review on treatment methods of dye wastewater [J]." CIESC Journal 1 (2013). https://doi.org/10.3969/j.issn.0438-1157.2013.01.011
31. Bitton, G. "Introduction to wastewater treatment en Wastewater microbiology." (2005): 213-223.
32. Kaegi, Ralf, Andreas Voegelin, Brian Sinnet, Steffen Zuleeg, Harald Hagendorfer, Michael Burkhardt, and Hansruedi Siegrist. "Behavior of metallic silver nanoparticles in a pilot wastewater treatment plant." Environmental science & technology 45, no. 9 (2011): 3902-3908.
33. Bauer, Christian, Thomas Heck, Niels Jungbluth, and Thomas Nemecek. "The environmental relevance of capital goods in life cycle assessments of products and services." (2007).
34. Mahmoud, Mohamed E., Mohamed S. Abdelwahab, and Eiman M. Fathallah. "Design of novel nano-sorbents based on nano-magnetic iron oxide–bound-nano-silicon oxide–immobilized-triethylenetetramine for implementation in water treatment of heavy metals." Chem.Eng Jour. 223 (2013): 318-327.

35. Tesh, Sarah J., and Thomas B. Scott. "Nano-composites for water remediation: A review." Advanced Materials 26, no. 35 (2014): 6056-6068. https://doi.org/10.1002/adma.201401376.
36. Terzi, Evren, S. Nami Kartal, Nural Yılgör, Lauri Rautkari, and Tsuyoshi Yoshimura. "Role of various nano-particles in prevention of fungal decay, mold growth and termite attack in wood, and their effect on weathering properties and water repellency." International Biodeterioration & Biodegradation 107 (2016): 77-87. https://doi.org/10.1016/j.ibiod.2015.11.010
37. Upadhyay, Ravi Kant, Navneet Soin, and Susanta Sinha Roy. "Role of graphene/metal oxide composites as photocatalysts, adsorbents and disinfectants in water treatment: a review." RSC advances 4, no. 8 (2014): 3823- 3851.
38. Abo-Zahhad, E. M., Ahmed H. El-Shazly, and M. F. El-Kady. "Synthesis and Characterization of Nanomagnetic Graphene via Co-Precipitation Technique with Aid of Ultrasound." In Materials Science Forum, vol. 860, pp. 21-24. Trans Tech Publications Ltd, 2016.
39. Bahiraei, Mehdi, and Morteza Hangi. "Flow and heat transfer characteristics of magnetic nanofluids: a review." Journal of Magnetism and Magnetic Materials 374 (2015): 125-138.
40. Dong, Yucheng, Kam Chuen Yung, Ruguang Ma, Xia Yang, Ying-San Chui, Jong-Min Lee, and Juan Antonio Zapien. "Graphene/acid assisted facile synthesis of structure-tuned Fe3O4 and graphene composites as anode materials for lithium ion batteries." Carbon 86 (2015): 310-317.
41. Jin, Bo, Guangyi Chen, Xiaobin Zhong, Yang Liu, Kaiyuan Zhou, Peng Sun, Peng Lu, Wanxi Zhang, and Jicai Liang. "Graphene/Fe3O4 hollow sphere nanocomposites as superior anode material for lithium ion batteries." Ceramics International 40, no. 7 (2014): 10359-10365.

42. Zhou, Guangmin, Da-Wei Wang, Feng Li, Lili Zhang, Na Li, Zhong-Shuai Wu, Lei Wen, Gao Qing Lu, and Hui-Ming Cheng. "Graphene-wrapped Fe3O4 anode material with improved reversible capacity and cyclic stability for lithium ion batteries." Chemistry of Materials 22, no. 18 (2010): 5306-5313. https://doi.org/10.1021/cm101532x International Journal of Solar Thermal Vacuum Eng. Vol. 2, Issue 1 (2020) 79-94 94
43. Wang, Lei, Ying Huang, Xu Sun, Haijian Huang, Panbo Liu, Meng Zong, and Yan Wang. "Synthesis and microwave absorption enhancement of graphene@ Fe 3 O 4@ SiO 2@ NiO nanosheet hierarchical structures." Nanoscale 6, no. 6 (2014): 3157-3164. https://doi.org/10.1039/c3nr05313j
44. Hu, Chuangang, Zhongyu Mou, Gewu Lu, Nan Chen, Zelin Dong, Minjia Hu, and Liangti Qu. "3D graphene–Fe 3 O 4 nanocomposites with high-performance microwave absorption." Physical Chemistry Chemical Physics 15, no. 31 (2013): 13038-13043. https://doi.org/10.1039/c3cp51253c
45. Zhu, Shenmin, Jingjing Guo, Junping Dong, Zhaowen Cui, Tao Lu, Chenglin Zhu, Di Zhang, and Jun Ma. "Sonochemical fabrication of Fe3O4 nanoparticles on reduced graphene oxide for biosensors." Ultrasonics sonochemistry 20, no. 3 (2013): 872-880. https://doi.org/10.1016/j.ultsonch.2012.12.001
46. Teo, P. S., H. N. Lim, N. M. Huang, C. H. Chia, and I. Harrison. "Room temperature in situ chemical synthesis of Fe3O4/graphene." Ceramics International 38, no. 8 (2012): 6411-6416. https://doi.org/10.1016/j.ceramint.2012.05.014
47. Wang, Jiahong, Shourong Zheng, Yun Shao, Jingliang Liu, Zhaoyi Xu, and Dongqiang Zhu. "Amino-functionalized Fe3O4@ SiO2 core–shell magnetic nanomaterial as a novel adsorbent for aqueous heavy metals removal." Journal of colloid and interface science 349, no. 1 (2010): 293-299. https://doi.org/10.1016/j.jcis.2010.05.010

48. Liang, Wenbin, Weijing Yi, Yan Li, Zhujun Zhang, Mingzhen Yang, Chuanmin Hu, and An Chen. "A novel magnetic Fe3O4@ gold composite nanomaterial: Synthesis and application in regeneration-free immunosensor." Materials Letters 64, no. 23 (2010): 2616-2619.
49. Hui, Chao, Chengmin Shen, Jifa Tian, Lihong Bao, Hao Ding, Chen Li, Yuan Tian, Xuezhao Shi, and Hong-Jun Gao. "Core-shell Fe 3 O 4@ SiO 2 nanoparticles synthesized with well-dispersed hydrophilic Fe 3 O 4 seeds." Nanoscale 3, no. 2 (2011): 701-705. https://doi.org/10.1039/c0nr00497a
50. Liu, Chenguang, Zhenning Yu, David Neff, Aruna Zhamu, and Bor Z. Jang. "Graphene-based supercapacitor with an ultrahigh energy density." Nano letters 10, no. 12 (2010): 4863-4868.
51. Li, Xuesong, Weiwei Cai, Jinho An, Seyoung Kim, Junghyo Nah, Dongxing Yang, Richard Piner et al. "Large-area synthesis of high-quality and uniform graphene films on copper foils." science 324, no. 5932 (2009): 1312-1314.
52. Nagasawa, Hideharu, Nobuaki Aoki, and Kazuhiro Mae. "Design of a new micromixer for instant mixing based on the collision of micro segments." Chemical Engineering & Technology: Industrial Chemistry-Plant Equipment- Process Engineering-Biotechnology 28, no. 3 (2005): 324-330.
53. Martínez-López, J. Israel, Mauricio Mojica, Ciro A. Rodríguez, and Héctor R. Siller. "Xurography as a rapid fabrication alternative for point-of-care devices: Assessment of passive micromixers." Sensors 16, no. 5 (2016): 705.
54. Fan, Liang-Liang, Xiao-Liang Zhu, Hong Zhao, Jiang Zhe, and Liang Zhao. "Rapid microfluidic mixer utilizing sharp corner structures." Microfluidics and Nanofluidics 21, no. 3 (2017): 36.
55. Fan, Liang-Liang, Xiao-Liang Zhu, Hong Zhao, Jiang Zhe, and Liang Zhao. "Rapid microfluidic mixer utilizing sharp corner structures." Microfluidics and Nanofluidics 21, no. 3 (2017): 36.

56. Lin, Che-Hsin, Chien-Hsiung Tsai, Chih-Wen Pan, and Lung-Ming Fu. "Rapid circular microfluidic mixer utilizing unbalanced driving force." Biomedical Microdevices 9, no. 1 (2007): 43-50. https://doi.org/10.1007/s10544-006-9009-3

57. Rahimi, Masoud, Neda Azimi, Mohammad Amin Parsamogadam, Alireza Rahimi, and Mohammad Moein Masahy. "Mixing performance of T, Y, and oriented Y-micromixers with spatially arranged outlet channel: evaluation with Villermaux/Dushman test reaction." Microsystem Technologies 23, no. 8 (2017): 3117-3130.

CHAPTER 3

REMOVAL OF AMOXICILLIN BETA-LACTAM ANTIBIOTIC USING La/Cu/Zr NANOCOMPOSITE VIA ADSORPTION

Assoc. Prof. Dr. Sevil AKÇAĞLAR[1]

DOI: https://dx.doi.org/10.5281/zenodo.10444699

[1] Dokuz Eylül University, Faculty of Engineering, Department of Mechanical Engineering İzmir, Türkiye. sevil.akcaglar@deu.edu.tr, Orcid ID: 0000-0002-5386-1862

INTRODUCTION

Organic pollutants namely emerging contaminants include pharmaceuticals, hormones, personal care products, surfactants drugs, antibiotics and pesticides [1-3]. These compounds together with their metabolites enter the environment primarily through domestic use to sewage treatment plants [1-3]. If pharmaceuticals are not quantitatively eliminated, they can be then discharged to rivers, lakes and seas which may be used as raw sources for drinking water production [6]. The presence of antibiotics in the environment has been associated to chronic toxicity and the prevalence of resistance to antibiotics in bacterial species [1-3]. Recent studies showed that numerous antibiotics have toxic nature toward algae and other lower organisms which can bring about indirect effect in long terms toward ecological sustainability [1-3]. Amoxicillin is a broad-spectrum beta-lactam antibiotic that belongs to penicillin class used as veterinary medicine for treatment of bacterial infections encountered in gastro-intestinal and systemic infections [1-3].It is also commonly employed for human prescription medicine against infections caused by bacteria [1, 2]. Recent studies have reported the presence of amoxicillin in concentrations in the range of ng L1 to mg L1 on domestic wastewater [1-3].

Bimetallic or trimetallic nanocomposites can be effectively used in the catalytic processes [4-14]. Prior works showed that bimetallic nanoparticles and trimetallic nanoparticles predominantly showed higher catalytic selectivity and activity than their monometallic nanoparticle equivalents in colloidal suspensions [15-18]. The addition of a third metal into the system allows for additional tailoring the catalyst's performance. In recent times, trimetallic nanoparticles have attracted more attention because of their outstanding electrochemical catalytic activity in comparison to bimetallic or single metal nanoparticles [20-21]. For example, Au-Pd-Pt trimetallic nanoparticles with triple-layered core–shell structure showed higher catalytic action for oxidation of methanol reactions compared with Au/Pt and Pt nanoparticles [22].

Magnetic Cu 0.4 Fe0.1 Ni0.5 nanocomposites possess an excellent catalytic performance in hydrolytic dehydrogenation of ammonia borane, surpassing its bimetallic and monometallic counterparts [23]. Hence, the mixing of three metals in nanoparticles can reliably yield significantly improved catalytic ability due to synergistic catalytic effects between the three noble metals. Catalysts with vacant cavities gained significant attention due to the numerous advantages of their hollow nanostructure, including a reduction in noble metal usage and enlarging in available surface area. Trimetallic nanoparticles improved the catalytic action for thermal decomposition of ammonium perchlorate as compared to Ni–Cu and Co–Ni bimetallic nanoparticles [24-37]. Trimetallic Ni-Mo-W/Al2O3 or alumina exhibits higher hydrotreating action than bimetallic Ni-W, Ni-Mo and commercial catalysts in thiophenehydrodesulfurization and gas oil treatment [25]. Trimetallic Pd-Ni-Ag nanoparticles supported on activated carbon were synthesized by wet-impregnation method. These carbon supported trimetallic nanoparticles were used as a heterogeneous catalyst in the catalytic decay of formic acid, which has large potential as a convenient and safe hydrogen carrier for fuel cells [26-40].

Trimetallic nanoparticles are efficient candidates for applications in adsorption, microelectronics, catalysis, electrochemistry, information storage, and metal- improved spectroscopes etc. [27-48]. The metallic nanoparticles are also finding application in environmental cleaning and monitoring they can act as sensors and photocatalyst for sensing and degradation of persistent organic pollutants. The persistent organic pollutants are synthetic chemicals such as pesticides, antibiotics, polychlorinated biphenyl, others are unintended byproducts industrial subsequent from industrial processes or combustion [28-46]. Their perseverance in the environment is significant; and it requires eras to degrade these POPs. The lipophilic nature of POPs make them more toxic for living organism as this can lead to their entrance into food chain

and biomagnification. Thus it is of prime importance to eradicate these POPs form environment.

In the present study the La/Cu/Zr trimetallics nanoparticles was generated under laboratory conditions for the adsorption ability of amoxicillin antibiotic from an antibiotic industry wastewater. The physicochemical properties of the generated nanocomposite were investigated using FTIR, XRD, SEM, TEM, XPS analysis. The effects of some operational conditions (nanocomposite concentration, amoxicillin concentration, pH, ionic strength) for maximum antibiotic yields were investigated. The reuse of the La/Cu/Zr nanocomposite was also studied. The kinetic studies were performed to detect the adsorption model of amoxicillin.

MATERIAL AND METHODS

Adsorption studies

Adsorption batch tests were performed in 250 mL glass flasks using increasing amount of amoxicillin concentrations prepared in distilled water at 25 °C versus time. Aqueous samples were taken from the solution and the concentrations were analyzed. All samples were filtered prior to the analysis.

Amoxicillin measurements

Amoxicillin concentration of all samples was determined by UVevis spectrophotometer (Thermo Scientific, Genesys 10S UVeVis) at wavelength of 230 nm.

Kinetic studies

Reaction order and rate constants are two important factors in the design of adsorption process. The amount of amoxicillin adsorbed on the activated granular carbon (q_t) at different contact times was determined by mass balance (Equation 1):

$$q_t = \frac{(Co - Ct).V}{W} \qquad \text{Equation 1}$$

where q_t is the amount of amoxicillin adsorbed at time t (mg g1), C0 and Ct are the liquid-phase concentrations of solute at the initial time and at any time t (mg L1), respectively. V is the volume of the solution (L) and W is the mass of dry adsorbent used (g). Adsorption kinetic models are used to explain the adsorption mechanism and adsorption characteristics. The pseudo-first-order rate equation (Equation 2) and pseudo-second-order model (Equation 3).

$$q_t = q_e (1- e^{-k1.t}) \qquad \text{Equation 2}$$

$$q_t = \frac{t}{\frac{1}{(k2)^2 qe^2} + \frac{t}{qe}} \qquad \text{Equation 3}$$

where q_t and qe are the amounts of amoxicillin adsorbed at time t and at equilibrium (mg g^{-1}), respectively, k_1 is the pseudo-first-order rate constant (min^{-1}) and k_2 is rate constant of the pseudo-second-order adsorption (mg g^{-1} min^{-1}).

Synthesis of La/Cu/Zr nanocomposite

The La/Cu/Zr trimetallics nanoparticles were synthesized as follows: 30 mL of 30 mM lanthanum nitrate solution was prepared in deionized water and 5.0 mL 2% (w/v) trisodium citrate in aqueous solution was added as reducing agent. The reaction mixture was heated for 1 minute in a heater at 400 W with pout. Again, 30 mL of 20 mM cupric nitrate solution and 4.0 mL of 2% trisodium citrate was added. Finally, 20 mL solution of 30 mM zirconium oxychloride and 4.0 mL of 2% trisodium citrate was added and mixture was heated again. After 5 minutes of cyclic heating, light blue colored precipitates of La/Cu/Zr trimetallic nanoparticles were obtained. The obtained precipitates were filtered and washed with distilled water several times to remove

impurities. The precipitates were dried in oven for 3 hours at 60 °C and then stored at room temperature for further studies [5, 49].

Characterization of synthesized La/Cu/Zr nanocomposite

Fourier transforms infrared (FTIR) studies

Fourier transform infrared spectrum of La/Cu/Zr TNPs was taken by KBr disc method. The La/Cu/Zr particles were thoroughly mixed with KBr, powdered and disc was formed by applying the pressure. FTIR absorption spectrum was recorded in the region of 400–4000 cm^{-1}.

X-Ray Diffraction (XRD) analysis

The X-Ray Diffraction pattern of the La/Cu/Zr was recorded with an analytical diffractrometer using Cu Kα radiation (λ = 1.5418 Å). X-ray diffraction (XRD, Panalytical's X'Pert Pro) analysis was performed out in reflectance mode.

SEM and TEM studies

For analyzing the prepared sample of La/Cu/Zr TNPs by SEM (scanning electron microscope-JSM-6100), was used to synthesize grids. The SEM graphs were obtained at different magnifications. Transmission electron microscope (TEM) observation was done on a Technai G2 20 S-TWIN at acceleration voltage of 20-200 kV. The sample was dissolved in ethanol solvent and ultrasonicated for 1 hour to prepare copper grids.

Particle size measurements

The particle size is obtained by applying Scherrer's formula: $p = k\lambda / \beta\cos\theta$ (1) Where p = particle size, β = full width at half maximum, λ = 1.54 Å for Cu Kα radiation and K = 0.9.

Sampling

Antibiotic containing wastewater samples was taken from an antibiotic produsing industry wastewater located in Gebze, Turkey.

RESULTS AND DISCUSSION

FTIR analysis results

The characteristic peak at 3429 cm^{-1} and 3424 cm^{-1} are due to O-H stretching mode of –OH group (Figure 1) **[**7-9**]**. The intense peaks observed at 889 cm^{-1}, 676 cm^{-1}, and 479 cm^{-1} indicate strong absorption bands for Zr-O, La-O and Cu-O [7-34]. FTIR spectrum display the characteristic OH stretching at 3439 cm^{-1} [23-30]. The peak at 2929 cm^{-1} is probable because of occurrence of methylene group asymmetric stretching vibrations. Peak relating to the C-O vibrations of oxygen groups was detected at 1038 cm^{-1} (Figure 1). The C-H bending vibrations are observed in range 709–605 cm^{-1}. The peaks at 1510 and 1680 cm^{-1} were probably because of C-C or C-O bond stretching of nanocomposite **[**24-37**]**. Peak presence at 719 cm^{-1} indicates C-C bending.

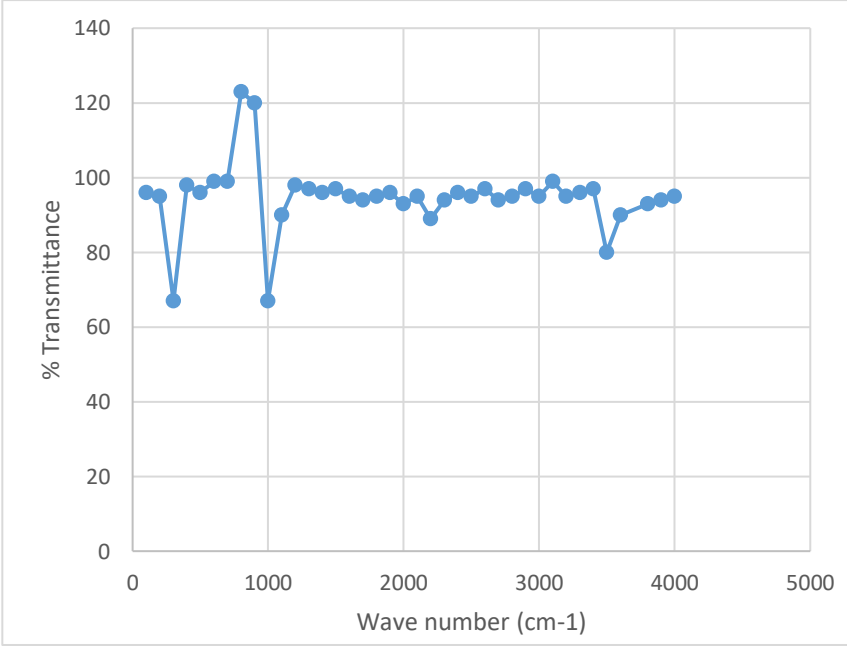

Figure 1. FTIR analysis results of La/Cu/Zr nanocomposite

XRD analysis results

The XRD pattern of the La/Cu/Zr nanocomposite shown in the Figure 2. La/Cu/Zr nanocomposite showed a crystalline structure and the peaks at 2θ = 27.09°, 30.38°, 33.86°, 43.210°, 47.50°, 50.09°, 30.19°, 50.15°, and 60.07°(Figure 2). The peaks at 2θ value of 27.08°, 30.29°, and 33.59° correspond to (003), (112) and (221) diffraction planes of lanthanum. The data is suitable with the standard JCPDS. The lattice constants were as follows: a=b= 6.1269Å and c= 2.4229 Å. The crystallite size for La nanoparticles (259.81 Å), was measured from the intense peak at 2θ=24.06°. The peaks at 2θ value 42.82°, 50.03°, and 47.02° correspond to diffraction planes (112), (202), and (223) of copper (7,46). The lattice constants were as follows: a=b=c= 2.59Å. The crystallite size for copper particles was calculated from intense peak of 230.58 Å. The peaks at 2θ value 31.07°, 50.18°, and 60.03° corresponds to (101), (112), and (211) diffraction planes for tetragonal zirconium crystal lattice [37]. The lattice constants were calculated as a=b= 1.46Å and c= 1.18Å. The crystallite size for zirconium particles as calculated from intense peak is 191.79 Å. The calculated unit cell volume for hexagonal lanthanum is 89.38 Å3, for face centered cube structure of copper is 17.37 Å3 and for tetragonal structure of zirconium is 23.9 Å3.

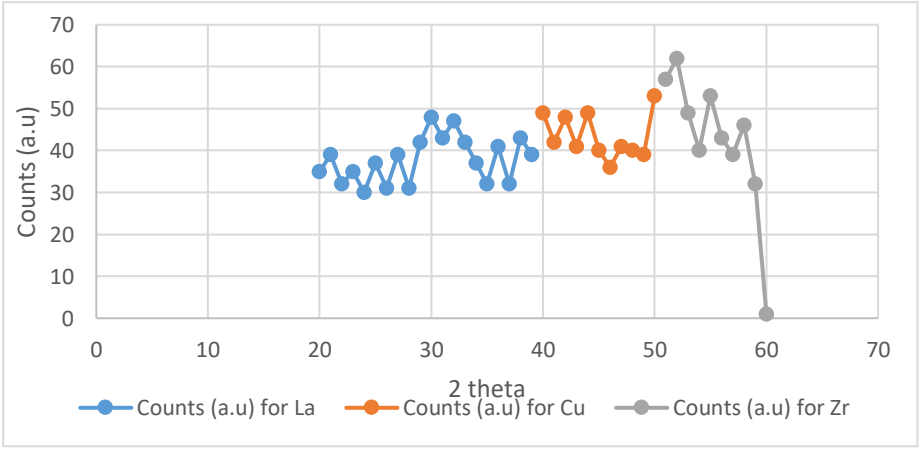

Figure 2. XRD analysis results

SEM analysis results

The SEM images of La/Cu/Zr nanocomposite were shown in Figure 3(a-b). The SEM images indicated that La/Cu/Zr consist of agglomerated structures in the range of 100 nm and 200 nm with a 50 nm of average range of subparticles. Individual nanoparticles of trimetallics are stacked on top of each other.

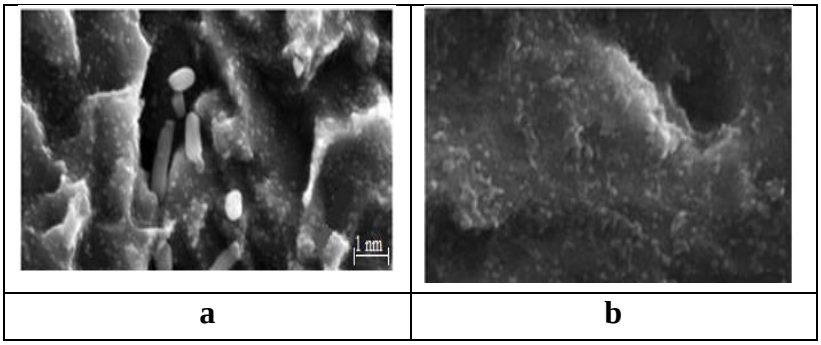

Figure 3. SEM images of La/Cu/Zr nanocomposite (a) and their agglomerated stuctures (b)

TEM images

It is found that the morphology of the nearly spherical with an average diameter of about 49 nm (Figure 4a and b)). The nanoparticles were tessellated during surface with metals in crater-like structures (20, 47, 49). A heterogeneous range of structural features were also observed for all nanoparticles in the La/Cu/Zr nanocomposite. Fine precipitates exhibited spot-shape and extend regions, while the precipitates with sizes of 2–5 nm show apparent dark contrast as illustrated in Figure 4b.The single spherical precipitation has an ordered fcc structure (32, 49).

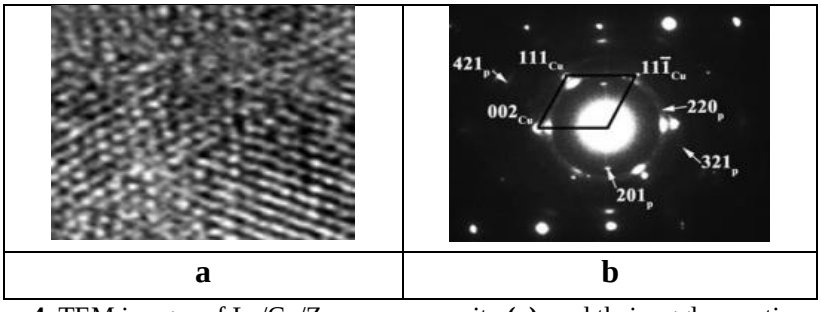

Figure 4. TEM images of La/Cu/Zr nanocomposite **(a)**, and their agglomerations **(b)**

XPS analysis results

XPS analysis illustrated in Figure 5 shows the distributions for O 1s (a), C 1s (b), La 3d(c), Cu 2p(d) and Zr 3d (e). Figure 5a, b, c, d and a demonstrates the absorptions peaks for C 1s spectra of the La/Cu/Zr nanocomposite. The deconvolution process identified three peaks in the spectra at 283.66 eV which represents the 1s-Π* transition showing the existence of C-O bond, the peak at 285.17 eV for 1s-Π transition represents C-H, C-C substituted carbonyl carbon. The peak at 287.47 eV represents 1s-3p/σ transition corresponding to C-H of aliphatic carbon of CH_3, CH_2 and CH groups. Figure 5a represents the O1s peaks [57, 58]. The peaks appear at 529.59, 531.77, 530.26 and 530.95 eV. These peaks show strong metal-oxide linkage [43]. The lanthanum showed the two sets of deconvolution peaks at 834.47 and 837.57 eV for $3d_{5/3}$ and 851.25 and 854.39 eV for $3d_{3/2}$ respectively (Figure 5c) [8-12]. Figure 5d demonstrates the XPS of copper 2p, where signals appear at 931.08 and 951.56 eV for $Cu_2P_{3/2}$ and $Cu_2P_{1/2}$, respectively [8, 32]. The $Cu_2p_{3/2}$ peak is further spilt into two peaks 931.78 and 932.06 for Cu_2^+ and CuO. The Zr 3d peaks are presented in Figure 5d two peaks appear at 181.56 and 183.98 eV for $3d_{5/2}$ and $3d_{3/2}$, respectively [4, 26].

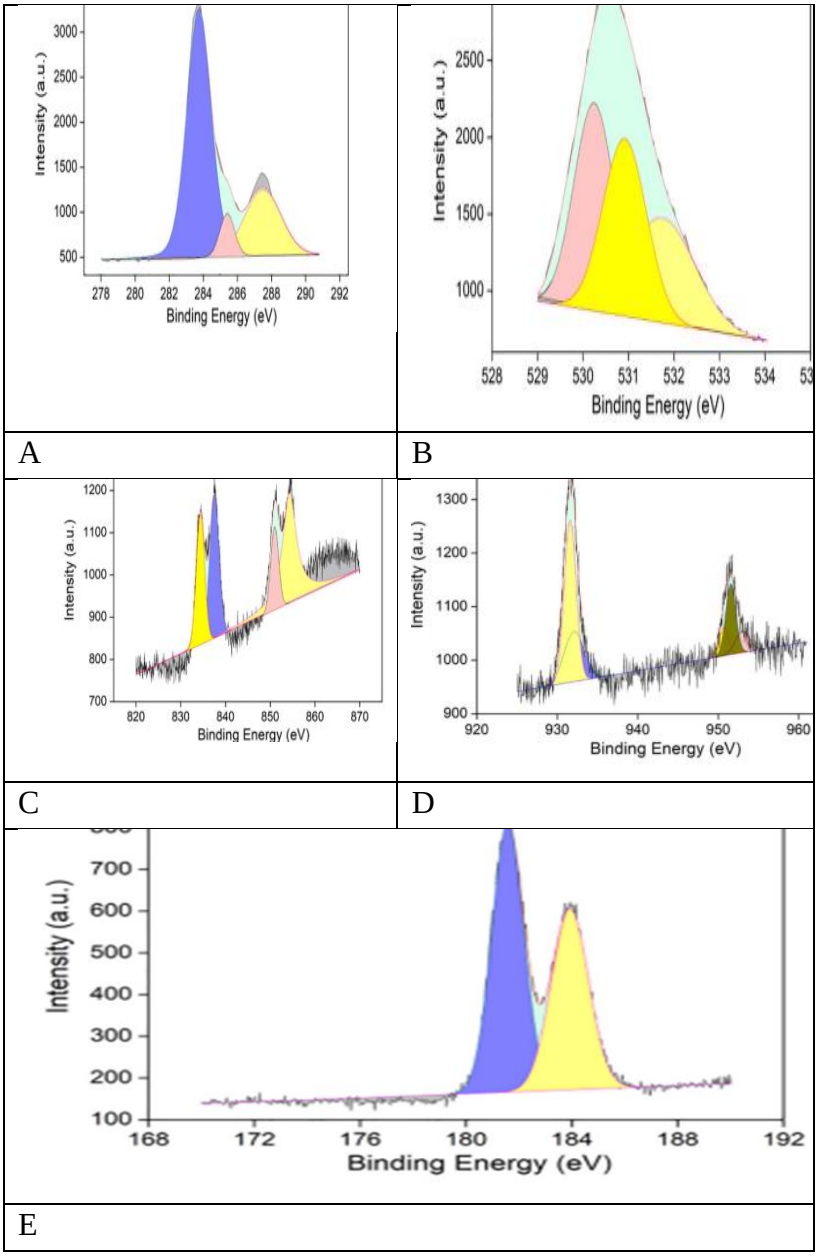

Figure 5. XPS analysis s for O 1s(a), C 1s(b), La 3d(c), Cu 2p(d) and Zr 3d (e)

Reuse of La/Cu/Zr nanocomposite

The reusability capacity of La/Cu/Zr nanocomposite in the adsorption of amoxicillin antibiotic is illustrated in Table 1 for 9 cycles. The adsorption capacity of 1.2 mg/l La/Cu/Zr nanocomposite was 99%

for adsorption of 600 mg/ amoxicillin after 16 mim adsorption. After 9 cycles of antibiotic adsorption yields was measured as 96%.

Table 1. Reusability capacity of La/Cu/Zr nanocomposite

Cycles	**Amoxicillin** adsorption yield (%)
1	99
2	99
3	99
4	99
5	99
6	99
7	99
8	98
9	96

Effect of some operational conditions on the adsorption of amoxicillin to La/Cu/Zr nanocomposite

Effect of pH and Ionic Strength on Ampicillin adsorption

The adsorption of 600 mg/l amoxicillin to 1,2 mg/l La/Cu/Zr nanocomposite was investigated within the pH range of 3.0 and 10.0 at a temperature of 25 ºC. The adsorption capacity of amoxicillin to La/Cu/Zr nanocomposite was governed by the pH. The results showed that the highest maximum adsorption capacity of amoxicillin was detected as 99% at a pH of 7.0 (Table 2). The lowest amoxicillin removal was detected as 57% at a pH of 3.0. During pH variations amoxicillin exhibited cationic, zwitterionic, and anionic forms. Amoxicillin is cationic at pH values less than 2.50, it is often zwitterionic at pH values between 2.58 and 7.0 and, it is anionic at pH values between 7.49 and 9.70. This antibiotic has a higher negative charge at pH values above 9.63 and at pH < 7.0 the surface of the La/Cu/Zr nanocomposite has a positive charge while the adsorption

capacity drops due to the electrostatic repulsion between the anionic amoxicillin and the negatively charged surface of the La/Cu/Zr nanocomposite. As a result, pH = 7.0 was selected as the optimal pH for amoxicillin adsorption onto La/Cu/Zr nanocomposite.

Table 2. Effect of Ph on the adsorption yields of amoxicillin

pH values	Amoxicillin yields (%)
3	57
7	99
10	43

Several types of ions can be affecting the adsorption yields. For this purpose, NaCl salt was employed for regulating the ionic strength of the amoxicillin containing wastewater. Accordingly, the adsorption tests were implemented at different NaCl concentrations (0.0001, 0.001, and 0.01 and 0.1 mg/l .As shown in Table 3, the adsorption yields of amoxicillin at high NaCL concentration was detected as 99% while this yield decreased slightly (90%) at low NaCl concentrations. This suggests that the saline ion concentration has an insignificant effect on the adsorption of amoxicillin onto La/Cu/Zr nanocomposite.

Table 3. Effect of ionic strength on the adsorption yields of amoxicillin

NaCl concentration (mg/l)	Amoxicillin yields (%)
0,0001	99
0,001	99
0,01	99
0,1	99

Effect of La/Cu/Zr nanocomposite and amoxicillin concentrations

The effect of the La/Cu/Zr nanocomposite concentrations (0.2, 0.5, 1.0, 1.2, 1.5 and 2.0 mg/l) on the adsorption yields were detected (Table 4).The maximum adsorption capacity was 99% at a La/Cu/Zr nanocomposite concentration of 1.2 mg/l. Then, the adsorption yields dropped slightly from 99% to 96% at 1.5 and 2.0 mg/l nanocomposite concentrations. This may be because, at low adsorbent dosages, adsorption sites are more exposed to amoxicillin antibiotics and adsorption occurs more rapidly. On the other hand, there are an additional number of unoccupied adsorption sites at higher adsorbent dosages, which reduces the adsorption capacity.

Table 4. Effect of La/Cu/Zr nanocomposite concentration on the adsorption yields of amoxicillin

La/Cu/Zr nanocomposite concentration (mg/l)	Amoxicillin yields (%)
0.2	80
0.5	85
1.0	90
1.2	99
1.5	96
2.0	96

The effect of increasing amoxicillin concentrations (40, 200, 300, 400, 500, 600, 700 and 800 mg/l) was investigated on the adsorption yields of antibiotic yields (Table 5). The adsorption capacity increased

rapidly with the increasing of the initial concentration of antibiotic then the adsorption capacity reduced sligtly at higher initial antibiotic concentrations. The adsorption capacity of 600 mg/l amoxicillin cover the 1.2 mg/l La/Cu/Zr nanocomposite was 99%. This can be attributed to gradients of large concentrations between the bulk and adsorbent particles at high initial amoxicillin concentrations. A low decrease in antibiotic yields (97%) was detected at 700 and 800 mg/l amoxicillin concentrations due to the maximum occupancy of active adsorption sites on the surface of La/Cu/Zr nanocomposite after 16 min.

Table 5. Effect of La/Cu/Zr nanocomposite concentration on the adsorption yields of amoxicillin

Amoxicillin concentration (mg/l)	Amoxicillin yields (%)
40	99
200	99
300	99
400	99
500	96
600	99
700	97
800	97

Adsorption kinetic models

The pseudo-first-order and pseudo-second-order kinetic models were used to evaluate the kinetics of amoxicillin adsorption on the surface of the of La/Cu/Zr nanocomposite. The calculated parameters and coefficients were tabulated in Table 6. The maximum amoxicillin adsorption capacity (q_e) was calculated as 456.45 mg g^{-1} at 600 mg/l

antibiotic concentration. The highest determined coefficient of R_2 was 0.999 for the pseudo-second-order kinetic model. The experimental data exhibited better data for the pseudo-second-order model in comparison with the pseudo-first-order model for antibiotic adsorption.

Table 6. Pseudo-first-order and pseudo-second-order kinetic models for amoxicillin adsorption

Amoxicillin concentration (mg/l)	Pseudo first order kinetic model				Pseudo second order kinetic model			
	K_1 (L/min)	q_e theorical (mg/g)	R_2	q_e experimental(mg/g)	K_2 (L/min)	q_e theorical (mg/g)	R_2	qe experimental(mg/g)
200	0.5634	453.45	0.99	453.44	0.0067	129.76	0.91	123.56
600	0.5897	456.45	0.99	456.42	0.0069	130.86	0.92	119.52

CONCLUSIONS

From the trimetallic nanoparticles (La, Cu and Zr) a novel nanocomposite namely La/Cu/Zr was prepared under laboratory conditions. It exhibits a excellent adsorption ability to amoxicillin antibiotic removal. The experimental data fitted better the pseudo-second-order model than pseudo-first-order model for the adsorption of amoxicillin. FTIR analyses exhibited intense peaks at 889 cm^{-1}, 676 cm^{-1} and 479 cm^{-1} while the XRD results exhibited a crystalline structure. SEM results indicated the agglomerated La/Cu/Zr with a 50 nm of average size. TEM assays showed heterogeneous range of structural

features with fine precipitates. XPS results showed peaks for O1s, lanthanum, Cu_2 $p_{3/2}$ and Zr 3d peaks.The maximum adsorption capacity of 1,2 mg/l La/Cu/Zr nanocomposite was 99% for adsorption of 600 mg/l amoxicillin after 16 min adsorption time. After 9 cycles of antibiotic adsorption yields was measured as 96% at a neutral pH at a 1.2 mg/l La/Cu/Zr nanocomposite and 600 mg/l amoxicillin concentration. With La/Cu/Zr, the antibiotics present in wastewaters can be treated effectively.

REFERENCES

1.J.Georgin , D. Stracke P. Franco, L. Meili ,Y. Dehmani , G. S. dos Reis , E.C. Lima. Main advances and future prospects in the remediation of the antibiotic amoxicillin with a focus on adsorption technology: A critical review.J of Wat. Pro. Eng..56,104407(2023)

2. C. Yang , L. Wang , Y.Yu , P. Wu , F. Wang , S.Liu, X. Luo Highly efficient removal of amoxicillin from water by Mg-Al layered double hydroxide/cellulose nanocomposite beads synthesized through in-situ coprecipitation method. Int J Biol Macromol, 15:149:93-100 (2020).

3. A. Aljeboree, A. Alshirifi, A. F. Alkaim: Removal of Pharmaceutical Amoxicillin drug by using (CNT) decorated Clay/ Fe2O3 Micro/Nanocomposite as effective adsorbent: Process optimization for ultrasound-assisted adsorption. Int. J of Pharma Res, 11(4):80-6 (2019)

4. C. Xia, W. Zhang, Z. Kang, Y. Jia, Y. Wu, R. Zhang, G. Xu, and M. Wang: High strength and high electrical conductivity Cu-Cr system alloys manufactured by hot rolling-quenching process and thermomechanical treatments. Mater. Sci. Eng., A 538, 295 (2012).

5. Z. Li, Z.Y. Pan, Y.Y. Zhao, Z. Xiao, and M.P. Wang: Microstructure and properties of high-conductivity, super-high-strength Cu-8.0Ni-1.8Si-0.6Sn-0.15Mg alloy. J. Mater. Res. 24, 2123 (2013).

6. H. Fernee, J. Nairn, and A. Atrens: Precipitation hardening of CuFe-Cr alloys, part I mechanical and electrical properties. J. Mater. Sci. 36, 2711 (2001).

7. H. Fernee, J. Nairn, and A. Atrens: Precipitation hardening of CuFe-Cr alloys, part II microstructural characterisation. J. Mater. Sci. 36, 2721 (2001).

8. Y.H. Zhao, X.Z. Liao, Z. Horita, T.G. Langdon, and Y.T. Zhu: Determining the optimal stacking fault energy for achieving high ductility in ultrafine-grained Cu-Zn alloys. Mater. Sci. Eng., A 493, 123 (2008).
9. H.T. Zhou, J.W. Zhong, X. Zhou, Z.K. Zhao, and Q.B. Li: Microstructure and properties of Cu-1.0Cr-0.2Zr-0.03Fe alloy. Mater. Sci. Eng., A 498, 225 (2008).
10. L. Arnberg, U. Backmark, N. Bäckström, and J. Lange: A new high strength, high conductivity Cu-0.5wt.% Zr alloy produced by rapid solidification technology. Mater. Sci. Eng. 83, 115 (1986).
11. M. Azimi and G.H. Akbari: Characterization of nano-structured Cu-6wt.% Zr alloy produced by mechanical alloying and annealing methods. J. Alloys Compd. 555, 112 (2013).
12. N. Muramatsu, H. Kimura, and A. Inoue: Microstructures and mechanical properties of highly electrically conductive Cu-0.5, Cu-1 and Cu-2 at% Zr alloy wires. Mater. Trans. 54, 176 (2013).
13. R. Kuzel, M. Janecek, Z. Matěj, J. Cí zek, M. Dopita, and O. Srba: Microstructure of equal-channel angular pressed Cu and Cu-Zr samples studied by different methods. Metall. Mater. Trans. A 41, 1174 (2009).
14. D.E. Tyler and W.T. Black: ASM Handbook, 10th ed. (ASM International Press, Detroit, The United States of America, 1990), p. 770. Olin Corporation.
15. V.K. Sarin and N.J. Grant: Cu-Zr and Cu-Zr-Cr alloys produced from rapidly quenched powders. Metall. Trans. 3, 875 (1972).
16. F.A. Guo, C.J. Xiang, C.X. Yang, X.M. Cao, S.G. Mu, and Y.Q. Tang: Study of rare earth elements on the physical and mechanical properties of a Cu-Fe-P-Cr alloy. Mater. Sci. Eng., B 147, 1 (2008).
17. Y. Zhang, H. Gao, Y. Kuai, Y. Han, J. Wang, B. Sun, S. Gu, and W. You: Effects of Y additions on the precipitation and recrystallization of Al-Zr alloys. Mater. Charact. 86, 1 (2013).

18. J. Lin and L. Meng: Effect of aging treatment on microstructure and mechanical properties of Cu-Ag alloys. J. Alloys Compd. 454, 150 (2008).
19. F. Bittner, S. Yin, A. Kauffmann, J. Freudenberger, H. Klauß, G. Korpala, R. Kawalla, W. Schillinger, and L. Schultz: Dynamic recrystallisation and precipitation behaviour of high strength and highly conducting Cu-Ag-Zr alloys. Mater. Sci. Eng., A 597, 139 (2014).
20. T. Fujii, H. Nakazawa, M. Kato, and U. Dahmen: Crystallography and morphology of nanosized Cr particles in a Cu-0.2% Cr alloy. Acta Mater. 48, 1033 (2000).
21. S.G. Jia, X.M. Ning, P. Liu, M.S. Zheng, and G.S. Zhou: Age hardening characteristics of Cu-Ag-Zr alloy. Met. Mater. Int. 15, 555 (2009).
22. M.Y-W. Lou and N.J. Grant: Identification of Cu5Zr phase in Cu-Zr alloys. Metall. Trans. A 15, 1491 (1984).
23. J. Ružić, J. Stašić * , V. Rajković, D. Božić, Synthesis, microstructure and mechanical properties of ZrB2 nano and microparticle reinforced copper matrix composite by in situ processings. Materials & Design, 62(), 409–415. (2014).
24. D. Zhou, F. Qiu, and Q. Jiang: Simultaneously increasing the strength and ductility of nano-sized TiN particle reinforced Al-Cu matrix composites. Mater. Sci. Eng., A 596, 98 (2014).
25. C. Xia, Y. Jia, W. Zhang, K. Zhang, Q. Dong, G. Xu, and M. Wang: Study of deformation and aging behaviors of a hot rolled-quenched Cu-Cr-Zr-Mg-Si alloy during thermomechanical treatments. Mater. Des. 39, 404 (2012).
26. X. Zhang, J. Han, L. Chen, B. Zhou, Y. Xue, and F. Jia: Effects of B and Y additions on the microstructure and properties of Cu-Mg-Te alloys. J. Mater. Res. 28, 2747 (2013).
27. J. Zhang, F. Huang, and Z. Lin: Progress of nanocrystalline growth kinetics based on oriented attachment. Nanoscale 2, 18 (2010).

28. D. Arlas and J.P. Abrlata: Cu-Zr (copper-zirconium). Bull. Alloy Phase Diagrams 11, 452 (1990).
29. A. Gaganov, J. Freudenberger, E. Botcharova, and L. Schultz: Effect of Zr additions on the microstructure, and the mechanical and electrical properties of Cu-7 wt.% Ag alloys. Mater. Sci. Eng., A 437, 313 (2006).
30. Q. Liu, X. Zhang, Y. Ge, J. Wang, and J.Z. Cui: Effect of processing and heat treatment on behavior of Cu-Cr-Zr alloys to railway contact wire. Metall. Mater. Trans. A 37, 3233 (2006).
31. Y.H. Zhao, X.Z. Liao, Z. Jin, R.Z. Valies, and Y.T. Zhu: Microstructures and mechanical properties of ultrafine grained 7075 Al alloy processed by ECAP and their evolutions during annealing. Acta Mater. 52, 4589 (2004).
32. Y.H. Zhao, J.F. Bingert, X.Z. Liao, B.Z. Cui, K. Han, A.V. Sergueeva, A.K. Mukherjee, R.Z. Valiev, T.G. Langdon, and Y.T. Zhu: Simultaneously increasing the ductility and strength of ultra-fine grained pure copper. Adv. Mater. 18, 2949 (2006).
33. H. Wen, T.D. Topping, D. Isheim, D.N. Seidman, and E.J. Lavernia: Strengthening mechanisms in a high-strength bulk nanostructured Cu-Zn-Al alloy processed via cryomilling and spark plasma sintering. Acta Mater. 61, 2769 (2013
34. J.-X. Kang, T.-W. Chen, D.-F. Zhang, L. Guo, PtNiAu trimetallic nanoalloys enabled by a digestive-assisted process as highly efficient catalyst for hydrogen generation, Nano Energy, 23 (2016) 145-152.
35. H. Zhang, N. Toshima, Preparation of novel Au/Pt/Ag trimetallic nanoparticles and their high catalytic activity for aerobic glucose oxidation, Applied Catalysis A: General, 400 (2011) 9-13.
36. G. Sharma, M. Naushad, A. Kumar, S. Devi, M.R. Khan, Lanthanum/Cadmium/Polyaniline bimetallic nanocomposite for the photodegradation of organic pollutant, Iranian Polymer Journal, 24 (2015) 1003-1013.

37 X. Liu, D. Wang, Y. Li, Synthesis and catalytic properties of bimetallic nanomaterials with various architectures, Nano Today, 7 (2012) 448-466.

38. H. Zhang, J. Okuni, N. Toshima, One-pot synthesis of Ag–Au bimetallic nanoparticles with Au shell and their high catalytic activity for aerobic glucose oxidation, Journal of Colloid and Interface Science, 354 (2011) 131-138. [

39. G. Sharma, D. Kumar, A. Kumar, A.a.H. Al-Muhtaseb, D. Pathania, M. Naushad, G.T. Mola, Revolution from monometallic to trimetallic nanoparticle composites, various synthesis methods and their applications: A review, Materials Science and Engineering: C, 71 (2017) 1216-1230.

40. A. Colombo, C. Dragonetti, M. Magni, D. Roberto, Degradation of toxic halogenated organic compounds by iron-containing mono-, bi- and tri-metallic particles in water, Inorganica Chimica Acta, 431 (2015) 48-60.

41. L. Wang, Y. Yamauchi, Strategic Synthesis of Trimetallic Au@Pd@Pt Core−Shell Nanoparticles from Poly(vinylpyrrolidone)-Based Aqueous Solution toward Highly Active Electrocatalysts, Chemistry of Materials, 23 (2011) 2457-2465.

42. N. Toshima, R. Ito, T. Matsushita, Y. Shiraishi, Trimetallic nanoparticles having a Au-core structure, Catalysis Today, 122 (2007) 239-244. [10] S. Sigurdson, V. Sundaramurthy, A.K. Dalai, J. Adjaye, Phosphorus promoted trimetallic NiMoW/γ-Al2O3 sulfide catalysts in gas oil hydrotreating, Journal of Molecular Catalysis A: Chemical, 291 (2008) 30-37.

43. W. Hong, Y. Fang, J. Wang, E. Wang, One-step and rapid synthesis of porous Pd nanoparticles with superior catalytic activity toward ethanol/formic acid electrooxidation, Journal of Power Sources, 248 (2014) 553-559.

44. H.-L. Wang, J.-M. Yan, Z.-L. Wang, Q. Jiang, One-step synthesis of Cu@FeNi core–shell nanoparticles: Highly active catalyst for hydrolytic dehydrogenation of ammonia borane, International Journal of Hydrogen Energy, 37 (2012) 10229-10235.
45. S. Singh, P. Srivastava, G. Singh, Nanorods, nanospheres, nanocubes: Synthesis, characterization and catalytic activity of nanoferrites of Mn, Co, Ni, Part-89, Materials Research Bulletin, 48 (2013) 739-746.
46. M.A. Matin, J.-H. Jang, Y.-U. Kwon, One-pot sonication-assisted polyol synthesis of trimetallic core–shell (Pd,Co)@Pt nanoparticles for enhanced electrocatalysis, International Journal of Hydrogen Energy, 39 (2014) 3710-3718.
47. G. Sharma, S. Bhogal, M. Naushad, Inamuddin, A. Kumar, F.J. Stadler, Microwave assisted fabrication of La/Cu/Zr/carbon dots trimetallic nanocomposites with their adsorptional vs photocatalytic efficiency for remediation of persistent organic pollutants, Journal of Photochemistry and Photobiology A: Chemistry, 347 (2017) 235-243.
48. V.K. Gupta, G. Sharma, D. Pathania, N.C. Kothiyal, Nanocomposite pectin Zr(IV) selenotungstophosphate for adsorptional/photocatalytic remediation of methylene blue and malachite green dyes from aqueous system, Journal of Industrial and Engineering Chemistry, 21 (2015) 957-964.
49. F. L. Aranda ,B. L. Rivas. Removal Of Amoxicillin Through Different Methods, Emphasizing Removal By Biopolymers And Its Derivatives. An Overview. J. Chil. Chem. Soc. vol.67 no.3 Concepción set. (2022)

CHAPTER 4

THE USE OF HYDROPHILIC INTERACTION METHODS IN THE ANALYSIS OF GLYCANS AND GLYCOPEPTIDES

Doç. Dr. Hacı Mehmet KAYILI[1]

DOI: https://dx.doi.org/10.5281/zenodo.10444713

[1]Karabük University, Faculty of Engineering, Department of Medical Engineering, Karabük, Türkiye. h.mehmetkayili@karabuk.edu.tr, ORCID ID: 0000-0002-6740-0645

INTRODUCTION

Hydrophilic interaction stands out as a valuable separation technique, enabling the efficient analysis of glycans and glycopeptides(Gilar et al., 2011). The fundamental principle underlying the success of hydrophilic interaction in glycan and glycopeptide analysis lies in the interaction between glycans and the stationary phase, which is primarily hydrophilic(Qing, Yan, He, Li, & Liang, 2020). Given the inherently hydrophilic characteristics of glycans, the interactions are facilitated through weak forces, predominantly involving hydrogen bonding. This method exploits the affinity of glycans for hydrophilic surfaces, allowing for enhanced separation and elucidation of their structural intricacies(Ahn, Bones, Yu, Rudd, & Gilar, 2010). The reliance on subtle interactions, such as hydrogen bonding, underscores the specificity and selectivity of hydrophilic interaction in capturing the hydrophilic nature of glycans, making it a robust tool in glycan analysis(Melmer, Stangler, Premstaller, & Lindner, 2011). The unique ability of hydrophilic interaction to harness the hydrophilic properties of glycans contributes to its effectiveness in achieving nuanced separation, providing researchers with a powerful approach for unravelling the complexities of glycan structures(Domínguez-Vega et al., 2018).

Glycosylation, a pivotal post-translational modification prevalent in organisms, exerts a profound impact on the functionality of proteins undergoing this alteration(Tian & Zhang, 2010). This process involves the covalent attachment of glycans to proteins, leading to the emergence of two distinct types of glycosylation in cellular organisms, namely *N*-linked and *O*-linked glycans, determined by the binding amino acids and atoms involved(Stavenhagen et al., 2016). The modification of proteins through glycosylation plays a crucial role in shaping cellular pathways. Notably, the glycosylation patterns of immunoglobulin G (IgG) have garnered attention due to their dynamic interplay between anti-inflammatory and pro-inflammatory features, with this property exhibiting variations linked to age and sex(Krištić et al., 2014).

Furthermore, glycans emerge as promising candidates in biomarker discovery studies(Stowell, Ju, & Cummings, 2015). Extensive research across various diseases and cancers has consistently highlighted the potential of glycans as indicative biomolecules. The evolving landscape of glycan research underscores their multifaceted role in influencing cellular functions and

responses. As our understanding deepens, the intricate connections between glycosylation patterns, disease states, and biological processes continue to unveil, positioning glycans as versatile players in both normal physiological function and pathological conditions(Pinho & Reis, 2015). This expanding knowledge paves the way for innovative diagnostic and therapeutic avenues that leverage the distinctive features of glycosylation for advancing personalized medicine and targeted interventions(Holst, Wuhrer, & Rombouts, 2015).

In this book chapter, a comprehensive exploration of the application of hydrophilic interaction for glycan analysis takes centre stage. The chapter meticulously scrutinizes the merits and demerits of employing HILIC, offering a nuanced evaluation of its advantages and disadvantages. Delving into the potential applications of hydrophilic interaction for the analysis of glycans, the discussion unfolds with a focus on the diverse scenarios where this chromatographic technique proves invaluable. By providing an in-depth examination of the capabilities and limitations inherent in hydrophilic interaction, the chapter endeavours to equip readers with a thorough understanding of the intricacies involved in utilizing this methodology for glycan analysis. Additionally, the chapter explores the horizon of possibilities that hydrophilic interaction opens up, shedding light on the promising avenues and innovative approaches that arise when deciphering the complexities of biomolecular structures.

Principle of Hydrophilic Interaction Approach

The stationary phase used in hydrophilic interaction comprises hydrophilic materials, including silica with hydroxyl groups or zwitterionic compounds(Chen et al., 2014). This hydrophilic matrix enhances the retention of polar analytes. The mobile phase in hydrophilic interaction consists of an organic solvent, such as acetonitrile or methanol, with a relatively low proportion of water. The organic content facilitates the partitioning of hydrophilic analytes onto the hydrophilic stationary phase. In the hydrophilic interaction framework, analyte retention hinges upon the extent of hydrophilicity(Liu et al., 2022). Notably, hydrophilic analytes exhibit interactions with the hydrophilic stationary phase, resulting in their delayed elution compared to less hydrophilic counterparts(Zauner, Deelder, & Wuhrer,

2011). The aqueous component in the mobile phase plays a role in modulating the strength of hydrophilic interactions(Kozlik, Goldman, & Sanda, 2018). Elevated organic content serves to amplify hydrophilic interactions, while a reduction in acetonitrile concentration accelerates analyte elution.

The retention mechanism intrinsic to hydrophilic interaction encompasses a synergistic interplay of partitioning and adsorption phenomena(Ongay, Boichenko, Govorukhina, & Bischoff, 2012). Hydrophilic analytes partition into the aqueous layer residing on the surface of the stationary phase, concurrently undergoing adsorption onto the stationary phase(Chen et al., 2014). Furthermore, the selectivity within the hydrophilic interaction is agreeable to fine-tuning through strategic adjustments in the mobile phase composition, particularly the ratio of water to organic solvent(H. M. Kayili, Ertürk, Elmaci, & Salih, 2019). This strategic adaptability lends versatility to the technique, rendering it productive for the separation of a broad spectrum of hydrophilic compounds(Boersema, Mohammed, & Heck, 2008).

Commonly Used Methodologies for the Analysis of Glycans and Glycopeptides

Glycan analysis encompasses intricate procedures, commencing with the enzymatic liberation of glycans from glycoproteins. Notably, for the release of *N*-glycans, the specific enzyme PNGase F is instrumental. However, an analogous enzymatic methodology for *O*-glycan analysis is currently unavailable. The enzymatic removal step is contingent upon the prior denaturation of proteins through the utilization of detergents, a prerequisite for productive *N*-glycan release(H Mehmet Kayili, Atakay, Hayatu, & Salih, 2022).

Sodium dodecyl sulfate (SDS) emerges as the predominant detergent employed for glycoprotein denaturation. The optimal SDS concentration preceding enzymatic treatment ranges between 0.5% and 1%(H. M. Kayili, Sakhta, & Salih, 2022). Concurrently, the incorporation of neutral detergents, such as NP-40 or Igepal CA630, becomes imperative to enhance PNGase F activity. Additionally, the introduction of a salt buffer, such as phosphate-buffered saline, into the sample at this stage is deemed essential(H. M. Kayili & Salih, 2021).

The incubation period for *N*-glycan release is contingent upon the quantities of glycoprotein and enzyme, varying from 1 hour to overnight incubation durations(H. M. Kayili et al., 2022). Alternatively, *N*-glycan release under native conditions is a viable approach, albeit necessitating extended incubation times. The duration of this process is predicated upon the intrinsic nature of the glycoprotein and enzyme interaction. This nuanced enzymatic liberation step constitutes a critical phase in glycan analysis, demanding meticulous consideration of variables such as detergent composition, incubation duration, and the nature of the glycoprotein under investigation. Conversely, *O*-glycans present in glycoproteins can be chemically released using distinct methodologies(Halim, Ruetschi, Larson, & Nilsson, 2013). Commonly employed techniques include hydrazinolysis and beta-elimination. Following the liberation of *O*-glycans through hydrazinolysis, the ensuing glycans can be subsequently labeled with a fluorophore tag(Guo, Nayak, Mao, & Li, 2021; Kozak et al., 2016). However, it is noteworthy that the beta-elimination approach does not afford the opportunity to label *O*-glycans with a fluorophore tag post-release.

The widely acknowledged gold standard for *N*-glycan analysis involves High-Performance Liquid Chromatography-Hydrophilic Interaction Chromatography-Fluorescence Detection (HPLC-HILIC-FLD)(H. M. Kayili & Salih, 2021). In this method, liberated *N*- or *O*-glycans undergo prior labeling with a fluorophore tag before analysis. Numerous fluorophore tags have been documented in the literature, each chemically appended to the released glycans. Consequently, the signal corresponding to the glycans becomes detectable by the Fluorescence Detection (FLD) apparatus upon elution and subsequent arrival at the detector. This strategic integration of HPLC, HILIC, and FLD constitutes a robust approach for the sensitive and selective analysis of *N*-glycans, epitomizing a well-established methodology in the field(Reusch et al., 2015).

The examination of glycopeptides entails the application of a bottom-up proteomic approach, wherein glycoproteins undergo digestion utilizing a proteolytic enzyme, with trypsin being the most commonly employed enzyme for this purpose(Stavenhagen et al., 2018). Initial steps in bottom-up glycopeptide analysis involve the reduction of glycoproteins with detergents, followed by the alkylation of disulfide bridges. Subsequently, glycoproteins

undergo enzymatic proteolysis, with the quantity of enzyme utilized being contingent upon the protein amount. The incubation time for this process spans from 4 hours to overnight(Pan, Chen, Aebersold, & Brentnall, 2011).

The optimal analytical methodology for glycopeptide analysis is LC-MS/MS, leveraging reverse-phased separation techniques that exploit the peptide components within glycopeptides(Bagdonaite et al., 2022). Unlike glycans, glycopeptides can be effectively separated using reverse-phased approaches due to their inclusion of peptide segments. Single glycoprotein analysis obviates the need for enrichment methods in glycopeptide analysis, while complex samples necessitate enrichment strategies to enhance the identification of glycopeptides. Various software tools are employed to validate and confirm glycopeptide structures in the course of analysis(Ye & Vakhrushev, 2021).

Purification of Glycans via Hydrophilic Interaction Approaches

The HPLC-HILIC-FLD method is widely employed in the analysis of labeled glycans due to its superior efficacy in quantitative glycomics. Upon the release of *N*- or *O*-glycans from glycoproteins, regardless of the chosen measurement approach, purification becomes imperative. During the labeling process, samples are laden with detergents, salts, organic solvents, and various chemicals, all of which can adversely impact glycan analysis efficiency(Yang & Zhang, 2012). Therefore, a prerequisite for HPLC-HILIC-FLD analysis involves the removal of these contaminants to ensure the detectability of the glycans' signal and to maintain the integrity of the chosen stationary phase.

Hydrophilic interaction stands out as the most reliable purification approach for glycans when compared to alternative methods. Some methodologies, such as metal-affinity-based systems, specifically target sialic acid-containing glycans. However, specific reports suggest that this interaction may inadvertently encompass neutral glycans as well, potentially skewing results due to a higher affinity for sialic acids(Chen et al., 2014). Given the notably elevated abundance of sialic acid glycans compared to other glycans, such potential bias can introduce inaccuracies in the assessment of glycan abundances. This underscores the critical importance of an optimal purification strategy to ensure the fidelity of glycan analyses.

Numerous hydrophilic materials have been reported in the literature, but a considerable portion of them involve intricate synthesis methods, posing challenges for adaptation in diverse laboratory settings(Qing et al., 2020). Conversely, commercially available materials find widespread use and are commonly applied for purification purposes. Among these, crystalline cellulose stands out as the most prevalent, offering a naturally hydrophilic surface(Ohta, Kameda, Matsumoto, & Kawasaki, 2017). Notably, cellulose can be directly employed for glycan purification without necessitating chemical modification. This material exhibits relative stability and compatibility with a broad array of solid-phase extraction cartridges. The optimal strategy involves packing filter plates and solid-phase extraction cartridges with crystalline cellulose for the purification step, rendering this approach cost-effective and easily implementable. Apart from cellulose, sepharose presents itself as a superb alternative for the purification of labeled glycans after the labeling process(H Mehmet Kayili et al., 2022). However, it is essential to note that a drawback associated with sepharose is its considerably higher cost compared to cellulose.

Moreover, the utilization of a natural product, cotton, proves to be an economical option for glycans' purification(Selman, Hemayatkar, Deelder, & Wuhrer, 2011). This method is more cost-effective than any commercially available material documented in the literature. Additionally, cotton can be conveniently packed into pipette tips, facilitating the purification of even small quantities of glycans within a sample(H. M. Kayili & Salih, 2022). However, it is essential to acknowledge that this approach is not suitable for packing cotton into solid-phase extraction (SPE) cartridges and filter plates. The primary limitation of this method lies in the challenges associated with adopting sample preparation techniques, making it difficult to purify a high number of samples using this approach efficiently.

Enrichment of Glycopeptides via Hydrophilic Interaction Approaches

The predominant method employed for glycopeptide analysis is nano flow-LC-RP-ESI-MS/MS, owing to its capability to deliver heightened sensitivity, accuracy, and speed. This system's tandem MS/MS capabilities are mainly instrumental in enabling the identification of glycopeptides. Furthermore, this approach facilitates quantitative glycopeptide analysis. For

glycopeptides originating from individual proteins, direct analysis without an enrichment step is feasible using this method. However, when dealing with intricate samples like human plasma, the enrichment of glycopeptides becomes imperative(Ongay et al., 2012). This phenomenon arises from the suppressive effects of regular peptides on the signals emanating from glycopeptides.

Similar to glycan analysis, numerous hydrophilic materials have been introduced in the literature for the enrichment of glycopeptides(Chen et al., 2014). However, the synthesis procedures involved demand additional effort, rendering the adaptation of these methods intricate for laboratories. Opting for commercially available materials stands out as the most viable choice for a comprehensive glycopeptide analysis. Although the availability of commercial materials is limited, those utilized for glycans' purification are also employed for glycopeptide enrichment due to the hydrophilic nature of glycopeptides. Notably, crystalline cellulose and sepharose serve as viable options for glycopeptide enrichment, with no literature highlighting discernible differences in their enrichment performance. Alternatively, cotton emerges as another optimal choice for glycopeptide enrichment, proving to be highly effective in this regard(Han et al., 2020; Selman et al., 2011).

A recently introduced commercially available alternative material known as ZIC-HILIC demonstrates notable efficacy in the enrichment of glycopeptides(Di Palma, Boersema, Heck, & Mohammed, 2011). The typical ZIC-HILIC material comprises zwitterionic sulfobetaine functional groups, with the sulfonic group positioned distally to afford hydrophilic interactions on its surface. Extensive investigations have established the robust adsorption capacity of ZIC-HILIC materials towards glycopeptides.

Conclusion

Hydrophilic interaction has garnered recognition as the optimal approach for the purification and enrichment of glycans and glycopeptides, owing to its multifaceted advantages. Notably, it exhibits a commendably high adsorption capacity for glycoconjugates. Furthermore, the solvents employed in hydrophilic interaction are amenable to mass spectrometry, enhancing compatibility and facilitating downstream analyses. Despite the acknowledged efficacy of this

method, the availability of commercially viable HILIC materials remains constrained. However, there exists potential for utilizing cost-effective alternative materials in the pursuit of purification and enrichment applications, thereby addressing the current limitations associated with commercially available options.

REFERENCES

Ahn, J., Bones, J., Yu, Y. Q., Rudd, P. M., & Gilar, M. (2010). Separation of 2-aminobenzamide labeled glycans using hydrophilic interaction chromatography columns packed with 1.7 μm sorbent. *Journal of Chromatography B-Analytical Technologies in the Biomedical and Life Sciences, 878*(3-4), 403-408. doi:10.1016/j.jchromb.2009.12.013

Bagdonaite, I., Malaker, S. A., Polasky, D. A., Riley, N. M., Schjoldager, K., Vakhrushev, S. Y., Scott, N. E. (2022). Glycoproteomics. *Nature Reviews Methods Primers, 2*(1), 48. doi:10.1038/s43586-022-00128-4

Boersema, P. J., Mohammed, S., & Heck, A. J. R. (2008). Hydrophilic interaction liquid chromatography (HILIC) in proteomics. *Analytical and Bioanalytical Chemistry, 391*(1), 151-159. doi:10.1007/s00216-008-1865-7

Chen, C. C., Su, W. C., Huang, B. Y., Chen, Y. J., Tai, H. C., & Obena, R. P. (2014). Interaction modes and approaches to glycopeptide and glycoprotein enrichment. *Analyst, 139*(4), 688-704. doi:10.1039/c3an01813j

Di Palma, S., Boersema, P. J., Heck, A. J. R., & Mohammed, S. (2011). Zwitterionic Hydrophilic Interaction Liquid Chromatography (ZIC-HILIC and ZIC-cHILIC) Provide High Resolution Separation and Increase Sensitivity in Proteome Analysis. *Anal Chem, 83*(9), 3440-3447. doi:10.1021/ac103312e

Domínguez-Vega, E., Tengattini, S., Peintner, C., van Angeren, J., Temporini, C., Haselberg, R., Somsen, G. W. (2018). High-resolution glycoform profiling of intact therapeutic proteins by hydrophilic interaction chromatography-mass spectrometry. *Talanta, 184*, 375-381. doi:10.1016/j.talanta.2018.03.015

Gilar, M., Yu, Y. Q., Ahn, J., Xie, H. W., Han, H. H., Ying, W. T., & Qian, X. H. (2011). Characterization of glycoprotein digests with hydrophilic interaction chromatography and mass spectrometry. *Anal Biochem, 417*(1), 80-88. doi:10.1016/j.ab.2011.05.028

Guo, L. L., Nayak, S., Mao, Y., & Li, N. (2021). Glycine additive enhances sensitivity for N- and O-glycan analysis with hydrophilic interaction

chromatography-electrospray ionization-mass spectrometry. *Anal Biochem, 635*. doi:10.1016/j.ab.2021.114447

Halim, A., Ruetschi, U., Larson, G., & Nilsson, J. (2013). LC-MS/MS characterization of O-glycosylation sites and glycan structures of human cerebrospinal fluid glycoproteins. *J Proteome Res, 12*(2), 573-584. doi:10.1021/pr300963h

Han, J. L., Chen, Q. H., Zou, M. Y., Lu, Y., Wei, M., Li, C., Wang, Z. F. (2020). Separation and Purification of Sialylglycopeptide from Egg Yolk Based on Cotton Hydrophilic Chromatography. *Chinese Journal of Analytical Chemistry, 48*(1), 34-39. doi:10.19756/j.issn.0253-3820.191317

Holst, S., Wuhrer, M., & Rombouts, Y. (2015). Glycosylation Characteristics of Colorectal Cancer. In R. R. Drake & L. E. Ball (Eds.), *Glycosylation and Cancer* (Vol. 126, pp. 203-256).

Kayili, H. M., Atakay, M., Hayatu, A., & Salih, B. (2022). Sample Preparation Methods for N-glycomics. *Advances in Sample Preparation*, 100042.

Kayili, H. M., Ertürk, A. S., Elmaci, G., & Salih, B. (2019). Poly(amidoamine) dendrimer-coated magnetic nanoparticles for the fast purification and selective enrichment of glycopeptides and glycans. *Journal of Separation Science, 42*(20), 3209-3216. doi:10.1002/jssc.201900492

Kayili, H. M., Sakhta, R., & Salih, B. (2022). Comparison of denaturing agent effects in enzymatic N-glycan release for human plasma N-glycan analysis. *Turkish Journal of Chemistry, 46*(5), 1524-+. doi:10.55730/1300-0527.3457

Kayili, H. M., & Salih, B. (2021). N-glycan Profiling of Glycoproteins by Hydrophilic Interaction Liquid Chromatography with Fluorescence and Mass Spectrometric Detection. *Jove-Journal of Visualized Experiments*(175). doi:10.3791/62751

Kayili, H. M., & Salih, B. (2022). Site-specific N-glycosylation analysis of human thyroid thyroglobulin by mass spectrometry-based Glyco-analytical strategies. *J Proteomics, 267*. doi:10.1016/j.jprot.2022.104700

Kozak, R. P., Urbanowicz, P. A., Punyadeera, C., Reiding, K. R., Jansen, B. C., Royle, L., Wuhrer, M. (2016). Variation of Human Salivary O-Glycome. *PLoS ONE, 11*(9), e0162824. doi:10.1371/journal.pone.0162824

Kozlik, P., Goldman, R., & Sanda, M. (2018). Hydrophilic interaction liquid chromatography in the separation of glycopeptides and their isomers.

Analytical and Bioanalytical Chemistry, 410(20), 5001-5008. doi:10.1007/s00216-018-1150-3

Krištić, J., Vučković, F., Menni, C., Klarić, L., Keser, T., Beceheli, I., Lauc, G. (2014). Glycans are a novel biomarker of chronological and biological ages. *J Gerontol A Biol Sci Med Sci, 69*(7), 779-789. doi:10.1093/gerona/glt190

Liu, Z. L., Xu, M. M., Zhang, W. Q., Miao, X. Y., Wang, P. G., Li, S. W., & Yang, S. (2022). Recent development in hydrophilic interaction liquid chromatography stationary materials for glycopeptide analysis. *Analytical Methods, 14*(44), 4437-4448. doi:10.1039/d2ay01369j

Melmer, M., Stangler, T., Premstaller, A., & Lindner, W. (2011). Comparison of hydrophilic-interaction, reversed-phase and porous graphitic carbon chromatography for glycan analysis. *Journal of Chromatography A, 1218*(1), 118-123. doi:10.1016/j.chroma.2010.10.122

Ohta, Y., Kameda, K., Matsumoto, M., & Kawasaki, N. (2017). Rapid Glycopeptide Enrichment Using Cellulose Hydrophilic Interaction/Reversed-Phase StageTips. *Mass Spectrom (Tokyo), 6*(1), A0061. doi:10.5702/massspectrometry.A0061

Ongay, S., Boichenko, A., Govorukhina, N., & Bischoff, R. (2012). Glycopeptide enrichment and separation for protein glycosylation analysis. *Journal of Separation Science, 35*(18), 2341-2372. doi:10.1002/jssc.201200434

Pan, S., Chen, R., Aebersold, R., & Brentnall, T. A. (2011). Mass Spectrometry Based Glycoproteomics—From a Proteomics Perspective. *Molecular & Cellular Proteomics : MCP, 10*(1), R110.003251. doi:10.1074/mcp.R110.003251

Pinho, S. S., & Reis, C. A. (2015). Glycosylation in cancer: mechanisms and clinical implications. *Nature Reviews Cancer, 15*(9), 540-555. doi:10.1038/nrc3982

Qing, G. Y., Yan, J. Y., He, X. N., Li, X. L., & Liang, X. M. (2020). Recent advances in hydrophilic interaction liquid interaction chromatography materials for glycopeptide enrichment and glycan separation. *Trac-Trends in Analytical Chemistry, 124*. doi:10.1016/j.trac.2019.06.020

Reusch, D., Haberger, M., Maier, B., Maier, M., Kloseck, R., Zimmermann, B., Wuhrer, M. (2015). Comparison of methods for the analysis of

therapeutic immunoglobulin G Fc-glycosylation profiles--part 1: separation-based methods. *MAbs, 7*(1), 167-179. doi:10.4161/19420862.2014.986000

Selman, M. H., Hemayatkar, M., Deelder, A. M., & Wuhrer, M. (2011). Cotton HILIC SPE microtips for microscale purification and enrichment of glycans and glycopeptides. *Anal Chem, 83*(7), 2492-2499. doi:10.1021/ac1027116

Stavenhagen, K., Kayili, H. M., Holst, S., Koeleman, C. A. M., Engel, R., Wouters, D., Wuhrer, M. (2016). In-depth site-specific N- and O-Glycosylation analysis of human C1-Inhibitor reveals extensive mucin-type O-glycosylation. *Glycobiology, 26*(12), 1474-1475.

Stavenhagen, K., Kayili, H. M., Holst, S., Koeleman, C. A. M., Engel, R., Wouters, D., Wuhrer, M. (2018). N- and O-glycosylation Analysis of Human C1-inhibitor Reveals Extensive Mucin-type O-Glycosylation. *Molecular & Cellular Proteomics, 17*(6), 1225-1238. doi:10.1074/mcp.RA117.000240

Stowell, S. R., Ju, T. Z., & Cummings, R. D. (2015). Protein Glycosylation in Cancer. In A. K. Abbas, S. J. Galli, & P. M. Howley (Eds.), *Annual Review of Pathology: Mechanisms of Disease, Vol 10* (Vol. 10, pp. 473-510).

Tian, Y., & Zhang, H. (2010). Glycoproteomics and clinical applications. *Proteomics Clinical Applications, 4*(2), 124-132. doi:10.1002/prca.200900161

Yang, S., & Zhang, H. (2012). Solid-phase glycan isolation for glycomics analysis. *Proteomics Clin Appl, 6*(11-12), 596-608. doi:10.1002/prca.201200045

Ye, Z., & Vakhrushev, S. Y. (2021). The Role of Data-Independent Acquisition for Glycoproteomics. *Molecular & Cellular Proteomics, 20*, 100042. doi:https://doi.org/10.1074/mcp.R120.002204

Zauner, G., Deelder, A. M., & Wuhrer, M. (2011). Recent advances in hydrophilic interaction liquid chromatography (HILIC) for structural glycomics. *Electrophoresis, 32*(24), 3456-3466. doi:10.1002/elps.201100247

CHAPTER 5

LITHIUM ION BATTERY AND BATTERY TECHNOLOGIES

Prof. Dr. Murat ATES[1]

DOI: https://dx.doi.org/10.5281/zenodo.10444719

[1] Tekirdag Namık Kemal University, Faculty of Arts and Sciences, Department of Chemistry, Tekirdag, TÜRKİYE. mates@nku.edu.tr, Orcid ID: 0000-0002-1806-0330

INTRODUCTION

Nowdays, lithium-ion batteries (LIB) or second (recheargeable) batteries have the highest energy density in market. LIBs are the most used recheargeable batteries since their commercialization in the 90s (Alvira et al., 2022). They can be used in many different types of electric devices, such as mobile phones, digital cameras, laptop computers, etc. (Ma et al., 2012). Lithium-ion is used as high theoretical capacity of 3860 mAh/g and lowest electrochemical potential (-3.04 V vs. standard hydrogen electrode) (Hong et al., 2012). Due to the needs of alternative and advanced energy storage systems, lithium-ion, lithium sulfur, lithium iron phosphate ($LiFePO_4$) batteries, etc. has been used in many different devices in the world (Wang et al., 2019; Zhu et al., 2018). Innovative electrode active material design is to key to present the various advancements in recheargeable LIBs (Kang et al., 2006). LIBs are mostly used energy storage devices because of the higher energy density (150-200 Wh/kg) compared to other systems. LIBs have large reversibility and durability (Fan et al., 2018). However, they have a few disadvantageous, such as a limited power density (<1000 W/kg) and low stability performance (<1000 cycles) (Zhang et al., 2013). There is a large specific volume expansion, which cause the disordering structure of electrode. Therefore, this process causes the rapid capacity fading of battery (Liu et al., 2014).

Lithium based batteries and battery technologies are very popular in the world. There are many different types of lithium batteries. For example, lithium-titanium oxide ($Li_4Ti_5O_{12}$, LTO) including spinel form has long stability due to limited volume change (Panero et al., 2001). It has a high specific capacity of 175 mAh/g during 1.00-3.00 V (vs. Li+/Li^o).

$$Li_4Ti_5O_{12} + 3Li^+ + 3e^- \rightarrow Li_7Ti_5O_{12} \quad (1)$$

The above reaction occurs during the potential range of 1.00-3.00 V. However, its capacity increases to 293 mAh/g while expanding potential range from 0.01 V to 3.00 V (vs. Li^+/Li^o). It is related to full reduction of titanium ions from +4 to +3 oxidation state. It supplies additional two Li^+ ions (Ge at al., 2009).

$$Li_7Ti_5O_{12} + 2Li^+ 2e^- \rightarrow Li_9Ti_5O_{12} \quad (2)$$

LTO type of batteries are used as a next generations of Li-ion batteries. It is only limited applications of their low electric conductivity (Yi et al., 2015). In

literature, it has modified with Ag nanoparticles (Krajewski et al., 2016). Addition of Ag nanoparticles affect the electrochemical properties of LTO batteries, such as reaction kinetics, and cyclability.

Second kind type electrodes, such as $Cd/Cd(OH)_2/OH^-$, $Pb/PbSO_4/SO_4^{-2}$, $Hg/HgO/OH^-$, $Ag/Ag_2O/OH^-$, etc. were used in practical LIBs due to soluble metal ions (Vetter, 1967). The main aim is to supply a depositing an inactive surface film on Li electrode to protect the reaction with Li^+ ion.

Using appropriate conductive substrates or channels for electron movements are very crucial for enhancing of LIBs performance. So, many conductive materials, such as graphene or GO were used to be an ideal substrate for LIBs because of their high electronic conductivity, chemical stability and high surface area (Lan et al., 2014; Mo et al., 2014; Li et al., 2013).

1. Electrode active materials in anode side

Graphite was mostly used in anode side of Li-ion batteries because of its availability, low-cost and durability (Shafiei et al., 2011). In graphite including in anode side, Li^+ insertion mechanism supply a reversible process, progressive intercalation of Li^+ ions between graphene layers to obtain a theoretical capacity of 372 mAh/g. An average value was taken as 350 mAh/g (Kasavajjula et al., 2007).

Graphene was also used in LIBs, which has two-dimensional layers of sp^2 hybridized carbon atoms arranged in six-membered rings. It has also extra electronic transport properties (Stankovich et al., 2006; Novoselov et al., 2005).

Muti-walled carbon nanotube (MWCNT) was used in composite anode materials due to their large internal cavity, large surface area, material flaxibility, and high electrical conductivity (Wang et al., 2009; Du et al., 2010). In literature, Sn-Cu / MWCNT composite electrodes were used in different amounts of MWCNTs (10 wt%, 20 wt%, 40 wt%) by high energy mechanical milling method (Uysal et al., 2014). It concludes the amounts of MWCNTs improve Sn-Cu / MWCNT composite anodes for cyclability and reversible capacity.

Co_3O_4 / graphene composites (CGC) were presented as anode materials in LIBs. In this study, Co_3O_4 nanoparticles in the range of 10-30 nm were homogeneously dispersed on graphene nanosheets. Graphene nanosheets supply an extra electrical conductivity of composite material. It was given a

good cyclic performance of 740 mAh/g after 60 cycles, 88.3% of the theoretical value of CGC (Cao et al., 2011).

Zinc oxide (ZnO) was used as an anode side in LIBs due to its high theoretical capacity (978 mAh/g) (Huang et al., 2011). Li metals and metal oxides such as Sn, Sb, TiO_2, and SO_2 easily help to develop cracks during charge / discharge process. As an alternative way, addition of MWCNT prevents the agglomeration and enhance the electronic conductivity of electrode materials. As a result, it enhances the stability performance of LIBs (Zhai et al., 2011).

The mechanism of SnO_2 and Li can be given in literature according to the following two steps (Alaf et al., 2013).

$$SnO_2 + 4Li^+ + 4e^- \rightarrow Sn + 2Li_2O \quad (3)$$

$$Li^+ + xe^- + Sn \leftrightarrow Li_4Sn \quad (0 \leq x \leq 4.4) \quad (4)$$

Sn / SnO_2 / MWCNT nanocomposite anode paper was synthesized by thermal evaporation and subsequent plasma oxidation techniques.

Silicon was used as a negative electrode material for LIBs due to its high theoretical specific capacity of 4200 mAh/g, low lithiation voltage characteristics and natural abundance (Tocoglu et al., 2020).

Cu_2O / reoxidized CuO (R-CuO) can be used for energy storage materials. It was obtained a specific capacity of 312.9 mAh/g at 100 mA/g after 200 cycles for LIBs (Zhao et al., 2021). In addition, the R-CuO was given as a pseudo supercapacitors and presented a specific capacity of 493 F/g at 5 A/g in a three-electrode cell. Cu oxides (Cu_2O and CuO) have been widely applied for photocatalyst, supercapacitors and protective coatings due to their proper band gaps for absorbing visible light and antibacterial properties. The Li and Na storage performances were used as Cu_2O derived CuO (R-CuO) materials.

PANI/amorphous TiO_2/GO nanocomposite was used as anode material for LIBs (Ye at al., 2015). A first discharge capacity was measured as 1335 mAh/g at 50 mA/g and a reversible capacity of 435 mAh/g after 250 cycles at 100 mA/g. Nickel-titanate / GO composite was presented as negative electrode for LIBs and SIBs. They were given as a high discharge capacities of 877 and 790 mAh/g against lithium and sodium metals (Majumder et al., 2021).

2. Electrode active materials in cathode side

LIBs have mostly been sold in daily life for electronic evaluations. LIBs consisting of $LiCoO_2$ and graphite were selected as electroactive materials with a critical limit in energy density (Ohzuku et al., 2007).

Guo et al. have suggested flexible and high electrical conductive Sn-Ni/C electrode, which improve the stability and rate performances of electrodes (Guo et al., 2007). Moreover, Zhao et al. have given a Sn-Co-C electrode for anode compartment, which was synthesized by carbothermal reduction method (He et al., 2010). It enhances the stability of device.

Lithium ion cathode material including AC/Li_3N shows a high capacitive protection of 91% after 10.000 cycles (E= 74.7 Wh/kg and P= 12.9 kW/kg) (Sun et al., 2020). Poly(3,4-ethlenedioxythiophene) (PEDOT) can be used in combination with other inorganic cathode materials and to coat Al current collector (Rehmen et al., 2020). In literature, there is a report to prevent the low electrical conductivity and volume expansion hinder for Fe_3O_4 nanoparticles (Han et al., 2018; Su et al., 2019).

CONCLUSION

In this study, lithium ion battery and battery technologies were investigated for designing of electroactive materials. Electroactive materials in electrodes were given according to literature. Electroactive material type together with Li ion critically affects the electrochemical performance of LIBs.

In summary, there are many different types of anode and cathode materials with a high rate performance and stability for LIBs applications. This chapter investigates the basis for further explanations of highly efficient electroactive materials in LIBs.

REFERENCES

Alaf, M., Gultekin, D., Akbulut, H. (2013). “Electrochemical properties of free-standing Sn/SnO_2/multi-walled carbon nanotube anode papers for Li-ion batteries”, Appl. Surf. Sci., 275, 244-251.

Alvira, D., Antoran, D., Manya, J.J. (2022). “Plant derived hard carbon as anode for sodium ion batteries: A comprehensive review to guide interdisciplinary research”, Chem. Eng. J., 447, Article number: 137468.

Du, G., Zhong, C., Zhang, P., Guo, Z., Chen, Z., Liu, H. (2010) “Tin dioxide / carbon nanotube composites with high uniform SnO_2 loading as anode material for lithium ion batteries”, Electrochim. Acta, 55, 2582-2586.

Fan, X., Yue, J., Han, F., Chen, J., Deng, T., Zhu, X., Hou, S., Wang, C. (2018). “High performance all solid-state Na-S battery enabled by casting annealing technology”, ACS Nano, 12, 3360-3368.

Ge, H., Li, N., Li, D., Dai, C., Wang, D. (2009). “Studying on the theoretical capacity of spinel titanium titanate induced by low potential intercalation”, J. Phys. Chem. C., 113, 6324-6326.

Guo, H., Zhao, H., Jia, X. (2007). “Spherical Sn-Ni-C alloy anode material with sub-micro/micro complex particle structure for lithium secondary batteries”, Electrochem. Commun. 9, 2207-2211.

Han, D., Guo, G., Yan, Y., Li, T., Wang, B., Dong, A. (2018). "Pomegranate like carbon coated-Fe3O4 nanoparticle supercapacitors for high-performance lithium storage", Energy Storage Mater., 10, 32-39.

He, J., Zhao, H., Wang, M., Jia, X. (2010). “Preparation and characterization of Co-Sn-C anodes for lithium ion batteries”, Mater. Sci. Eng. B., 171, 35-39.

Hong, C., Noviyanto, A., Ryu, J.H., Kim, J., Yoon, D. (2012). “Effects of the starting materials and mechanochemical activation on the properties of solid state reacted $Li_4Ti_5O_{12}$ for lithium ion batteries”, Ceram. Int., 38(1), 301-310.

Huang, X.H., Xia, X.H., Yuan, Y.F., Zhou, F. (2011) “Porous ZnO nanosheets grown on copper substrates as anode for lithium ion batteries”, Electrochim. Acta, 56(14), 4960-4965.

Kang, K.S., Meng, Y.S., Breger, J., Grey, C.P., Ceder, G. (2006). "Electrodes with high power and high capacity for rechargeable lithium batteries", Science, 311, 977-980.

Kasavajjula, U., Wang, C., Applebyb, A.J. (2007). "Nano- and bulk silicon-based insertion anodes for lithium ion secondary cells ", J. Power Sources, 163, 1003-1039.

Krajewski, M., Hamankiewicz, B., Czerwinski, A. (2016). "Voltammetric and impedance characterization of $Li_4Ti_5O_{12}$/n-Ag composite for lithium ion batteries", Electrochim. Acta, 219, 277-283.

Lan, T.B., Liu, Y.B., Dou, J., Hong, Z.S., Wei, M.D. (2014). "Hierarchically porous TiO_2 microspheres as a high performance anode for lithium-ion batteries", J. Mater. Chem. A., 2, 1102-1106.

Li, W., Wang, F., Feng, S.S., Wang, J.X., Sun, Z.K., Li, B., Li, Y.H., Yang, J.P., Elzatahry, A.A., Xia, Y.Y., Zhao, D.Y. (2013). "Sol-gel design strategy for ultradispersed TiO_2 nanoparticles on graphene for high-performance lithium ion batteries", 135, 18300-18303.

Li, B., Cao, H., Shao, J., Li, G., Qu, M., Yin, G. (2011). "Co_3O_4@graphene composites as anode materials for high-performance lithium-ion batteries", Inorg. Chem., 50, 1628-1632.

Liu, C., Huang, H., Cao, G., Xue, F., Camacho, R.A.P., Dong, X. (2014). "Enhanced electrochemical stability of Sn-carbon nanotube nanocomposites as lithium-ion battery anode", Electrochim. Acta, 144, 376-382.

Ma, R.G., Luo, Z.G., Yang, S.L., Xi, L.J., Wang, C.D., Wang, H.E., Chung, C.Y. (2012). "Facile synthesis and electrochemical characterizations of Sn_4Ni_3/C nanocomposites as anode materials for lithium ion batteries", J. Solid State Chem., 196, 536-542.

Majumder, T., Das, D., Majumder, S.B. (2021). "Nickel titanate-GO composite as negative electrode for lithium and sodium ion batteries", Materials Letters, 301, Article number: 130293.

Mo, R.W., Lei, Z.Y., Sun, K.N., Rooney, D. (2014). "Facile synthesis of anatase TiO_2 quantum-dot / graphene nanosheet composites with enhanced electrochemical performance for lithium-ion batteries", Adv. Mater., 26, 2084-2088.

Novoselov, K.S., Geim, A.K., Morozov, S.V., Jiang, D., Katsnelson, M.I., Grigorieva, I.V., Dubonos, S.V. (2005). "Two-dimensional gas of massless dirac fermions in graphene", Nature, 438 (7065), 197-200.

Ohzuku, T., Brodd, R.J. (2007). "An overview of positive-electrode materials for advanced lithium-ion batteries", J. Power Sources, 174, 449-456.

Panero, S., Reale, P., Ronci, F., Scrosati, B., Perfetti, P., Albertini, V.R. (2001) "Refined, in-situ EDXD structural analysis of the $Li[Li_{1/3}Ti_{5/3}]O_4$ electrode under lithium insertion-extraction", Phys. Chem. Chem. Phys., 3, 845-847.

Rehmen, J., Pathirana, T., Garcia-Quintana, L., Kerr, R., Howlett, P.C., Zuber, K., Pozo-Gonzalo, C., Evans, D.R. (2020). "Structuring PEDOT hollow nanosphere electrodes for high specific energy Li-metal / polymer thin-film batteries", ACS Appl. Nano Mater., 3, 3820-3828.

Shafiei, M., Alpas, A.T., Edited by Harris, S.J., Qi, Y., Jiang, M. (2011). "A transmission electron microscopy study of degradation mechanism in a tin-carbon fibre composite anode for rechargeable lithium-ion batteries", ECS Transactions, 35(14), 7-17.

Stankovich, S., Dikin, D.A., Dommett, G.H.B., Kohlhaas, K.M., Zimney, E.J., Stach, E.A., Piner, R.D., Nguyen, S.T., Ruoff, R.S. (2006). "Graphene-based composite materials", Nature, 442 (7100), 282-286.

Su, Y., Wang, F., Zhang, J., Tong, R.A., Chong, S., Wang, W.A., Wang, C.A., Chen, C. (2019). "A monocrystal Fe_3O_4@ultrathin *N*-doped carbon core / shell structure from magnetotactic bacteria to Li storage", J. Mater. Chem., 7, 20899-20904.

Sun, C.K., Zhang, X., Li, C., Wang, K., Sun, X.Z., Ma, Y.W. (2020). "High-efficiency sacrificial prelithiation of lithium-ion capacitors with superior energy storage performance", Energy Storage Materials, 24, 160-166.

Toçoglu, U., Alaf, M., Akbulut, H. (2020). "Towards high cycle stability yolk-shell structured silicon/rGO/MWCNT hybrid composites for Li-ion battery negative electrode", Mater. Chem. Phys., 240, Article number: 122160.

Wang, P., Zhou, H., Meng, C., Wang, Z., Akhtar, K., Yuan, A. (2019). "Cyanometallic framework-derived hierarchical Co_3O_4-NiO /graphene foam as high-performance hinder-free Wang, Y., Wu, M., Jiao, Z., Lee,

J.Y. (2009). “Sn@CNT and Sn@c@CNT nanostructures for superior reversible lithium ion storage”, Chem. Mater., 21(14), 3210-3215.

electrodes for supercapacitors”, Chem. Eng. J., 369, 57-63.

Uysal, M., Cetinkaya, T., Kartal, M., Alp, A., Akbulut, H. (2014). “Production of Sn-Cu / MWCNT composite electrodes for Li-ion batteries by using electroless tin coating”, Thin Solid Films, 572, 216-223.

Vetter, K.J., Electrode Kinetics, Academic Press, NY, 1967.

Yi, T.F., Yang, S.Y., Xie, Y. (2015). “Recent advances of $Li_4Ti_5O_{12}$ as a promising next generation anode material for high power lithium-ion batteries”, J. Mater. Chem. A., 3, 5750-5777.

Ye, Y., Wang, P., Sun, H., Tian, Z., Liu, J., Liang, C. (2015). “Structural and electrochemical evaluation of a TiO_2-graphene oxide based sandwich structure for lithium-ion battery anodes”, RSC Adv., 5, 45038-45043.

Zhang, F., Zhang, T., Yang, X., Zhang, L., Leng, K., Huang, Y., Chen, Y. (2013). “A high performance supercapacitor-battery hybrid energy storage device based on graphene-enhanced electrode materials with ultrahigh energy density”, Energy Environmental Science, 6(5), 1623-1632.

Zhai, C.X., Du, N., Zhang, H., Yu, J.X., Wu, P., Xiao, C.M., Yang, D.R. (2011). “Assembling $CoSn_3$ nanoparticles on multiwalled carbon nanotubes with enhanced lithium storage properties”, Nanoscale, 3(4), 1798-1801.

Zhao, H., Zhao, Z., Qu, J., Chen, X., Zhou, F., Xie, H., Wang, D., Yin, H. (2021). “A combined oxidation and salt-thermal approach to converting copper scraps to copper oxides as energy storage materials”, Journal of Cleaner Production, 320, Article number: 128870.

Zhu, M., Zhou, H., Shao, J., Feng, J., Yuan, A. (2018). “Prussian blue nanotubes supported or graphene foam as superior binder-free anode of lithium-ion batteries”, J. Alloys Compd., 749, 811-817.

CHAPTER 6

SUPERCAPACITORS AND APPLICATIONS

Prof. Dr. Murat ATES[1]

DOI: https://dx.doi.org/10.5281/zenodo.10444727

[1] Tekirdag Namık Kemal University, Faculty of Arts and Sciences, Department of Chemistry, Tekirdag, TÜRKİYE. mates@nku.edu.tr, Orcid ID: 0000-0002-1806-0330

INTRODUCTION

Electrochemical energy storage systems were named as batteries, fuel cells and supercapacitors. They include the principle of chemical process to electrical energy conversion (Rajkumar et.al., 2015). Supercapacitors have advantageous compared to other energy storage systems because of their fast charge/discharge capability, long stability, low-cost and eco-friendly (Kumar et al., 2014; Zhang et al., 2017; Wen et al., 2017). They can be used many applications, such as hybrid electronic cars, portable electronics, digital camare, etc. (Zhang et al., 2009; Singu et al., 2016). Lithium (Li) half cell including copper nanopillar based current collector shows a high capacity of 880 mAh/kg at 0.2 C, good rate capability and high durability (97% after 1000 cycles). This supercapacitor supply a high energy density of 98.9 Wh/kg at 248 W/kg, high power density of 7018 W/kg and long stability (>1000 cycles). Large porous materials have ion buffer devices to store ions, which may quickly transfer electrolyte ions into these porous (Qin et al., 2018; Sun et al., 2020). Supercapacitors (SCs) are limited specific energy (~5-10 Wh/kg) for EDLC system (Su et al., 2020; Shao et al., 2018). In addition, self-discharge and high-low temperature properties are very critical issue for supercapacitors. To solve these problems a few theoretical studies were given in literature (Kong et al., 2015).

1. Mechanisms of supercapacitors

There are three sections to categorize the energy storage mechansism of supercapacitors. These are electrical double layer capacitor (EDLC), pseudocapacitor (Mohammadi et al., 2018) and hybrid supercapacitors.

EDLC system includes carbon based electrode materials, which store charges via accumulation at the Helmoltz plane (Ning et al., 2016). EDLC system includes carbanous materials and their hybrids, such as graphene, carbon fiber, carbon nanotubes, etc. (Liu et al., 2014). To prevent the agglomeration of graphene nanosheet, there is a practical approach to design the best chosen material on electrode surface (Li and Ostling, 2013). A nitrogen rich thin layer of amorphous carbon coated on graphene was synthesized to avoid restacking of graphene nanosheets. Therefore, the high electronegativity of nitrogen attracts the Li^+ ions and enhances the electrochemical performances of supercapacitors (Kashedikar and Maier, 2009). Among many different types

of nanomaterials, graphene and its derivatives are used ideal materials for supercapacitor applications due to their superior physicochemical properties, such as large surface area and wide potential window, etc. (Seyyidin et al., 2016). Carbon nanotubes (CNTs) are used in EDLC system due to their large surface area, high conductivity, and good stability performances. However, its specific capacitance was very low (<100 F/g) (Sun et al., 2012).

Pseudocapacitors have transition metal oxides and conducting polymers. They have mostly reversible redox reactions taking place on the surface or near the electrodes (Zhang et al., 2017). Pseudocapacitors store charges for a fast reversible Faradaic redox reactions on the electrode surface. It suppy a high specific capacitance due to asymmetric supercapacitor design (Wu et al., 2021). Metal oxides can mostly be chosen for electroactive materials than most conducting polymers due to their higher capacitance and electrochemical stability (Hulicova-Jurcakova et al., 2009). There are many different types of transition metal oxides, such as RuO_2, NiO, CuO, $NiMoO_4$, Co_3O_4, MnO_2, Mn_3O_4, Fe_2O_3, $NiCo_2O_4$, etc. (Hu et al., 2015; Vadiyar et al., 2015). One dimensional (1D) nanomaterials including metal oxides and carbanous materials have been used in energy storage devices (Xie et al., 2014). There are many conducting polymers used for supercapacitors. For example, polypyrrole (PPy) including nanospheres (Lee et al., 2017), nanosheets (Yang et al., 2016), nanorods / tubes / wires (Huang et al., 2017) have great surface areas and porosities. Therefore, it supplies shorten diffusion path for ions (Shown et al., 2015).

Hybrid supercapacitors have both EDLC and paseudocapacitor systems. It can be named as asymmetric supercapacitors (Wang et al., 2013). Hybrid supercapacitors are important next generation energy storage systems because of high energy, high power density and long stability (Lee et al., 2022). Mexene type of materials can be combined with conducting polymers to improve the electrical conductivity and cycling stability (Meng et al., 2017).

2. Symmetric Supercapacitor systems

A new synthesis of copper and nitrogen-doped graphene (NG) / carbon nanotube (CNT) with percentage of nitrogen (10.1%) has been given in literature (Faisal et al., 2021).The NG/CNT electrode shows a high specific capacitance of 1250 mAh/g at a constant current density of 0.1 A/g. It is 3.4.

times greater than graphite (372 mAh/g). In another study, a new type of polyaniline / graphene oxide / copper (Cu) composite was obtained by in-situ polymerization process (Ma et al., 2019). The PANI/rGO/Cu electrode has a high specific capacitance of C_{sp}= 557.92 F/g and good cycling stability.

The copper manganese oxide materials were obtained by co-precipitation method. It has was C_{sp}= 280 F/g at 1 A/g. CMO/MWCNT/PEDOT:PSS electrode shows a high specific capacitance of C_{sp}= 1087 F/g at 1 A/g with a good rate performance and good electrochemical stability of 104% capacitance retention and coulombic efficiency of 101% over 10.000 cycles at a current density of 5 A/g (Kiruthika et al., 2023).

Symmetric design of binder-free Ni_3S_2/MoS_2/rGO electrodes were synthesized on Ni-foam with a high specific capacity of 2580 F/g at 1 A/g and good cycling stability with 100% capacitance retention for 10.000 charge/discharge capability with specific capacitance of C_{sp}= 600 F/g at 20 A/g (Arun et al., 2023). MnO_2 decorated on electrospun carbon nanofiber / 5 wt % graphene composite electrode shows a high specific capacitance of C_{sp}= 210 F/g at 1 mA/cm^2, good rate capability of C_{sp}=170 F/g retained at a high current density of 20 mA/cm^2, high energy density of E= 24-19 Wh/kg and power density of P= 400 to 10.000 W/kg in 6 M KOH aqueous solution (Lee and Kim, 2016). In addition, Ag nanoparticles enable in avoiding agglomeration and supply a long cycle life (Atif and Inam, 2016).

3. Asymmetric supercapacitor systems

The ideal energy storage devices have both high energy and high power density. Moreover, SCs have high power density. However, they have limited energy density. Therefore, scientists have developed an asymmetric supercapacitors to enhance energy density (Chen et al., 2019; Simon et al., 2014). An asymmetric supercapacitor electrode design was given in literature (Ng et al., 2017). A nanoporous CuO electrode shows high specific capacitance of C_{sp}= 431 F/g at 3.5 mA/cm^2, good rate capability and stability of asymmetric electrode design for supercapacitors. CuO nanoporous has a positive electrode and activated carbon (AC) as negative electrode. They show a high energy density of E= 19.7 Wh/kg and power density of P= 7 kW/kg (Moosavifard et al., 2015).

Hybrid lithium-ion supercapattery (HLS) was combined with an insertion type anode (high capacity battery type) and porous cathode (high rate capacitive type) (Wang et al., 2019; Li et al., 2019). Co_3O_4 / graphene composite was presented as efficient electrode material for supercapacitor (Wang et al., 2017). It has a specific capacitance of C_{sp}= 392 F/g at 1 A/g, a relatively small internal resistance and diffusion resistance of 0.36 Ω and 0.45 Ω, respectively. In addition, microwave-irradiation method was used as GO based nanocomposites to reduce rGO using supercapacitors and battery studies (Zhu et al., 2015).

CONCLUSION

This review study will help to development of efficient and functional nanostructure and energy storage systems. Green energy storage devices, such as batteries and supercapacitors have been used due to their good stability, high rate capability, etc. (Li et al., 2016; Li et al., 2018). The electrode components should be taken as simple, cheap and eco-friendly.

In conclusion, hybrid electrode system has mostly higher electrochemical performances than EDLC and pseudocapacitance systems. Wearable electronic technologies are very popular. They can be used in many flexible and sensitive devices. In literature, a new synthesized crystal structure of the cumarin was given during PEDOT polymerization process. It has a long-discharge time of 2767 s at 5 mA/cm^2 similar to batteries. The lifetime of the supercapacitor with a long cycles, 15.000 times was obtained as 113.6%. Therefore, the use of material has been successfully made in wearable electronic sectors (Yazar et al., 2023).

REFERENCES

Atif, R., Inam, F. (2016). “Reasons and remedies for the agglomeration of multilayered graphene and carbon nanotubes in polymers”, Beilstein Jo Nanotechnol., 7, 1174-1196.

Arun, T., Aravininth, K., Bhargav, P.B., Francis, M.K. (2023). "Enhanced supercapacitor performance through surface modification: Binder-free electrode synthesis of Ni_3S_2/MoS_2/rGO on Ni-foam with superior cyclability", J. Energy Storage, 74, Article number: 109333.

Chen, S., Cheng, M., Long, Y., Tian, C. (2019). “Preparation and characterization of monodispersed spherical $Fe_2O_3@SiO_2$ reddish pigments with core-shell structure”, J. Adv. Ceramics, 8(1), 39-46.

Faisal, S.N., Subramaniyam, C.M., Islam, M.M., Chowdhury, A.I., Dous, S.X., Roy, A.K., Harris, A.T., Minett, A.I. (2021). “3D copper-confined *N*-doped graphene / carbon nanotubes networks as high performing lithium-ion battery anode”, J. Alloys Compds., 850, Article number: 156701.

Hu, X.W., Liu, S., Qu, B.T., You, Y.Z. (2015). “Starfish-shaped Co_3O_4 / $ZnFe_2O_4$ hollow nanocomposite synthesis, supercapacity, and magnetic properties”, ACS Appl. Mater. Interfaces, 7, 9972-9981.

Huang, S., Han, Y., Lyu, S., Lin, W., Chen, P., Fang, S. (2017). “A facile one-step approach for the fabrication of polypyrrole nanowire / carbon fiber hybrid electrodes for flexible high performance solid-state supercapacitors”, Nanotechnology, 28, Article number: 435204.

Hulicova-Jurcakova, D., Kodama, M., Shiraishi, S., Hatori, H., Zhu, Z.H., Lu, G.Q. (2009). “Nitrogen enriched nanoporous carbon electrodes with extraordinary supercapacitors”, Adv. Funct. Mater., 19, 1800-1809.

Kashedikar, N.A., Maier, J. (2009). “Lithium storage in carbon nanostructures”, Adv. Mater., 21, 2664-2680.

Kiruthika, K., Renuga, V., Suryanarayanan, V. (2023). "Fabrication and electrochemical performance of spinel copper manganese oxide nanocomposites for supercapacitor application", Bull. Mater., 46, Article number: 98.

Kong, X., Lu, D.N., Liu, Z., Wu, J.Z. (2015). "Molecular dynamics for the charging behavior of nano-structured electric double layer capacitors

containing room temperature ionic liquids", Nano Research, 8(3), 931-940.

Kumar, M., Subramania, A., Balakrishnan, K. (2014). “Preparation of electrospun Co_3O_4 nanofibers as electrode material for high performance asymmetric supercapacitors”, Electrochim. Acta, 149, 152-158.

Li, J., Ostling, M. (2013). “Prevention of graphene restacking for performance boost of supercapacitors- a review”, Crystals, 3, 163-190.

Li, D., Zhou, J., Chen, X., Song, H. (2018). “Achieving ultrafast and stable Na-ion storage in $FeSe_2$ nanorods / graphene anodes by controlling the surface oxide”, ACS Appl. Mater. Interfaces, 10, 22841-22850.

Lee, J., Jeong, H., Lassarote L.R., Businaina, A., Kim, Y., Jung, Y.J., Lee, H. (2017). “Polypyrrole films with micro/nanosphere shapes for electrodes of high performance supercapacitors”, ACS Appl. Mater. Interfaces, 9, 33203-33211.

Lee, J., Young-Seok, J., Yang, M., Kang, B. (2022). “Facile fabrication of high-performance hybrid supercapacitor by one-step, self-grown copper nanopillar forest anchored with Fe_2O_3 anode”, Int. J. Precision Eng. and Manufac.-Green Technol., 9, 213-223.

Lee, D.G., Kim, B.H. (2016). "MnO_2 decorated on electrospun carbon nanofiber / graphene composites as supercapacitor electrode materials", Synth. Met., 219, 115-123.

Li, D., Zhou, J., Chen, X., Song, H. (2016). “Amorphous Fe_2O_3 / graphene composite nanosheets with enhanced electrochemical performance for sodium-ion battery”, ACS Appl. Mater. Interfaces, 8, 30899-30907.

Li, C., Zhang, X., Sun, C., Wang, K., Sun, X., Ma, Y. (2019). “Recent progress of graphene based materials in lithium-ion capacitors”, J. Phys. D., 52, Article number: 19143001.

Liu, J., Zhang, L., Wu, H.B., Lin, J., Shen, Z., Lou, X.W. (2014). “High-performance flexible asymmetric supercapacitors based on a new graphene foam / carbon nanotube hybrid film”, Energy Environ. Sci., 7, 3709-3719.

Ma, Y., Zhao, D., Chen, Y., Huang, J., Zhang, Z., Zhang, X., Zhang, B. (2019). “A novel core-shell polyaniline / graphene oxide / copper nanocomposite for high-performance and low-cost supercapacitors”, Chemical Papers, 73, 119-129.

Meng, Q.F., Cai, K.F., Chen, Y.X., Chen, L.D. (2017). “Research progress on conducting polymer based supercapacitor electrode material”, Nano Energy, 36, 268-285.

Mohammadi, A., Arsalani, N., Tabrizi, A.G., Moosavifard, S.E., Naqshbandi, Z., Ghadimi, L.S. (2018). “Engineering rGO-CNT wrapped Co_3O_4 nanocomposites for high-performance asymmetric supercapacitors”, Chem. Eng. J., 334, 66-80.

Moosavifard, S.E., El-Kady, M.F., Rahmanifar, M.S., Kaner, R.B., Mousavi, M.F. (2015). “Designing 3D highly ordered nanoporous CuO electrodes for high-performance asymmetric supercapacitors”, ACS Appl. Mater & Interfaces, 7(8), 4851-4860.

Ng, C.H., Lim, H.N., Hayase, S., Zaind, Z., Shafie, S., Huang, N.M. (2017)." Capacitive performance of graphene-based asymmetric supercapacitor", Electrochim. Acta, 229, 173-182.

Ning, P., Duan, X., Ju, X., Lin, X., Tang, X., Pan, X., Wang, T., Li, Q. (2016). “Facile synthesis of carbon nanofibers / MnO_2 nanosheets as high-performance electrodes for asymmetric supercapacitors”, Electrochim. Acta, 210, 754-761.

Rajkumar, M., Hsu, C.T., Wu, T.H., Chen, M.G., Hu, C.C. (2015). “Advanced materials for aqueous supercapacitors in the asymmetric design”, Prog. Nat. Sci. Mater. Int., 25, 527-544.

Shao, Y., El-Kady, M.F., Sun, J., Li, Y., Zhang, Q., Zhu, M., Wang, H., Dunn, B., Kaner, R.B. (2018). "Design and mechanism of asymmetric supercapacitors", Chem. Rev., 118, 9233-9280.

Shown, I., Ganguly, A., Chen, L.C., Chen, K.H. (2015). “Conducting polymer based flexible supercapacitor”, Energy Sci. Eng., 3, 2-26.

Seyyidin, S.T., Sovizi, M.R., Yaftian, M.R. (2016). “Enhancing lithium-sulfur battery performance by copper oxide@graphene oxide nanocomposite – modified cathode”, Chem. Pap., 70(12), 1590-1599.

Singu, B.S., Yoon, K.R. (2016). "Porous 3D-β-nickel hydroxide micro-flowers for electrochemical supercapacitors ", J. Ind. Eng. Chem., 33, 374-380.

Simon, P., Gogotsi, Y., Duan, B. (2014). “Where do batteries end and supercapacitors begin”, Science, 343, 1210-1211.

Su, F., Hou, X., Qin, J., Wu, Z. (2020). "Recent advances challenges of two-dimensional materials for high-energy and high power lithium ion capacitors", Batteries supercaps, 3, 10-29.

Sun, Y., Xue, J., Dong, S., Zheng, Y., An, Y., Ding, B., Zhang, T., Dou, H., Zheng, X. (2020). "Biomass-derived porous carbon electrodes for high-performance supercapacitors", J. Mater. Sci., 55, 5166-5176.

Sun, M.Q., Wang, G.C., Li, X.W., Cheng, Q.L., Li, C.Z. (2012). "Interfacial synthesis and supercapacitive performance of hierarchical sulfonated carbon nanotubes", Ind. Eng. Chem. Res., 51(10), 3981-3987.

Wang, X., Liu, I., Niu, Z. (2019). "Carbon based materials for lithium ion capacitors", Mater. Chem. Front., 3, 1265-1279.

Wang, J.G., Yang, Y., Huang, Z.H., Kang, F. (2013). "A high performance asymmetric supercapacitor based on carbon and carbon-MnO_2 nanofiber electrodes", Carbon, 61, 190-199.

Wang, Y., Ma, R., Liu, L. (2017). "A facile one-pot method for Co_3O_4 / graphene composite as efficient electrode materials for supercapacitors", Nano Brief Reports and Reviews, 12(8), Article number: 1750102.

Wen, J., Qin, T., Wng, Z., Jiang, X., Peng, S., Zhang, J., Hou, J., Huang, F., He, D., Cao, G. (2017). "Self-supported binder-free carbon fibers / MnO_2 electrodes derived from disposable bamboo chopsticks for high-performance supercapacitors", J. Alloys Compds., 699, 126-135.

Wu, T., Xu, L., Sun, H., Bao, Y., Yu, H., Guo, X., Hu, Q., Li, J. (2021). "Hierarchical shell/core electrodes with CuO nanowires based on carbon cloths for high-performance asymmetric supercapacitors", Ceramics International, 47, 33758-33765.

Qin, F., Tian, X., Guo, Z., Shen, W. (2018). "Asphaltene-based porous carbon nanosheet as electrode for supercapacitor", ACS Sustain Chem. Eng., 6, 15708-15719.

Xie, J.L., Cuo, C.X., Li, C.M. (2014). "Construction of one-dimensional nanostructures on graphene for efficient energy conversion and storage", Energy Environ. Sci., 7, 2559-2579.

Vadiyar, M.M., Bhise, S.C., Patil, S.K., Patil, P.S., Pawar, D.K., Ghule, A.V., Patil, P.S., Kolekar, S.S. (2015). "Mechanochemical growth of a porous $ZnFe_2O_4$ nano-flake thin film as an electrode for supercapacitor application", RSC Adv., 5, 45935-45942.

Yang, X., Lin, Z., Zheng, J., Huang, Y., Chen, B., Mai, Y., Feng, X. (2016). “Facile template-free synthesis of vertically aligned polypyrrole nanosheets on nickel foams for flexible all-solid state asymmetric supercapacitors”, Nanoscale, 8, 8650-8657.

Yazar, S., Arvas, B., Arvas, M.B., Yolacan, C., Sahin, Y. (2023). "A biocompatible and flexible supercapacitor for wearable electronic devices", J. Energy Storage, 74, Article number: 109400.

Zhang, T., Liu, J., Guan, H., Zhao, Y., Zhang, B. (2017). “Decoration of nickel hydroxide nanoparticles onto polypyrrole nanotubes with enhanced electrochemical performance for supercapacitors”, J. Alloys Compd., 721, 731-740.

Zhang, Y., Feng, H., Wu, X.B., Wang, L.Z., Zhang, A.Q., Xia, T.C., Dong, H.C., Li, X.F., Zhang, L.S. (2009). "Progress of electrochemical capacitor electrode materials: A review", Int. J. Hydrogen Energy, 34(11), 4889-4899.

Zhang, C., Wei, J., Chen, L., Tang, S., Deng, M., Du, Y. (2017). “All solid state asymmetric supercapacitors based on Fe-doped mesoporous Co_3O_4 and three-dimensional reduced graphene oxide electrodes with high energy and power densities”, Nanoscale, 9, 15423-15433.

Zhu, Y., Cao, C., Zhang, J., Xu, X. (2015). "Two-dimensional ultrathin $ZnCo_2O_4$ nanosheets: general formation and lithium storage application", J. Mater. Chem. A., 3, 9556-9564.

CHAPTER 7

COMPARATIVE STUDY ON PHYTOCHEMICAL SCREENING AND ANTIBACTERIAL ACTIVITY OF TAPINANTHUS LONGIFOLIA AND TAPINANTHUS GLOBIFERUS LEAVES EXTRACTS

Musa HALIMATU FAGO[1]* and Zainab AHMAD MUHAMMAD[2]

DOI: https://dx.doi.org/10.5281/zenodo.10444749

[1 -2]Department of Pure & Industrial Chemistry, Faculty of Natural and Applied Sciences, Umaru Musa Yaradua University, Katsina, Nigeria
*Corresponding author: halimatumusafago@gmail.com

INTRODUCTION

The term 'medicinal plants' refers to a wide variety of plants that are used in herbalism, and some of these plants have been shown to have medicinal properties. Medicinal plants are a rich source of compounds that can be used in the development of drugs and other therapeutic products. They also play a critical role in the cultures of many societies around the world. In addition to their medicinal value, some plants are also important sources of nutrition. Examples of plants with medicinal properties include ginger, green tea, walnuts and some others plants.(Bassam, 2012). Medicinal plants constitute the main source of new pharmaceuticals and healthcare products. Ivanova *et al.,* (2005). The use of medicinal plants in the industrialized societies has been traced to the extraction and development of several drugs from these plants as well as from traditionally used herbal medicine. Extraction and characterization of several active phytocompounds from plants have given birth to some high activity profile drugs. Vaghasiya *et al.*, (2011). Plants contain substances that can be used for beneficial purposes in one or more of their organs, and these substances can serve as precursors for the production of useful drugs. Plants that contain these substances are known as medicinal plants. Thousands of these plant species have been used to treat various ailments for generations (Ojewole, 2008). In Nigeria, the use of traditional medicine is widespread and herbal medicines are popular in the treatment of many diseases due to the belief that they are safe, easily available and with less side effects.

Phytochemical provides health benefits for human, they are biologically active, naturally occurring chemical compounds found in plants, which provide health benefits for humans further than those attributed to macro-nutrients and micro-nutrients. Hollman *et al.,* (1996). They protect plants from disease and damage and contribute to their colour, aroma, and flavor. Phytochemicals are not essential nutrients and are not required by the human body for sustaining life but have important properties to prevent or to fight against some common diseases (Parekh and Chanda, 2007). Phytochemical screening of plants has revealed the presence of numerous chemicals including alkaloids, tannins, flavonoids, steroids, glycosides and saponins etc. Secondary metabolites of plants serve as defense mechanisms against predation by many microorganisms, insects and herbivores. Vaghasiya *et al.*, (2011).

Tapinanthus is a species in the Loranthaceae family. It is locally called Kauchi in Hausa Northern Land (Burkill, 2000). It is a semi-parasite with glabrous pendulous stems up to 1.2 m long with presumably roots that mostly grows on the branches of a large number of tree species of the genera Vitellaria, Kola, Citrus (L.), Combretum, Acacia, Aloe Vera and Terminalia as host (Roodt, 1989). It is used traditionally to treat many ailments including inflammations, malaria, bacterial infections, pain relief and ulcers (Burkill, 2000). Infection by Tapinanthus species can cause significant damage to the branches of the host plant. The branches above the point of attachment may become less vigorous, develop galls, bend, and sometimes die. If the host plant is poorly managed or experiencing drought stress, the damage may be more severe and can even lead to the death of the entire plant. Boussim *et al*., (2004)

METHODOLOGY

Sample collection and Identification

Fresh healthy, mature leaves of Tapinanthus Longifolia and Tapinanthus globiferus were collected from a farm in Bani'iza village in Ajiwa Local Government Area of Katsina state. The leaves were then Identified and authenticated in the Herbarium Unit of Biology Department, Faculty of Natural and Applied Sciences, Umaru Musa Yar'adua University Katsina, where voucher specimen are (UMYUH-2516) and (UMYUH-2517) of Tapinanthus longifolia and Tapinanthus globeferus were deposited in the Herbarium respectively.

Sample preparation

The Collected leaves were washed with distilled water in order to remove dust. The leaves were shade dried for six days, finely grounded into powder using pestle and mortar and stored in an air tight container for subsequent analyses.

Preparation of the Extract

The crude extracts were prepared using maceration method. Thus, 100g of the powdered plant materials was weighed and treated separately with 250ml of ethyl acetate for 72hours in a stoppered container. The mixtures were filtered using whattman filter paper (No.1) into a conical flask. The filtrate was

evaporated to dryness at 50°C on a thermostatic water bath in order to afford the corresponding extract, the crude extract was further analyzed for phytochemical test.

Qualitative Phytochemical Screening

Phytochemicals are non-nutritive plant chemicals that contain protective, disease-preventing compounds. Chemical screening test were carried out on the ethyl acetate extract and on the powdered specimens using standard procedures as described by Shaikh and Patil, (2020). To identify the presence or absence of secondary metabolites, such as Alkaloids, flavonoids, tannins, steroids, saponins, phenols, terpenoids and cardiac glycosides etc.

Test for Alkaloids

100mg of the crude extracts were dissolved Individually in dilute hydrochloric acid, afterward the solution was filtered. the filtrate was tested carefully with various alkaloidal reagents.

Wagner's Test

2 drops of Wagner's reagent were added into 3ml of the filtrate along the side of the test tube, Formation of reddish-brown precipitate indicated the presence of Alkaloid.

Mayer's Test

2 drops of Mayer's reagent were added into 3ml of the filtrate along the side of the test tube, a white or creamy precipitate Indicated the presence of Alkaloid.

Test for Flavonoids

Various methods were used to determine the presence of flavonoids in the plant sample. 1g of the crude extract was heated with 10ml of ethyl acetate over a water bath for 3mins, the mixture was filtered

Ammonia Test

3ml of the filtrate was shaken vigorously with 1ml of dilute ammonium solution. A yellow Coloration was observed indicating the presence of flavonoids.

Lead acetate test

3ml of the filtrate was treated with 2 drops of 5% lead acetate solution. Formation of yellow color precipitate indicated the presence of flavonoids.

Alkaline Test

4ml of the filtrate was treated with 3ml of distilled water and boiled for 5 mins. 3 drops of dilute NaOH solution was added. The color changes from colorless to yellow. Then, 3 drops of 1 % of HCl was added into the mixture. The presence of flavonoids was interpreted by observing the decolorization of the yellow colour.

Test for Saponins (Frothing test)

50mg of the crude extract was dissolved in 10ml of distilled water in a test tube. the test tube was covered tightly and shaken vigorously for 30sec, A Honey comb like Froth was formed and it showed the presence of Saponins.

Test for Steroids (Salkowski's Test)

0.3g of the Crude extract was dissolved in 2ml of chloroform and 3ml of Concentrated Sulphuric acid was carefully added, two layers were formed, a lower layer which is in yellow color with green fluorescence and a reddish brown color on upper layer which was interpreted as a steroid ring.

Test for Tannins (Braymer□s test)

0.3g of the crude extract was boiled with 4ml of distilled water in a test-tube and then filtered. 3 drops of 10% of ferric chloride solution were added to the filtrate, a brownish-green coloration Indicates the presence of tannins.

Test for Terpenoids (Salkowski's Test)

0.2ml of the crude extract was mixed with 2ml of Chloroform and 3ml of Concentrated Sulphuric acid was carefully added to form a layer, a reddish-

brown Coloration at the interface indicates positive results for the presence of terpenoids.

Test for Phenolic Compounds (Ferric Chloride test)

0.5g of the crude extract was boiled with 5ml of distilled water in a test tube and then filtered. A few drops of 5% of ferric Chloride solution were added. A dark green Coloration indicated the presence of phenolic Compounds.

Test for Cardiac glycosides (Keller killiani□s test)

0.2g of the crude extract was dissolved in 2ml of glacial acetic acid, A few drops of 5% ferric chloride solution and 1ml of concentrated sulphuric acid was added. Formation of Green-blue precipitate indicated the presence of glycosides.

Antibacterial Activity Test

The disk diffusion method was adopted as a local antibacterial testing method and both the crude plant extracts exhibited antibacterial activity at concentrations ranging from 250mg/ml, 125mg/ml, 62.5mg/ml, and 31.25mg/ml

Sample preparation and serial dilution

1g of the extracts and 2ml of (DMSO) was measured and used for serial dilution and sent to autoclave prior to use for sterilization. This gave a stock solution which contained a concentration of 250mg/ml. The solution was then transferred into a plain containers and mixed well by using vortex mixer and water bath sonicator. Three dilutions were additionally made from each of the extracts as 250mg/ml, 125mg/ml, 62.5 mg/ml and 31.25mg/ml respectively (NCCLS, 2004).

Preparation of Mueller Hinton agar (MHA)

Mueller Hinton agar were used for the antibacterial activities. Mueller Hinton agar was prepared i.e**.** 3.9g of Mueller Hinton agar was dissolved in 100ml of distilled water in 500ml conical flask. Magnetic Stirrer was used to stir the mixture to ensure proper mixing. After stirring, MHA was autoclaved for sterilization at temperature of 121°C for 15 minutes, After autoclaved, the

hot sterilized MHA solution was allowed to cooled for at least 5 minutes, and then poured into the petri-plates in the laminar air flow cabinet. Each of the petri-plates contained approximately 25ml of MHA solution which can only occupy 60-70% of the petri plate. The Mueller Hinton agar solution was allowed to solidify in the cabinet and the UV of the laminar air flow cabinet was on for 15 minutes to achieve sterilization. Sapkota, *et al.,* (2020).

Preparation of the Disk and Impregnation

From the four different concentrations of each Extracts which were 250mg/ml, 125mg/ml, 62.5mg/ml and 31.25 mg/ml. Sterile disk punched using Whattman filter paper No.2 were impregnated into each of the respective plain containers containing four different concentrations and allowed to soak for 30minutes and dispensed in each of the already seeded plates of Staphylococcus aureus and pseudomonas aeruginosa. Ciprofloxacin was used as a bacterial positive control while fresh disc soaked in distilled water was used as a bacterial negative control and incubated at 37°C for 24 hours (NCCLS, 2004).

Result Interpretations

Following the 24-hour incubation, a clear zone was observed as zone of inhibition which was measured in millimeter□s (mm) recorded and tabulated.

Determination of Minimum Inhibitory Concentration (MIC)

MIC of both the crude extracts were determined using the tube dilution method. Tekwu, *et al*., (2012). Doubling dilutions of the extracts was carried out in well labeled plain containers using nutrient broth as diluents. The plain containers were then inoculated with 0.1ml of standard inoculums and incubated at 37^0C for 24hrs to observe turbidity (growth). The least concentration showing no visible sign of growth which gave no turbidity of the medium will be taken as the MIC as compared with controls of; 1 (the broth with extracts each only) and 2 (broth with test organisms only).

Determination of the Minimum Bactericidal Concentration (MBC)

The result from the MIC tubes will be used to determine the MBC. The contents of all the tubes will be inoculated onto sterile nutrient agar plates using a wire-loop and the plates was incubated aerobically at 37^0C for about 24 hours.

The MBC values was read as the least concentrations that totally killed the test organisms, which was indicated by the complete absence of growth. (Joshua and Takudzwa, 2013).

RESULTS AND DISCUSSION

Table 1. Results for Qualitative Analysis of Phytochemical Constituents of ethyl acetate leaf extract of Tapinanthus longifolia

S/N	Phytochemical constituents	Test Performed	Results
1	Alkaloids	Wagner's test	+++
		Mayer's test	+++
2	Flavonoids	Ammonia test	+++
		Lead acetate test	+++
		Alkaline test	+++
3	Saponins	Frothing test	+
4	Steroids	Salkowski's test	+++
5	Tannins	Braymer□s test	++
6	Terpenoids	Salkowski's Test	+++
7	Phenolic Compounds	Ferric chloride test	+++
8	Glycosides	Keller killiani□s test	+++

Key: +++ (Highly presence of phytochemical constitutes), ++ (Moderately presence of phytochemical constitutes), + (Trace presence of phytochemical constitutes)

Qualitative analysis of phytochemical constituents of ethyl acetate leaves extracts of Tapinanthus longifolia and Tapinanthus globiferus

The qualitative phytochemical analysis was performed with ethyl acetate extracts of the leaves of Tapinanthus longifolia and Tapinanthus globiferus. The phytochemical analysis of Tapinanthus longifolia showed alkaloids, flavonoids, steroids, terpenoids, phenolic compounds and glycosides were

highly present, Tannins showed moderately present whereas saponins showed trace present as shown in (table 1).

Table 2. Results for Qualitative Phytochemical Constituents of ethyl acetate leaf extract of Tapinanthus globiferus.

S/N	Phytochemical constituents	Test Performed	Results
1	Alkaloids	Wagner's test	+++
		Mayer's test	+++
2	Flavonoids	Ammonia test	+++
		Lead acetate test	+++
		Alkaline test	+++
3	Saponins	Frothing test	++
4	Steroids	Salkowski's test	+++
5	Tannins	Braymer□s test	+
6	Terpenoids	Salkowski's Test	+++
7	Phenolic Compounds	Ferric chloride test	++
8	Glycosides	Keller killiani□s test	+++

Key: +++ (Highly presence of phytochemical constitutes), ++ (Moderately presence of phytochemical constitutes), + (Trace presence of phytochemical constitutes).

Qualitative phytochemical analysis of Tapinanthus globiferus leaf extracts showed alkaloids, flavonoids, steroids, terpenoids and glycosides were highly present, saponins and phenolic compounds were moderately present whereas Tannins showed trace presents as shown in (table 2).

The leaves of both Tapinanthus longifolia and Tapinanthus globiferus revealed the presence of Alkaloids, flavonoids, saponins, steroids, Tannins, terpenoids, phenolic Compounds and glycosides. This observation was supported by the work of (Bassey, 2012). Who reported that the plants T. Globiferus have contained Alkaloids, flavonoids, saponins, tannins, terpenoids and cardiac glycosides. These phytochemicals present Antibacterial activity on the leaves extracts as shown in (Table 1 and 2). The various phytochemical

compounds detected are known to have beneficial importance in medicinal sciences. In addition, presence of this phytochemicals are accountable for its medicinal uses such as: antibacterial, antifungal antidiabetics, antioxidant and antidiarrhoe etc. As it was reported by (Lata and dubey, 2010) that medicinal benefits of plant depend on the quality of the bioactive constituents including tannins, phenolic compounds, alkaloid and flavonoid which are present in the understudied aquatic plant. The presence of secondary metabolites in the mistletoes and the host plant has been reported to be responsible for different pharmacological and physiological actions of plant extracts (Cragg and Newman, 2005). Flavonoids have been referred to as nature□s biological response modifiers, because of their inherent ability to modify the body□s reaction to allergies and virus and they showed their anti-allergic, anti-inflammatory, anti-microbial and anti-cancer activities (Aiyelaagbe and Osamudiamen, 2009). Tannins are used in antihemorrhoidal, hemostatic and anti-diarrheal preparations. Saponins are helpful in lowering cholesterol, as antioxidant and anti-inflammatory agents. Najafi, *et al*., (2010). Terpenoids are large and diverse class of naturally occurring organic chemicals found in all classes of living organisms. They have antibacterial properties. Selvan, *et al*., (2012). Steroids have been reported to have antibacterial properties and they are very important compounds especially due to their relationship with compounds such as sex hormones. Yadav, *et al*., (2011). Terpenoids have been shown to have a variety of important pharmacological activities, including anti-inflammatory, anticancer, anti-malarial, cholesterol-reducing, anti-viral and antibacterial properties.

Table 3. Results for Antibacterial Activity of Tapinanthus longifolia and Tapinanthus globiferus leaves extract using disc diffusion method

EXTRACT	STUDY OF INDICATOR TEST BACTERIA	Zone of inhibition in (mm)				
		250 (mg/ml)	125 (mg/ml)	62.5 (mg/ml)	31.25 (mg/ml)	Control
Tapinanthus longifolia	Staphylococcus aureus	9	8	7	7	33
	Pseudomonas aeruginosa	10	10	9	9	36
Tapinantus globiferus	Staphylococcus aureus	11	9	9	8	33
	Pseudomonas aeruginosa	13	12	10	9	36

Antibacterial activity of Tapinanthus Longifolia and Tapinanthus globiferus leaves extracts against some bacteria Isolates

The antibacterial activity was carried out using disc diffusion method, the Concentration of the extracts were range from 250mg/ml,125mg/ml,62.5mg/ml and 31.25mg/ml. The results of the ethyl acetate extracts of Tapinanthus Longifolia and Tapinanthus globiferus leaves exhibited antibacterial activity against the tested strain: staphylococcus aureus and Pseudomonas aeruginosa, The diameter for the zone of Inhibition manifested by the Tapinantus longifolia extracts ranged from (7-9mm) against staphylococcus aureus while the zone of inhibition for pseudomonas aeroginosa ranged from (9-10mm) as shown in (Table 3), The highest value for the zone of Inhibition was (10mm) against pseudomonas aureginosa with the Inhibitory Concentration of 250mg/ml. The lowest value for the zone of Inhibition was (7mm) against staphylococcus aureus with the Inhibitory Concentration of 31.25mg/ml.

The results of the Tapinanthus globiferus leave extract showed antibacterial activity against staphylococcus aureus and Pseudomonas aeruginosa as indicated by a clear zone of inhibition ranged from (8-11mm) against staphylococcus aureus while the zone of inhibition for pseudomonas aeriginosa ranged from (9-13mm) in diameter as shown in (Table 3)

respectively. The highest value for the zone of Inhibition was (13mm) against pseudomonas aureginosa with the Inhibitory Concentration of 250mg/ml. The lowest value for the zone of Inhibition was (8mm) against staphylococcus aureus with the Inhibitory Concentration of 31.25mg/ml.These shows that the higher the Concentration of the extracts the higher the zone of inhibition. Comparatively, Tapinanthus globiferus extracts were more active than the Tapinanthus longifolia extracts against all the microorganisms. The zone of inhibitions for both the Tapinanthus longifolia and Tapinanthus globiferus leave extracts were ranging from 7-13mm in diameter (Table 3) The highest value for the zone of Inhibition was (13mm) noted in Tapinanthus globiferus extract against pseudomonas aureginosa with the Inhibitory Concentration of 250mg/ml. The lowest value for the zone of Inhibition was (7mm) noted in Tapinanthus longifolia extract against staphylococcus aureus with the Inhibitory Concentration of 31.25mg/ml.

The variations in the antibacterial activities of the aqueous leaf extract of this mistletoe obtained from different hosts might be due to differences in the contents of its phytochemical compositions and host as these affect mistletoe antimicrobial effects (Osadebe, *et al.,* 2008 and Bassey, 2012). The outstanding antibacterial activity of T. globiferus obtained might be attributed to the higher concentration of flavonoids observed as analyzed in this study as flavonoids was known to disrupt the functions of viruses and bacteria. Generally, the activity demonstrated by the extracts may be due to the presence of alkaloids (karou, *et al.,* 2005), steroids (Silva, *et al.,* 2003), glycoside (Jacques, *et al.,* 2011) and saponins (Soetan, *et al*., 2006).

Table 4. Minimum Inhibitory Concentration of Tapinanthus Longlifolia and Tapinanthus globiferus Leaves Extract

EXTRACT	STUDY OF INDICATOR TEST BACTERIA	Minimum Bactericidal Concentration (MBC)				
		31.25 (mg/ml)	62.5 (mg/ml)	125 (mg/ml)	250 (mg/ml)	Control
Tapinanthus Longlifolia	Staphylococcus aureus	-	-	-	+	+
	Pseudomonas aeruginosa	-	+	+	+	+
Tapinanthus globiferus	Staphylococcus aureus	-	-	+	+	+
	Pseudomonas aeruginosa	-	+	+	+	+

Positive (+): Turbidity indicating presence of growth; Negative (□): No turbidity indicating absence of growth

The MIC and MBC of Tapinanthus Longlifolia and Tapinanthus globiferus Leaves Extract

After 24 hours of incubation in anaerobic condition at 37ºC, turbidity was noticed in all the plain containers ranging from 31.25 to 250 mg/ml containing the ethyl acetate leaves extracts of T. Longifolia and T. globiferus indicating the growth of bacteria as shown in (Table 4). Presence or absence of turbidity was denoted as + or □ respectively. The minimum Inhibitory Concentration (MIC) test of the ethyl acetate leaves extracts of T. Longifolia had an inhibitory effect at 125mg/ml, 62.5mg/ml, and 31.25mg/ml on Staphylococcus aureus Whereas in concentrations of 31.25 mg/ml, no turbidity was seen exhibiting inhibition of bacterial growth on pseudomanas aeroginosa. The minimum inhibitory concentration of the ethyl acetate leaves extract of T. globiferus was 62.5 and 31.25mg/ml on Staphylococcus aureus, and had an inhibitory effect at the Concentration of 31.25mg/ml on pseudomonas aeroginosa.

Tables 5. Minimum Bactericidal Concentration of Tapinanthus Longlifolia and Tapinanthus globiferus Leaves Extract

EXTRACT	**STUDY OF INDICATOR TEST BACTERIA**	**Minimum Bactericidal Concentration (MBC)**				
		31.25 (mg/ml)	**62.5 (mg/ml)**	**125 (mg/ml)**	**250 (mg/ml)**	**Control**
Tapinanthus Longlifolia	Staphylococcus aureus	-	-	-	+	+
	Pseudomonas aeruginosa	-	+	+	+	+
Tapinanthus globiferus	Staphylococcus aureus	-	-	-	+	+
	Pseudomonas aeruginosa	-	-	+	+	+

Positive (+): Turbidity indicating presence of growth; Negative (□): No turbidity indicating absence of growth

The trend of events in the Minimum Bactericidal Concentration (MBC) test presented in (Table 5) was the same as observed in the minimum inhibitory concentration (MIC) test. When bacterial growth at different concentrations of ethyl acetate extracts of T. longifolia and T. globiferus leaves was assessed after 24 hours, the MIC and MBC of S. aureus in both the leaves extracts was observed maximum for a concentration of 31.25 to 125mg/ml, indicating it has both bacteriostatic and bactericidal activity (Tables 5). the optimum MIC was obtained with 31.25mg/ml as the least inhibitory Concentration. These results thus confirm that the MIC and MBC of the ethyl acetate extracts of T. longifolia and T. globiferus leaves was found to be effective at the Concentration of 31.25mg/ml.

Conclusion

The phytochemical screening and anti-bacterial activity of the ethyl acetate extract of Tapinanthus longifolia and Tapinanthus globiferus leaves provided valuable insights into the potential medicinal properties of these plant extracts. The project shed light on the diverse phytochemical constituents

present in both Tapinanthus longifolia and Tapinanthus globiferus leaves, highlighting their therapeutic potential. The Phytochemical screening revealed the presence of various bioactive compounds such as alkaloids, flavonoids, saponins, steroids, terpenoids tannins, phenolic compounds and glycoside in the ethyl acetate leaves extracts. These compounds are known for their antibacterial properties and have been extensively studied for their therapeutic applications. The antibacterial activity conducted on the ethyl acetate extracts of both Tapinanthus longifolia and Tapinanthus globiferus leaves demonstrated their potentials as the natural alternatives for combating bacterial infections. The extracts exhibited significant inhibitory effects against staphylococcus aureus and pseudomonas aeruginosa at the concentration ranging from 250mg/ml, 125mg/ml, 62.5mg/ml, and 31.25 mg/ml which revealed that tapinanthus globiferus extracts were more active than the tapinanthus longifolia extracts against all the microorganism with a clear zone of inhibition ranging from 7-13mm in diameter. The results thus confirm that the MIC and MBC of the ethyl acetate extracts of T. longifolia and T. globiferus leaves was found to be effective at the Concentration of 31.25mg/ml. The antibacterial activity displayed by these extracts indicates their potential for the development of new antimicrobial agents.

Recommendation

In this study, ethyl acetate extraction was used for the phytochemical analysis and antibacterial activity. It was recommended that solvent partitioning using solvents of different polarities should be done to show the chemicals and activity of each fraction.

It is recommended that further studies should be carried out on the Phytochemicals profiling of these leaves to probe the detailed antibacterial activity of the constituent molecules using modern chromatography techniques such as Gas chromatography and High performance liquid chromatography (HPLC).

REFERENCES

Aiyelaagbe, O. O. and Osamudiamen, P. M. (2009): Phytochemical screening for active compounds in mangifera indica, *Plant, Sci. Res*, Vol.2**(1):** pp.11-13.

Bassam, A. (2012): Clinical Pharmacy Discipline, School of Pharmaceutical Sciences, University of Sains Malaysia. *Pharmaceut Anal Acta,* Vol. 3**(10)**.

Bassey, M. E. (2012): Phytochemical Investigation of Tapinanthus globiferus (Loranthaceae) From Two Hosts and the Taxonomic Implications. *International Journal of Chemical, Environmental and Pharmaceutical Research*, Vol. 3**(2)**: pp.174-177.

Boussim, I. J., Guinko, S., Tuquet, C. and Salle, G. (2004): Mistletoes of the agroforestry parklands of Burkina Faso. *Agroforostry systems*, Vol. 60**(2)**: pp.39-49.

Burkill, H. M. (2000): Useful Plants of West Tropical Africa. *2nd edition Royal Botanic Gardens, Kew England, Vol*. 5: Pp. 548-560.

Cragg, G. M. and Newman, D. J. (2005): International collaboration in drug discovery and development from natural sources.*Pure Applied Chemistry*. Vol. 77**(11)**: pp.1923-1942.

Hollman, P. C. H., Hertog, M. G. L. and Katan, M. B. (1996): Analysis and health effects of flavonoids. *Food Chemistry*, Vol. 57: pp. 43-46.

Ivanova, D., Gerova, D., Chervenkov, T. and Yankova, T. (2005): Polyphenols and antioxidant capacity of Bulgarian medicinal plants. *Journal of Ethnopharmacology*. Vol.9(6): pp. 145-150.

Jacques, k., Laure, B. K., Jules, R. K., Alembert, T. and Zacharias, T. F. (2011): Antimicrobial glycosides and derivatives from roots of picarlima nitida. *International journal of chemistry*, Vol. 3**(2)**: pp. 23-31.

Joshua, M. and Takudzwa, M. (2013): Antibacterial properties of Mangifera indica on Staphylococcus aureus. *African Journal of Clinical and Experimental Microbiology*, Vol.14**(2):** pp. 62-74.

Karou, D., Aly, S., Antonella, C., Saydou, Y., Carla, M., Jacques, S., Vitloro, C. and Alfred, S. T. (2005): Antibacterial activity of alkaloids from Sida acuta.*Journal of biotechnology*. Vol.4**(8)**: pp. 823-828.

Lata, N. and Dubey V. (2010). Preliminary phytochemical screening of Eichhornia crassipes: the world□s worst aquatic Weed. *Journal of Pharmacy Research, Vol*. 3**(12)**: pp. 40-42.

Najafi, S., Sanadgol, N., Nejad, B. S., Beiragi, M. A. and Sanadgo, E. (2010): Phytochemical screening and antibacterial activity of Citrullus colocynthis (Linn.) Schrad against Staphylococcus aureus. *J Med Plants Res, Vol.* 4**(22)**: pp. 2321-2325.

NCCLS □ National Commity for clinical laboratory standards. (2004): Performance standadard for antimicrobial susceptibility testing. *Fourteenth informational supplemented.* M100-S14, Wayne, P. A., U. S. A.

Ojewole, E. O. (2008). Pharmacognosy: Fundamentals, applications, and strategy (2nd ed.). Science and Technology Book Co. pp.208.

Osadebe, P. O., Dieke, C. A. and Okoye, F. B. C. (2008): A Study of the Seasonal Variation in the Antimicrobial Constituents of the Leaves of Loranthusmicranthus Sourced from Percia American. *Research Journal of Medicinal Plant,* Vol. 2**(1)**: pp.48-52.

Parekh, J. and Chanda, S. (2007): Antibacterial and phytochemical studies on twelve species of Indian medicinal plants. *Afr. J. Biomed. Res.*, Vol. 10: pp. 175-181.

Roodt, V. (1989): Common Wild Flowers of the Okavango Delta. Medicinal Uses and Nutritional Values The Shell Field Guide Series: *Part II. Windhoek: Gamsberg Publishers;*

Sapkota, S., Khadka, S., Adhikari, S., Parajuli, A., Kandel, H. and Ramesh, S. R. (2020): Microbial Diversity and Antibiotic Susceptibility Pattern of Bacteria Associated with Motorcycle Helmets, *International Journal of Microbiology*, vol.20, pp.7, Article ID 8877200, https://doi.org/10.1155/2020/8877200.

Selvan, R. T., Mohideen, A. K. S., Sheriff, M. A. and Azmathullah, N. M. (2012): Phytochemical screening of Acalypha Indica L. Leaf extracts.*Int J Appl Biol Pharm Technol.* Vol. 3**(2)**: pp. 158-161.

Shaikh, J. R., Patil, M. K. (2020): Qualitative tests for preliminary phytochemical screening: An overview. *Int J Chem Stud* , Vol. 8**(2)**: pp.603-608. DOI: 10.22271/chemi.2020.v8.i2i.8834

Silva, H. T., Marcos, J. S., Evandio, W., Izabel, Y. I. and Dioneia, C. R. (2003): Antimicrobial activity of flavonoids and steroids isolated from two chomolaenaspecie. *Brazillian journal of pharmaceutical sciences*, Vol. 39**(4)**: pp. 403-408.

Soetan, K., Oyekunle, M. A., Aiyelaagbe, O. O. and Fafunso, M. A. (2006): Evaluation of the antimicrobial activity of saponins extracts of sorghum Bicolor L. Moench. *Africa Journal of Biotechnology*, Vol. 5**(23)**: pp.2405-2407.

Tekwu, E. M., Pieme, A. C. and Beng, V. P. (2012): Investigations of antimicrobial activity of some Cameroonian medicinal plant extracts against bacteria and yeast with gastrointestinal relevance. *Journal of Ethnopharmacology*, Vol.14**(2)**:pp. 265-273.

Vaghasiya, Y., Dave, R. and Chanda, S. (2011): Phytochemical analysis of some medicinal plants from Western Region of India. *Research Journal of Medicinal Plants*. Vol. 5: pp. 567□576

Yadav, R. N. S., Agarwala, M. (2011): Phytochemical analysis of some medicinal plants. *J Phytology*. Vol.3**(12)**: pp.10-14.

CHAPTER 8

GLYCO-ANALYSIS OF MONOCLONAL ANTIBODIES

Doç. Dr. Hacı Mehmet KAYILI[1]

DOI: https://dx.doi.org/10.5281/zenodo.10444753

[1]Karabük University, Faculty of Engineering, Department of Medical Engineering, Karabük, Türkiye. h.mehmetkayili@karabuk.edu.tr, ORCID ID: 0000-0002-6740-0645

INTRODUCTION

Protein biopharmaceuticals are indispensable therapeutic agents extensively utilized in clinical applications to treat a range of illnesses, such as cancer, diabetes, infections, inflammatory conditions, and autoimmune disorders. Monoclonal antibodies (mAbs) and various recombinant proteins, spanning hormones, fusion proteins, growth factors, cytokines, vaccines, blood factors, and therapeutic enzymes, are produced as biopharmaceuticals using diverse biotechnological methodologies. The last few years have witnessed a notable surge in the approval of protein biopharmaceuticals for human use in the United States and the European Union, with the count nearing 250, establishing a robust multi-billion-dollar industry(Walsh, 2014).

The escalating sales trajectory of protein biopharmaceuticals underscores their burgeoning prominence, with the potential to encompass a significant share of the pharmaceutical market. Given that protein biopharmaceuticals undergo enzymatic and chemical modifications during expression and purification, resulting in structural and functional diversity, the monitoring of post-translational modifications (PTMs) becomes imperative. PTMs such as oxidation, deamidation, glycosylation, and aggregation play pivotal roles in these alterations(Houde, Peng, Berkowitz, & Engen, 2010). To secure the production of protein therapeutics that are both safe and of superior quality, it is essential to meticulously monitor post-translational modifications (PTMs) through various methods. This scrutiny is necessary for obtaining approval for biosimilar drugs from regulatory bodies like the United States Food and Drug Administration (FDA) and the European Medicines Agency (EMA).

The majority of biopharmaceuticals, exceeding 60% of approved counterparts, are glycoproteins, with glycosylation exerting a profound influence on the efficacy and safety of therapeutic proteins(Zheng, Bantog, & Bayer, 2011; Zheng, Yarmarkovich, Bantog, Bayer, & Patapoff, 2014). Glycosylation also impacts the pharmacokinetics and pharmacodynamics of therapeutic proteins, making the production of appropriately glycosylated therapeutic proteins a challenging undertaking(Sola & Griebenow, 2010). Consequently, glycan analysis of therapeutic proteins using a reliable methodology assumes critical importance in the development of biosimilar drugs. This analytical step not only facilitates the elucidation of glycan

structures but also enables the monitoring of safety and quality during the developmental stages of protein biopharmaceuticals intended for human use.

Mass spectrometry, when coupled with chromatographic or electrophoretic separation techniques, emerges as the preeminent and potent method for glycan analysis in therapeutic glycoproteins. The method's sensitivity, speed, and resolution power render it the preferred choice. Furthermore, mass spectrometry has played a foundational role in FDA biologics license applications (BLAs), with glycosylation analysis conducted by mass spectrometry encompassing 71% of the scrutinized BLAs(Rogstad et al., 2016). This review concentrates on mass spectrometry-based glyco-analytical methods tailored for profiling glycan heterogeneity at glycosylation sites in protein biopharmaceuticals.

Mass spectrometry-based glyco-analytical strategies emerge as the preferred and robust choice for assessing the safety and quality of protein therapeutics. This preference is attributed to the distinctive mass spectrometric features, including high speed, mass accuracy, and resolution.

This chapter critically examines the most widely applied methods, encompassing diverse glyco-analytical strategies and their applications in elucidating glycan structures within protein biopharmaceuticals. The inherent advantages of mass spectrometry, such as rapidity, precision, and resolution, underscore its efficacy in advancing our understanding of glycosylation patterns and ensuring the quality and safety of therapeutic proteins.

Glyco-Analytical Strategies

Numerous glyco-analytical methods utilizing diverse mass spectrometric instruments have been developed for the comprehensive characterization of protein biopharmaceuticals. Electrospray ionization (ESI) and matrix-assisted laser desorption/ionization (MALDI) represent the prevailing mass spectrometric approaches employed in the analysis of glycans, conducted in both negative and positive ionization modes(Dotz et al., 2015; Oh et al., 2016; Rogstad et al., 2016; Sandra, Vandenheede, & Sandra, 2014; Stavenhagen, Kolarich, & Wuhrer, 2015; L. Zhang, S. Luo, & B. L. Zhang, 2016b). The glyco-analytical strategies based on mass spectrometry operate at three distinct levels, encompassing the analysis of intact proteins (in their native or reduced forms), glycopeptides, and released glycans. These analytical levels are

mutually complementary and essential for the comprehensive characterization of the glycan structures present in therapeutic glycoproteins.

Intact Protein Level for Glycan Profiling

The application of top-down proteomics is frequently employed for the glycosylation analysis of therapeutic proteins. In this approach, molecular ions of biomolecules are generated through electrospray ionization (ESI) or matrix-assisted laser desorption/ionization (MALDI) and introduced into the mass analyzer(Cui, Rohrs, & Gross, 2011; Staub, Guillarme, Schappler, Veuthey, & Rudaz, 2011; Whitelegge, 2013). At the intact protein level, analysis can encompass both the native and reduced forms of therapeutic proteins. Additionally, the enzyme PNGase F can be utilized to release *N*-glycans from therapeutic proteins before intact mass spectrometric analysis. Comparing conditions before and after PNGase F treatment provides enhanced structural information and insights into *N*-glycan profiles.

In the initial applications of intact monoclonal antibody (mAb) analysis, MALDI-TOF has been particularly useful for determining the mass of an intact antibody due to its unlimited mass range(Z. Zhang, H. Pan, & X. Chen, 2009). However, MALDI-TOF's limitations in mass accuracy and low peak resolution for large molecules may hinder effective resolution of glycoform mass peaks, thereby impeding glycan analysis at this level. In contrast, electrospray ionization (ESI) techniques frequently yield large multiply charged ions in the analysis of biomacromolecules, enabling efficient analysis of large molecules with ESI-MS. Modern ESI mass spectrometers equipped with high-throughput mass analyzers offer exceptional resolution, mass accuracy, and sensitivity, rendering ESI the preferred method for analyzing the glycans of protein therapeutics at the intact protein level.

Middle-down proteomics, a complementary application to the top-down approach, involves the mass determination of large fragments or subunits of protein therapeutics following limited proteolysis (Z. Q. Zhang, H. Pan, & X. Y. Chen, 2009). The reduction of disulfide bonds in monoclonal antibodies (mAbs) can yield heavy chains (~50 kDa) and light chains (~25 kDa) through a chemical reaction. Various proteases, such as papain(Zheng et al., 2011), pepsin(Majumdar et al., 2012), Lys-C(Kim et al., 2010), and ideS(Fornelli, Ayoub, Aizikov, Beck, & Tsybin, 2014), have been introduced to obtain Fab

(~50 kDa) or (Fab)′2 (~100 kDa) and Fc (~50 kDa) fragments of mAbs through the cleavage of the hinge region under native or reduced conditions.

Glycan Profiling at the Glycan and Glycopeptide Levels

The predominant method for glycan profiling of monoclonal antibodies (mAbs) is conducted at the glycan level(L. Zhang et al., 2016b). This approach involves the enzymatic release of glycans from mAbs. The enzyme PNGase F is particularly well-suited for the release of *N*-glycans, exhibiting specificity exclusively towards *N*-glycosylation sites. However, it is noteworthy that no enzyme is efficacious in releasing *O*-glycans. To address this limitation, chemical methods are employed for the liberation of *O*-glycans from mAbs featuring *O*-glycosylation sites(H Mehmet Kayili, Atakay, Hayatu, & Salih, 2022). It is pertinent to mention that a significant proportion of commercially available mAbs predominantly possess *N*-glycosylation sites, underscoring the relevance of utilizing PNGase F for *N*-glycan release. This methodological approach not only facilitates the comprehensive profiling of *N*-glycans on mAbs but also highlights the necessity of alternative strategies for *O*-glycan analysis in cases where *O*-glycosylation sites are present(Z. Zhang et al., 2009).

The golden analytical standard for glycan profiling of monoclonal antibodies (mAbs) involves the use of HPLC-HILIC-FLD(L. Zhang, S. Luo, & B. Zhang, 2016a). In this method, released glycans undergo labeling with a fluorophore tag. Numerous fluorophore tags have been documented in the literature for *N*-glycan labeling, with the widely utilized 2-aminobenzamide (2-AB) being the most common(Ruhaak et al., 2010). This tag is favoured for its cost-effectiveness and efficacy in glycan analysis using HPLC-HILIC-FLD. However, studies indicate that alternative fluorophore tags, such as procainamide, rapifluor, and instant PC, exhibit superior Fluorescence Detection (FLD) and Mass Spectrometry (MS) sensitivity in comparison to 2-AB. While 2-AB remains a popular choice, exploring these alternatives can enhance the sensitivity and precision of glycan analysis, offering a nuanced perspective for researchers in the field(H. M. Kayili, Sakhta, & Salih, 2022).

The majority of strategies employed for glycan profiling of monoclonal antibodies (mAbs) incorporate a crucial Hydrophilic Interaction-based purification step(H. M. Kayili, Ragoubi, & Salih, 2022). This step is essential for the practical analysis of *N*-glycans through HPLC-HILIC-FLD. The

labeling process involved in this analysis occurs under harsh conditions, often utilizing organic solvents, excess fluorophore tags, and reducing agents, all of which can impact the analysis. To mitigate these challenges, the incorporation of a HILIC purification step becomes imperative.

Materials featuring amide or amine-based functional groups are commonly employed for glycan purification in HILIC(H. M. Kayili, Ertürk, Elmaci, & Salih, 2019). This choice is rooted in the interaction facilitated by hydrogen bonding between the hydroxyl groups on glycans and the nitrogen groups on the sorbents. This interaction enhances the specificity of glycan purification, contributing to the removal of unwanted contaminants and facilitating a cleaner sample for subsequent analysis.

A pivotal aspect of glycan profiling involves the characterization of *N*-glycans derived from the obtained data. Identifying peaks corresponding to specific glycan structures is a crucial step in the analysis. An effective approach employing Glycan Unit Index (GU) facilitates the determination of glycan structures within the chromatogram(Gautam et al., 2020). This method involves labeling a glycan ladder, typically composed of dextran, with the same fluorophore tag utilized for *N*-glycan labeling(R. Zhang et al., 2021). The labeled glycan ladder is then subjected to analysis by HPLC-HILIC-FLD.

The retention time and the glycan unit information derived from the dextran ladder serve as the basis for calibration. This calibration curve enables the determination of the retention times corresponding to glycans in the sample, facilitating their annotation and quantification. The total area normalization approach is subsequently employed, wherein the areas under the annotated glycan peaks are summed(H. M. Kayili & Salih, 2021). This approach is crucial for calculating the relative abundances of different glycans in the sample.

Furthermore, the obtained glycan data is subjected to a comparative analysis with data from innovator products. This comparative evaluation provides insights into the glycan composition of the therapeutic protein in question, allowing researchers to discern any variations or similarities in glycosylation patterns(De Leoz et al., 2020). Overall, the application of the Glycan Unit Index and calibration with a glycan ladder significantly enhances the precision and reliability of glycan profiling in the context of monoclonal antibodies or other therapeutic proteins.

In the realm of glycan analysis, a complementary method involves extracting valuable information on glycoform relative abundances from glycopeptides(Saadé et al., 2021). In this methodology, monoclonal antibodies (mAb's) are enzymatically broken down into proteolytic products, which are then subjected to analysis using LC-C18-ESI-MS/MS(H. M. Kayili & Salih, 2022). This versatile technique accommodates the scrutiny of both glycopeptides and ordinary peptides. To discern glycopeptide signals within the MS/MS spectra, one can focus on oxonium ions, which are distinctive to glycopeptides(Stavenhagen et al., 2018). The subsequent identification of glycopeptide signals can be accomplished through manual or automated annotation. The optimal strategy for glycopeptide characterization employs the stepping energy collision-induced dissociation approach (SE-CID), enabling the separate determination of fragments from both the glycan backbone and peptide ions within glycopeptides(Hinneburg et al., 2016).

The wealth of MS/MS data generated by SE-CID has spurred the development of numerous commercially or freely available software tools. These software applications significantly enhance analysis efficiency by expediting the identification of glycopeptides and facilitating the extraction of corresponding areas within spectra(Bern, Kil, & Becker, 2012). The calculated relative abundances of glycopeptides can then be compared with those of the original products, providing insights into changes during the glycosylation process. Moreover, this approach allows for a comprehensive evaluation of peptide profiles, encompassing other post-translational modifications (PTMs). Through this holistic approach, any sequence variations in the final products can be robustly determined, underscoring the power of this methodology in glycoproteomic investigations.

Conclusion

In conclusion, the pivotal role of protein biopharmaceuticals in treating life-threatening diseases cannot be overstated, given their intricate structures. Glycosylation, as a prevalent post-translational modification, emerges as a key player in the modification landscape, with a majority of protein biopharmaceuticals exhibiting this modification. The microheterogeneity of glycans at glycosylation sites significantly influences the efficacy and safety of these therapeutic proteins. Recognizing the critical impact of glycosylation, a

comprehensive glycan analysis becomes indispensable in the pursuit of developing safe and effective drugs for human use. To achieve this goal, employing multiple analytical approaches is essential. This chapter has provided an in-depth exploration of the most appropriate method for the analysis of glycans associated with monoclonal antibodies (mAbs). By elucidating these analytical strategies, we aim to contribute to the advancement of biopharmaceutical development, ensuring the delivery of therapies that meet the highest standards of safety and efficacy for the benefit of patients worldwide.

REFERENCES

Bern, M., Kil, Y. J., & Becker, C. (2012). Byonic: advanced peptide and protein identification software. *Curr Protoc Bioinformatics, Chapter 13*, 13.20.11-13.20.14. doi:10.1002/0471250953.bi1320s40

Cui, W., Rohrs, H. W., & Gross, M. L. (2011). Top-down mass spectrometry: Recent developments, applications and perspectives. *Analyst, 136*(19), 3854-3864. doi:10.1039/C1AN15286F

De Leoz, M. L. A., Duewer, D. L., Fung, A., Liu, L., Yau, H. K., Potter, O., . . . Stein, S. E. (2020). NIST Interlaboratory Study on Glycosylation Analysis of Monoclonal Antibodies: Comparison of Results from Diverse Analytical Methods*. *Molecular & Cellular Proteomics, 19*(1), 11-30. doi:https://doi.org/10.1074/mcp.RA119.001677

Dotz, V., Haselberg, R., Shubhakar, A., Kozak, R. P., Falck, D., Rombouts, Y., Wuhrer, M. (2015). Mass spectrometry for glycosylation analysis of biopharmaceuticals. *TrAC Trends in Analytical Chemistry, 73*, 1-9. doi:http://dx.doi.org/10.1016/j.trac.2015.04.024

Fornelli, L., Ayoub, D., Aizikov, K., Beck, A., & Tsybin, Y. O. (2014). Middle-Down Analysis of Monoclonal Antibodies with Electron Transfer Dissociation Orbitrap Fourier Transform Mass Spectrometry. *Analytical Chemistry, 86*(6), 3005-3012. doi:10.1021/ac4036857

Gautam, S., Peng, W., Cho, B. G., Huang, Y., Banazadeh, A., Yu, A., . . . Mechref, Y. (2020). Glucose unit index (GUI) of permethylated glycans for effective identification of glycans and glycan isomers. *Analyst, 145*(20), 6656-6667. doi:10.1039/d0an00314j

Hinneburg, H., Stavenhagen, K., Schweiger-Hufnagel, U., Pengelley, S., Jabs, W., Seeberger, P. H., Kolarich, D. (2016). The Art of Destruction: Optimizing Collision Energies in Quadrupole-Time of Flight (Q-TOF) Instruments for Glycopeptide-Based Glycoproteomics. *J Am Soc Mass Spectrom, 27*(3), 507-519. doi:10.1007/s13361-015-1308-6

Houde, D., Peng, Y., Berkowitz, S. A., & Engen, J. R. (2010). Post-translational modifications differentially affect IgG1 conformation and receptor binding. *Mol Cell Proteomics, 9*(8), 1716-1728. doi:10.1074/mcp.M900540-MCP200

Kayili, H. M., Atakay, M., Hayatu, A., & Salih, B. (2022). Sample Preparation Methods for N-glycomics. *Advances in Sample Preparation*, 100042.

Kayili, H. M., Ertürk, A. S., Elmaci, G., & Salih, B. (2019). Poly(amidoamine) dendrimer-coated magnetic nanoparticles for the fast purification and selective enrichment of glycopeptides and glycans. *Journal of Separation Science, 42*(20), 3209-3216. doi:10.1002/jssc.201900492

Kayili, H. M., Ragoubi, Z. M. E., & Salih, B. (2022). An integrated stage-tip-based glycomic and glycoproteomic approach for simple and rapid N-glycosylation profiling of glycoproteins. *Biomedical Chromatography, 36*(12). doi:10.1002/bmc.5503

Kayili, H. M., Sakhta, R., & Salih, B. (2022). Comparison of denaturing agent effects in enzymatic N-glycan release for human plasma N-glycan analysis. *Turkish Journal of Chemistry, 46*(5), 1524-+. doi:10.55730/1300-0527.3457

Kayili, H. M., & Salih, B. (2021). N-glycan Profiling of Glycoproteins by Hydrophilic Interaction Liquid Chromatography with Fluorescence and Mass Spectrometric Detection. *Jove-Journal of Visualized Experiments*(175). doi:10.3791/62751

Kayili, H. M., & Salih, B. (2022). Site-specific N-glycosylation analysis of human thyroid thyroglobulin by mass spectrometry-based Glyco-analytical strategies. *J Proteomics, 267*. doi:10.1016/j.jprot.2022.104700

Kim, J., Jones, L., Taylor, L., Kannan, G., Jackson, F., Lau, H., . . . Bailey, B. (2010). Characterization of a unique IgG1 mAb CEX profile by limited Lys-C proteolysis/CEX separation coupled with mass spectrometry and structural analysis. *Journal of Chromatography B-Analytical Technologies in the Biomedical and Life Sciences, 878*(22), 1973-1981. doi:10.1016/j.jchromb.2010.05.032

Majumdar, R., Manikwar, P., Hickey, J. M., Arora, J., Middaugh, C. R., Volkin, D. B., & Weis, D. D. (2012). Minimizing Carry-Over in an Online Pepsin Digestion System used for the H/D Exchange Mass Spectrometric Analysis of an IgG1 Monoclonal Antibody. *Journal of the American Society for Mass Spectrometry, 23*(12), 2140-2148. doi:10.1007/s13361-012-0485-9

Oh, M. J., Hua, S., Kim, U., Kim, H. J., Lee, J., Kim, J. H., & An, H. J. (2016). Analytical detection and characterization of biopharmaceutical glycosylation by MS. *Bioanalysis, 8*(7), 711-727. doi:10.4155/bio.16.20

Rogstad, S., Faustino, A., Ruth, A., Keire, D., Boyne, M., & Park, J. (2016). A Retrospective Evaluation of the Use of Mass Spectrometry in FDA Biologics License Applications. *J Am Soc Mass Spectrom*. doi:10.1007/s13361-016-1531-9

Ruhaak, L. R., Zauner, G., Huhn, C., Bruggink, C., Deelder, A. M., & Wuhrer, M. (2010). Glycan labeling strategies and their use in identification and quantification. *Anal Bioanal Chem, 397*(8), 3457-3481. doi:10.1007/s00216-010-3532-z

Saadé, J., Biacchi, M., Giorgetti, J., Lechner, A., Beck, A., Leize-Wagner, E., & François, Y. N. (2021). Analysis of Monoclonal Antibody Glycopeptides by Capillary Electrophoresis-Mass Spectrometry Coupling (CE-MS). *Methods Mol Biol, 2271*, 97-106. doi:10.1007/978-1-0716-1241-5_7

Sandra, K., Vandenheede, I., & Sandra, P. (2014). Modern chromatographic and mass spectrometric techniques for protein biopharmaceutical characterization. *Journal of Chromatography A, 1335*, 81-103. doi:10.1016/j.chroma.2013.11.057

Sola, R. J., & Griebenow, K. (2010). Glycosylation of therapeutic proteins: an effective strategy to optimize efficacy. *BioDrugs, 24*(1), 9-21. doi:10.2165/11530550-000000000-00000

Staub, A., Guillarme, D., Schappler, J., Veuthey, J. L., & Rudaz, S. (2011). Intact protein analysis in the biopharmaceutical field. *Journal of Pharmaceutical and Biomedical Analysis, 55*(4), 810-822. doi:10.1016/j.jpba.2011.01.031

Stavenhagen, K., Kayili, H. M., Holst, S., Koeleman, C. A. M., Engel, R., Wouters, D., Wuhrer, M. (2018). N- and O-glycosylation Analysis of Human C1-inhibitor Reveals Extensive Mucin-type O-Glycosylation. *Molecular & Cellular Proteomics, 17*(6), 1225-1238. doi:10.1074/mcp.RA117.000240

Stavenhagen, K., Kolarich, D., & Wuhrer, M. (2015). Clinical Glycomics Employing Graphitized Carbon Liquid Chromatography-Mass

Spectrometry. *Chromatographia, 78*(5-6), 307-320. doi:10.1007/s10337-014-2813-7

Walsh, G. (2014). Biopharmaceutical benchmarks 2014. *Nat Biotech, 32*(10), 992-1000. doi:10.1038/nbt.3040

Whitelegge, J. (2013). Intact protein mass spectrometry and top-down proteomics. *Expert Review of Proteomics, 10*(2), 127-129. doi:10.1586/epr.13.10

Zhang, L., Luo, S., & Zhang, B. (2016a). Glycan analysis of therapeutic glycoproteins. *MAbs, 8*(2), 205-215. doi:10.1080/19420862.2015.1117719

Zhang, L., Luo, S., & Zhang, B. L. (2016b). Glycan analysis of therapeutic glycoproteins. *Mabs, 8*(2), 205-215. doi:10.1080/19420862.2015.1117719

Zhang, R., Peng, W., Gautam, S., Huang, Y., Mechref, Y., & Tang, H. (2021). GlycanGUI: Automated Glycan Annotation and Quantification Using Glucose Unit Index. *Front Chem, 9*, 707382. doi:10.3389/fchem.2021.707382

Zhang, Z., Pan, H., & Chen, X. (2009). Mass spectrometry for structural characterization of therapeutic antibodies. *Mass Spectrom Rev, 28*(1), 147-176. doi:10.1002/mas.20190

Zhang, Z. Q., Pan, H., & Chen, X. Y. (2009). Mass Spectrometry for Structural Characterization of Therapeutic Antibodies. *Mass Spectrometry Reviews, 28*(1), 147-176. doi:10.1002/mas.20190

Zheng, K., Bantog, C., & Bayer, R. (2011). The impact of glycosylation on monoclonal antibody conformation and stability. *Mabs, 3*(6), 568-576. doi:10.4161/mabs.3.6.17922

Zheng, K., Yarmarkovich, M., Bantog, C., Bayer, R., & Patapoff, T. W. (2014). Influence of glycosylation pattern on the molecular properties of monoclonal antibodies. *Mabs, 6*(3), 649-658. doi:10.4161/mabs.28588

CHAPTER 9

EXAMINING THE ROLE OF NANOMATERIALS AS EFFECTIVE ADSORBENTS AND THEIR APPLICATIONS IN THE REMOVAL OF POLLUTANTS FROM WASTEWATER

Assist. Prof. Dr. Nilgün ONURSAL[1]

DOI: https://dx.doi.org/10.5281/zenodo.10444770

[1] Siirt University, Faculty of Education, Department of Mathematics and Physical Sciences Education, Physical Sciences Education, Siirt, Türkiye, Email: nilgun.onursal@gmail.com, Orcid ID: 0000-0002-2460-6475

1. Introduction

Water is a substance as important as air and soil that is vital for the life of all living things on earth. It is the most fundamental entity in the development of humans and all living things. Access to clean water is a basic human need, and accessing clean water at low economic cost is very difficult. Therefore, it seems inevitable that there will be water wars in the future. Because the increase in the amount of heavy metals in water directly affects the rate of clean water (Onursal, 2023). Water directly or indirectly affects areas needed by humans and even all living things, such as health, economy, food and energy. Due to the increasing population, fresh water resources are gradually decreasing and increasing them does not seem possible under today's conditions. Because almost 25% of big cities experience water problems at some level. Moreover, approximately 2.2 billion people worldwide cannot access vital water (Pérez, García, Allieri, & Vázquez, 2023). There are heavy metals, pesticides, antibiotics, dyes, endocrine disruptors and many pollutants in wastewater (Madenli, Deveci, & Gönen, 2021). These pollutants can cause very serious health problems (Onursal,2022-ıjpas). In addition, these pollutants must be identified and do not need to be used as they are. Because, unfortunately, their presence in the environment, their effects on organisms and their fate are not fully understood. There is a very long list of these items. These; industrial products, detergents, sunscreens, insect repellents, pesticides, disinfectants, make-up, fragrances, oils, personal care products, oils, antibiotics, analgesics, anti-diabetics, anti-inflammatories, natural and synthetic hormones, additives, lipid regulators, flame retardants, surfactants, solvents, pathogens, nanomaterials; can be written as microplastics and antidepressants (Crini, et al., 2022). Human beings, trying to understand and recognize the events taking place in the universe, aim to solve their secrets based on these. Because this was very important in order to control nature and create a safe environment. In a sense, people's desire to know and learn can be considered as the first foundations laid for the birth of science (Utma, 2015). Science and technology play an important role in the lives of all societies over time, and rapidly developing technology has become almost an indispensable element of life. Nanoscience and nanotechnology, which are considered revolutionary in the twenty-first century, have been the pioneer of modern

research. (Onursal, 2023). The importance of the nano dimension was emphasized for the first time in Richard Feynman's speech titled "There is enough free space below/at the base" at the annual meeting of the American Physical Society at the California Institute of Technology on December 29, 1959. Feynman stated here that many discoveries could be made if production was made at nanoscale (Akkaş, 2018). The word nano is derived from the Greek nannos (νάννος) and means dwarf. Concepts defined by nano are expressed as one billionth of any size. It is defined as one billionth of a meter, which is several times the size of an atom.

For comparison, the diameter of a human hair is 80000 nm, and the diameter of a water molecule is approximately 0.3

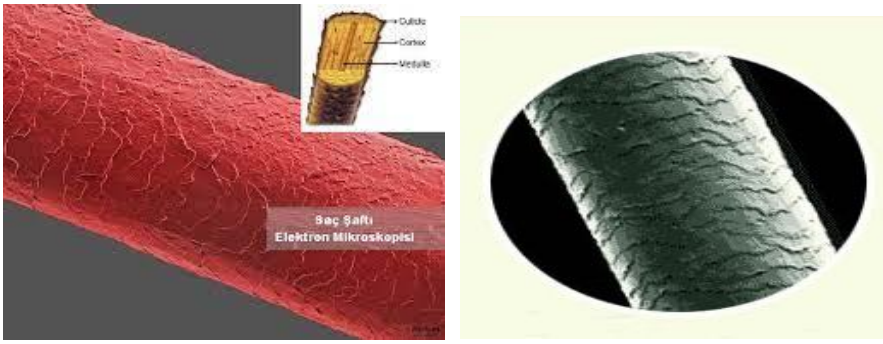

Picture 1. (a) Dermatology and Medical Aesthetics (Uzm.Dr. Hakan Buzoğlu), (b) Natrimin (https://natrumin.com.tr/sac-ile-ilgili-bilgiler/).

Nanoscience; It is defined as the scientific understanding and examination of the events that occur as a result of the manipulation and control of matter at the nanoscale (Bostancı, Boyraz, Zor, Zor, & Aslan, 2021). Nanotechnology, on the other hand, can be defined as the science and engineering of designing, synthesizing, characterizing and applying devices whose smallest functional functions are very small in nano size or one billionth of a meter (Saini, Saini, & Sharma, 2010). Although chemical oxidation and adsorption are effective methods in water treatment, they can sometimes be economically costly and quite time consuming.With the development of nanotechnology, nanotechnology is one of the most important factors in terms of quality and quantity in the treatment of water pollution to ensure environmental stability (Naser, Ahmed,, & Ali, 2021).

2. Nanotechnology

2.1. What is Nanotechnology?

Nanotechnology can be expressed as a process that combines the basic features of chemical, physical and biological sciences. Nanotechnology allows the production of nano-sized products such as atoms. Nanotechnology uses the reverse engineering principle that operates in nature, instead of producing materials by shrinking or reducing huge materials (Malik, Muhammad, & Waheed, 2023).

2.2. What is Nanomaterial?

Nano is a unit in the metric system and 1 nm = 10-9 m.

Nanomaterial: According to the common definition, materials with at least one dimension smaller than 100 nm or formed by combining these small materials are called nanomaterials (Köksal, Rahmi Köseoğlu, Narendra, & Kumbhat, 2022). Nanomaterial; These are materials whose physical and chemical properties can be changed by making changes in the structure of the substance at the nanoscale (Tan, 2015). These materials have been specially developed. The number and category of these materials are almost more than 1000. Nanomaterials have developed very rapidly, especially in the field of medicine. These; medical devices, cosmetics, bandages, dental repair materials, carbon nano materials (Beşergil, 2023), drug delivery systems, tissue and organ adhesives, antibacterial substances, anti-ultraviolet light substances, apoptosis of cancer cells under UV rays (a form of programmed cell death). or “cellular suicide) and can be written as water purification devices (Dağlıoğlu, Kabakçı, & Akdeniz, 2016), (Shah , Shah, Hussain, & Khan, 2017).

3. Adsorption

The phenomenon of a substance adhering to a surface or environment is called adsorption. The basis of the adsorption process is based on unbalanced forces (Buldağ & Yavuz, 2023). Adsorption is also expressed as the accumulation of liquid molecules, vapor, gas, and dissolved substances on the surface of a solid. The substance that accumulates / clings on the surface is called adsorbent (Dal,2021). The surface to which the substance adheres is called the adsorbent. The separation of attached molecules or particles from the surface is desorption (Demir & Yalçın, 2014).

3.1. Adsorbents

There are many adsorbent substances in nature. Adsorbents must not harm the environment, be non-toxic, easily obtainable and recyclable, insoluble in water, contain functional groups, have large surface areas and be scientifically accepted (Demir & Yalçın, 2014). Organic and inorganic adsorbents such as biochar, activated carbon, zeolite, biofuels, polymer materials, agricultural waste carbon-based adsorbents are some of them (Dehghani, et al., 2023). Apart from this, clays (Dal & Onursal, 2023), basalt (Dal M. C., Onursal, Arıca, & Yavuz, 2021), calcite and Midyat stone (Altunkaynak, 2022) are also used as adsorbents. Apart from this, clays (Dal & Onursal, 2023), basalt (Dal M. C., Onursal, Arıca, & Yavuz, 2021), calcite and Midyat stone (Altunkaynak, 2022) are also used as adsorbents. Adsorption plays an important role in the removal of low levels of toxic and harmful compounds and is widely used today (Uçar, 2019). The names and surface areas of some adsorbents are given in table 1 below.

Table 1. Some adsorbents and their surface areas

Name of Adsorbent	Surface Area	Source
Synthetic NaY Zeolite	654 m^2g^{-1}.	(Dikmen & Orhun, 2013)
Siirt (Koçpınar) Clay	19.178 m^2g^{-1}.	(Onursal,2022)
Malatya Clay	60.266 m^2g^{-1}	(Onursal, Altunkaynak, Baran, & Dal, 2023)
Sivas Clay	153.364 m^2g^{-1}	
Pumice (Bitlis)	26.44 m^2g^{-1}	(Tanaydın, Tanaydın, İnce, & Demirkıran, 2022)
Basalt (Diyarbakır/Karacadağ) Karacadağ Scoria	4.98 m^2g^{-1}	(Dal M. C., Onursal, Arıca, & Yavuz, 2021)
Midyat stone (Mardin)	15.848 m^2g^{-1}	(Canpolat, Altunkaynak, & Yavuz, 2022)
Glass powder	20.4 dm^2/g	(Aroğuz, 1984)
Average Surface Areas of Coal, Lignite, Wood and Coconut Shell Activated Carbons are 500-1500 m2/g (Karakaş, 2019)	500-1500 m^2/g	(Karakaş, 2019)
Cellulose (pH=6)	73,46 mg Cr^{+3}/ g	(Yıldırım, 2019)

3.2. Nanomaterials as Adsorbents and Their Usage Areas

We can group adsorbents as carbons, synthetic polymers, and inorganic and organic substances (Erkayacan, 2007). Natural adsorbents are divided into two according to their origin. As organic and inorganic adsorbents. Inorganic adsorbents can be written as clay, zeolite, perlite, bentonite, fuller's soil, coke, lignite and peat (Baylan, 2013). Organic adsorbents can be expressed as living and non-living organic substances. Microorganisms can be said to be living adsorbents (Demir & Yalçın, 2014). Non-living adsorbents are quite abundant. Some of these are Chitosan, tree bark, hazelnuts, peanuts, almonds, cashews, walnuts, chestnuts, coconut, peanut shells and sawdust, resin, fruit shells and hard fruit seeds, roots, stems, tea, coffee pulps, grain (rice, wheat, lentils) and agricultural wastes. Additionally, melon, watermelon, orange (Canpolat,2022), apple, acorn, tangerine, mango, wool, cotton and many vegetables and fruits can also be written. Nanomaterials used as sorbents can also be defined as inorganic and organic nanomaterials. Apart from this, organic nanomaterials can be defined as organic polymer nanomaterials and nanocomposite materials supported by organic polymers. Inorganic materials are in the form of transition metal-sulfur-oxide nanoparticles and carbon/silica-based nanomaterials. Recently, graphene and graphene oxide-based nanocomposite materials have been widely used and studied (Seval, 2021). Recently, nanoadsorbent materials have been used more widely, especially in water treatment, and have a unique potential in the adsorption process. When compared with general adsorbents, the unique properties of nanoadsorbents increase their application areas and appear to be more useful in many areas. Therefore, further and renewed studies, including surface modification and chemical stabilization, are needed to improve the applications of nanoadsorbent materials in water or wastewater.

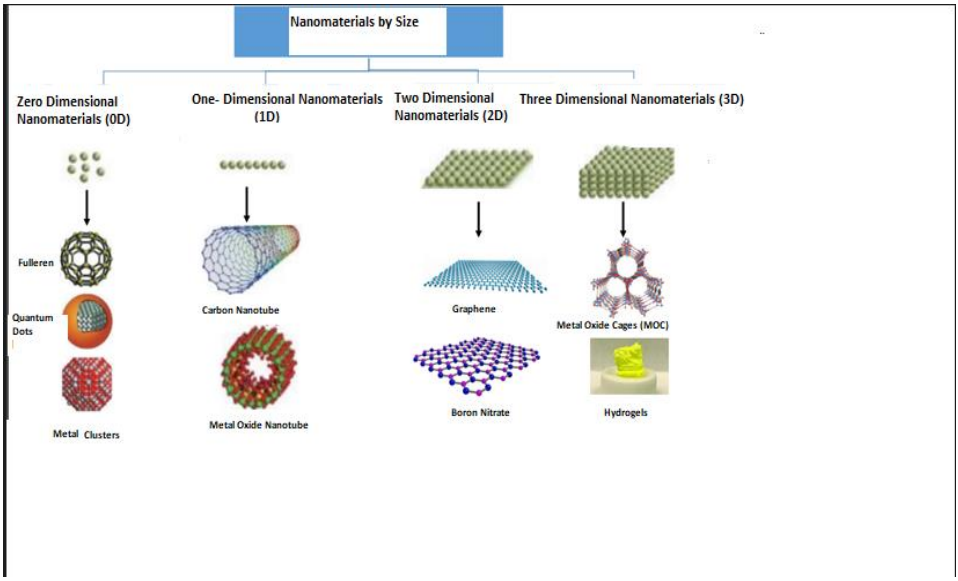

Picture 2. Nanomaterials according to their sizes (https://acikders.ankara.edu.tr/pluginfile.php/196157/mod_resource/content/0/KYM%20345%20Yeni%20Malzemeler-Nanomalzemeler.pdf). Retrieved from.

It is extremely important to recycle wastewater efficiently and discharge it without harming nature. Graphene and its derivatives and carbon-based nanomaterials have high conductivity as well as having a large surface area. Due to the various chemical and physical properties of these materials, nanocomposite and biocomposite adsorbents are synthesized by improving their functionality with different materials. In particular, graphene highlights its very different properties in the scientific world in terms of adsorption (Madenli, Deveci, & Gönen, 2021). Nanoadsorbent materials today produce promising solutions to environmental problems. The unique high physical and chemical properties of nanoadsorbers compared to conventional adsorbents promote their widespread use.

4. CONCLUSION

Environmentally friendly, sustainable and economical technologies have always attracted the attention of human beings. In this sense, quite intensive studies have been carried out recently. Scientists' introduction to nanostructure has made them indispensable. Nowadays, nanomaterials are produced and used in many areas. Nanotechnology has revolutionized the field of engineering and

medicine, as well as developments in science and technology. It is clear that this will be the most important competitive area of the industry of the century.

For this reason, countries should direct their future generations to this field and ensure that they acquire the necessary interest and information about this field. Only in this way can they compete with other countries and keep up with the times. Nanotechnology appeals to and is used in almost every field. For example, it provides a great advantage in terms of examining the events occurring in nature at the molecular and atomic level. The reasons why these materials are preferred include high efficiency and being an alternative source. However, these materials must be environmentally friendly. According to the studies, there is not enough research on the toxic effects of nanoparticles, some on the respiratory system. The development of nanotechnology also provides extremely successful results in the removal of wastewater. Nanocarbon tubes, fullerenes, nanosilver, nanogold, nanometal oxides are a few of them. Recently, nano adsorbents have been intensively developed and the desired results are achieved in the purification process. The century we are in is a candidate to be the century of nanomaterials.

References

Onursal, N., & Dal, M. C. (2023). Investigation of isotherm and thermodynamic parameters of adsorption of copper (II) ions in aqueous solution with natural mixed type Siirt clay (NMTSC-2) and new (second) linear equation derived from Harkins–Jura isotherm. *Chemical Papers*, https://doi.org/10.1007/s11696-023-03116-4.

Pérez, H., García, O. J., Allieri, M. A., & Vázquez, R. R. (2023). Nanotechnology as an efficient and effective alternative for wastewater treatment: an overview. *Water Sci Technology 87 (12)*, 2971-3001.

Madenli, Ö., Deveci, E. Ü., & Gönen, Ç. (2021). Ağır Metal Gideriminde Grafen Uygulamaları: Adsorpsiyon Teknolojisi. *Fırat Üniversitesi Müh. Bil. Dergisi, 33(1)*, 151-159.

Onursal, N. (2023). Ni (II)'nin Atık Badem kabuğundan Üretilen Biyonanokompozit ile Sulu Çözeltilerden Giderimi. *MAS JAPS 8(2)*, 391-402.

Crini, N. M., Lichtfouse, E., Fourmentin, M., Ribeiro, A. R., Noutsopoulos, C., Mapelli, F., . . . Piraján, M. e. (2022). Removal of emerging contaminants from wastewater. *Environmental Chemistry Letters, 20*, 1333-1375.

Utma, S. (2015). Bilim iletişimi ve bilim gazeteciliği: ege üniversitesi haber ajansı örneğinde üniversitelerde bilim haberlerinin üretilmesine yönelik bir inceleme. *Ege Üniversitesi Sosyal Bilimler Enstitüsü, Doktora Tezi* . İzmir, Türkiye: Ege Üniversitesi .

(Onursal, Iron-Based Nanomaterials as Wastewater and Pollutant Adsorbents, 2023)

Akkaş, M. A. (2018). Nano iletişim Teknolojilerinin Biyomedikale Katkısİ. *Sakarya Üniversitesi Fen Bilimleri Enstitüsü Dergisi, 22 (2)*, 516-528.

Arıcı, A. (2018). Elektrospin Metodu ile Hazırlanan Polimer/Mwcnt Nanofiberlerin Özelliklerine Mwcnt Çapının ve Uzunluğunun Etkisinin Araştırılması. *Necmettin Erbakan Üniversitesi Fen Bilimleri Enstitüsü*. Konya: Necmettin Erbakan Üniversitesi.

Bostancı, Ş. Ç., Boyraz, A., Zor, T. Ş., Zor, E., & Aslan, O. (2021). Nanobilim ve Nanoteknolojinin TÜBİTAK Popüler Bilim Dergilerine

Yansımaları. *Uluslararası Türk Eğitim Bilimleri Dergisi, 10 (17)*, 90-113.

Saini, R., Saini, S., & Sharma, S. (2010). Nanotechnology: The Future Medicine. *J Cutan Aesthet Surg, 3(1)*, 32-33.

Naser , J. A., Ahmed,, Z. W., & Ali, E. H. (2021). Nanomaterials usage as adsorbents for the pollutants removal from wastewater; a review. *Materials Today: Proceedings, 42*, 2590-2595.

Malik, S., Muhammad,, K., & Waheed, Y. (2023). Nanotechnology: A Revolution in Modern Industry. *Molecules.28(2): 661*, doi: 10.3390/molecules28020661.

Köksal, F., Rahmi Köseoğlu, Narendra, K., & Kumbhat, S. (2022). *Essentials in Nanoscience and Nanotechnology- Nanobilim ve Nanoteknoloji/Bartın Üniversitesi Ders Kitabı.* Wiley-nobel.

Tan, E. (2015, Aralık). Antibakteriyel Yeni Bir Nano-Biyokompozitin Hazırlanması ve Yüzey Karakterizasyonu. *İstanbul Üniversitesi Fen bilimleri enstitüsü*. İstanbul: İstanbul Üniversitesi .

Beşergil, B. (2023, Aralık 23). *Karbon Nanomalzemeler(Carbon nanomaterials).* Prof. Dr. Bilsen Beşergil: https://bilsenbesergil.blogspot.com/p/karbon-nanomalzemeler-carbon.html adresinden alındı

Dağlıoğlu, Y., Kabakçı, D., & Akdeniz, G. (2016). Nanokteknoloji/Nanopartikül, Çevre Ve Bal Arıları Arasındaki İlişki. *Arıcılık Araştırma Dergisi, Cilt:8, Sayı:1*, 22-27.

Shah , S. N., Shah, Z., Hussain, M., & Khan, M. (2017). Hazardous Effects of Titanium Dioxide Nanoparticles in Ecosystem. *Bioinorg Chem Appl*, doi: 10.1155/2017/4101735.

Buldağ, E., & Yavuz, Ö. (2023). Adsorption Kinetics of Cu(II) and Ni(II) Ions Using Clay in Kulp District of Diyarbakır Province. *Gazi University Journal of Science*, 78-88.

Dal, M. C. (2021, Temmuz). Cu (II), Ni (II) VE Co(II)'nin Karacadağ Skoryası ile Adsorpsiyonunun İzoterm, Kinetik ve Termodinamik Analizi. *Dicle Üniversitesi Fen Bilimleri Enstitüsü-Doktora Tezi*. Diyarbakır: Dicle Üniversitesi.

Demir, E., & Yalçın, H. (2014). Adsorbentler: Sınıflandırma, Özellikler, Kullanım ve Öngörüler. *Türk Bilimsel Derlemeler Dergisi 7 (2)*, 70-79.

Dehghani , M. H., Ahmadi, S., Ghosh, S., Othmani, A., Osagie, C., Meskini, M., . . . Lima , E. C. (2023). Recent advances on sustainable adsorbents for the remediation of noxious pollutants from water and wastewater: A critical review. *Arabian Journal of Chemistry, Volume 16, Issue 12*, https://doi.org/10.1016/j.arabjc.2023.105303.

Dal, M. C., & Onursal, N. (2023). Two new linearized equations derived from a pseudo-second-order kinetic model. *Deswater, 308*, 183-189.

Dal, M. C., Onursal, N., Arıca, E., & Yavuz, Ö. (2021). Diyarbakır Karacadağ Kırmızı Tepe Skoryası ile Cu (II) Adsorpsiyon Kinetiğinin İncelenmesi. *Dicle Üniversitesi Mühendislik Fakültesi Mühendislik Dergisi*, 337-346.

Dikmen, Z., & Orhun, Ö. (2013). Manyetik Modifiye Edilmiş Sentetik ve Doğal Zeolitlerin Hazırlanması ve Bazı Fiziksel Özelliklerinin Kıyaslanması. *Anadolu Üniversitesi Bilim ve Teknoloji Dergisi-A Uygulamalı Bilimler ve Mühendislik, Vol.: 14-No: 1*, 75-90.

Onursal, N. (2022). Removal of Ni (II) Ions from Aqueous Solutions with Siirt Koçpınar Mixed Type Clay (SKMTC) Investigation of Isotherm, Thermodynamic and Kinetic Parameters. *Desalination and Water Treatment, (276)*, 150-159.

Onursal, N., Altunkaynak, Y., Baran, A., & Dal, M. C. (2023). Adsorption of nickel(II) ions from aqueous solutions using Malatya clay: Equilibrium, kinetic, and thermodynamic studies. *Environmental Progress & Sustainable EnergyVolume 42, Issue 5*, https://doi.org/10.1002/ep.14150.

Tanaydın, Z. B., Tanaydın, M. K., İnce, M., & Demirkıran, N. (2022). Ponza ile bakır ve kurşun iyonlarının adsorpsiyon karakteristikleri. *GUFBD / GUJS 12(2)*, 581-596.

Canpolat, M., & Altunkaynak, Y. (2022). Sulu Çözeltilerden Nikel(II) İyonlarının Uzaklaştırılmasında Portakal Kabuğu Atığının Kullanılması: Denge, Kinetik Ve Termodinamik Çalışmalar. *Journal of Advanced Research in Natural and Applied Sciences,8(2)*, 322-339.

Aroğuz, A. Z. (1984). Bazı Pestisıtlerin Özel Hazırlanmış Olan Cam Tozları Üzerindeki Adsorpsiyonun İncelenmesi, Adsorpsiyon Isısı ve Adsorban Yüzey Alanlarının Hesaplanması. *İstanbul Üniversitesi*

Mühendislik Fakültesi Kimya Bölümü-Fizikokimya A.B.D. İstanbul: İstanbul Üniversitesi.

Karakaş, M. (2019). Sulu Çözeltilerden Adsorpsiyon Yöntemi ile Cr(VI) Giderimi. *Sakarya Üniversitesi Fen Bilimleri Enstitüsü*. Sakarya: Sakarya Üniversitesi .

Yıldırım, S. A. (2019). Nikel Oksit Katkılı Farklı Türde Gözenekli Malzeme ile Desteklenmiş Metal Oksit Adsorbentler Kullanılarak Atık Sulardan Krom (VI) Giderilmesi. *Gazi Üniversitesi Fen Bilimleri Enstitüsü*. Ankara: Gazi Üniversitesi.

Erkayacan, H. (2007). Yer Fıstığı Kabuğunun Adsorban Olarak Kullanımı. *Yıldız teknik Üniversitesi Fen Bilimleri Enstitüsü*. İstanbul, Türkiye: Yıldız teknik Üniversitesi.

Baylan, N. (2013). Bentonit ve Üzüm Çekirdeği Aktif Karbonunun Tekli ve Çoklu İyon Sistemlerindeki Adsorpsiyon Özelliklerinin İncelenmesi. *İstanbul Üniversitesi Fen Bilimleri Enstitüsü*. İstanbul, Türkiye: İstanbul Üniversitesi.

Canpolat, M., Altunkaynak, Y., & Yavuz, Ö. (2022). Kimyasal olarak işlenmemiş Midyat taşı kullanılarak sulu çözeltilerden Pb(II) iyonlarının etkin bir şekilde uzaklaştırılması: İzoterm, kinetik ve termodinamik çalışmalar. *Niğde Ömer Halisdemir Üniversitesi Mühendislik Bilimleri Dergisi,11(4).*, 1085-1096.

Uçar, M. (2019). Adsorption of chlorophenolic compounds on activated clinoptilolite. *Adsorption Science & Technology, volume:37, Issue 7-8*, 664-679.

Seval, k. (2021). Su Örneklerindeki Metal İyonlarının Tayini İçin Silika Nanopartikül Kaplı Grafen Oksitin Katı Faz Ekstraksiyon Sorbenti Olarak Kullanımı. *Pamukkale Üniversitesi fen Bilimleri Enstitüsü*. Denizli, Türkiye: Pamukkale Üniversitesi .

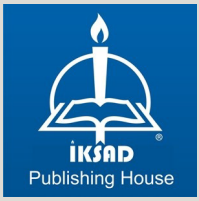

ISBN: 978-625-367-562-2